The central engine of Active Galactic Nuclei

Nikita Salvi

Mullard Space Science Laboratory
Department of Space and Climate Physics
University College London

A thesis submitted to the University of London
for the degree of Doctor of Philosophy

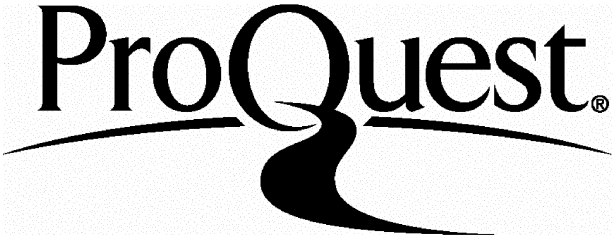

To

my Parents

for all your love and support

Abstract

Active Galactic Nuclei (AGN) are luminous objects thought to be powered by accretion of material onto a super-massive black hole. They emit radiation across a wide frequency range from the γ-rays to the radio. X-ray emission, relativistic jets and superluminal motion are phenomena which originate close to the central power source and can be used to study conditions in the innermost regions around a black hole. To understand the central engines in these sources, I have used the high sensitivity and signal to noise $XMM - Newton$ data to study the X-ray emission in three observationally very different AGN. III Zw2 is a luminous ($L_{2-10} \sim 10^{45}$ erg s^{-1}) radio-intermediate (i.e. intrinsically radio weak but with relativistic jets pointed straight at the observer) quasar and I have studied its radio to X-ray emission over a period of 25 years. The X-ray data for a bright ($L_{2-10} \sim 10^{44}$ erg s^{-1}) radio quiet Seyfert 1 galaxy MCG-2-58-22 is compared with advanced reflection models incorporating Compton reflection and re-processing of X-rays in an accretion disk in a self consistent manner. I have also studied the rapidly variable X-ray emission in a low luminosity ($L_{2-10} \sim 10^{40-41}$ erg s^{-1}) narrow line Seyfert 1 galaxy NGC 4051. Time resolved spectra are used to better understand the properties of various components in the X-ray emission of this source. To help discriminate between theoretical models that explain energy generation close to the central source and to obtain clues to the dominant emission mechanisms within the source I have also studied the multi-wavelength emission and the broad band spectrum (radio to X-rays) of these AGN.

Acknowledgements

I thank Dr Mat Page for taking on my secondary supervisor-ship despite the prevailing circumstances and providing encouragement and guidance during the difficult period of my PhD. His continuous support and critical evaluation of my work has helped raised the standard of this thesis. I thank Dr Kinwah Wu most sincerely for taking time out of his busy schedule on a regular basis to help strengthen my foundations of theoretical physics and for his invaluable advice on the content, structure and time-line for writing this thesis. I am grateful for his unofficial supervision and expert advice which has helped in the timely completion of this thesis despite initial set backs. I would also like to thank Dr Roberto Soria for his suggestions and discussions which have helped improve the structure of this thesis. Dr Mittaz and Dr Rosenwell thanked for for their help and guidance in analyzing the X-ray data from previous missions and the XMM-newton optical monitor data respectively along with all postdocs and students for their help in dealing with everyday problems. I thank my supervisor Prof. Keith Mason for offering me the PPARC PhD student-ship and for going through my work in a reasonably short period of time during these last few months, despite his extremely busy schedule.

My heartfelt thanks to my parents for their unconditional love, support and constant encouragement which gave me the strength and the confidence to achieve my goals. Most of all I am grateful to them for believing in me, teaching me to be strong in the face of adversity and making me who I am. Finally, I thank my husband for his love, infinite patience and understanding. He has been my strength and inspiration and I could not have done this without him by my side.

Contents

List of Figures

List of Tables

Chapter 1

Introduction

1.1 History

The mystery and fascination of Active Galactic Nuclei (AGN) began in the early 1940's with the advancement in radio astronomy, the detection of powerful radio sources and radio jets, and the discovery of spiral Galaxies with bright star-like nuclei by Carl Seyfert (Seyfert 1943) that were more luminous than the entire host Galaxy. Over the next few decades several exciting discoveries were made regarding these peculiar objects. AGN were found to be much brighter in the UV compared to normal stars and not all of them appeared to be radio loud (Matthews & Sandage 1963, Sandage 1965). Their emission line spectra showed large redshifts indicating that the sources were extra-galactic in origin (Hazard et al. 1963, Schmidt 1963, Oke 1963, Greenstein & Matthews 1963). Also the X-ray emission in some AGN was found to be rapidly variable, indicating a very compact emission region (Marshall et al. 1981). After six decades the AGN phenomenon still remains controversial and continues to challenge the brightest minds. One of the most difficult issues is understanding the energy generation mechanism, 'the central engine', in these extremely luminous objects ($L_{X-ray} > 10^{40}$ erg s^{-1}) whose enormous energy output is seen to arise from a very small region and cannot be accounted for by nuclear fusion which powers

stars. The only known theoretical process for energy production that can account for such high luminosities from very compact volumes is the process of accretion onto a massive object, in which the potential energy of the in-falling material is efficiently converted into radiation. The amount of gravitational potential energy released is proportional to the mass (M)-to-radius (R) ratio of the accreting object (E_{acc} = GMm/R), so the more compact the object, the greater is the energy liberated. The observed AGN luminosities require accretion on to *supermassive black holes* ($10^6 - 10^9$ $M_\odot$) to account for their energy output.

Although the black hole model was first introduced as a theoretical necessity to explain the large energy output from compact volumes in AGN, the evidence in favour of super-massive black holes at the center of galaxies including our own, is growing at an increasing pace (Rees 1998). If AGN are powered by accretion on to a super-massive black hole they are laboratories of extreme physics which cannot be duplicated on earth and as such provide a unique opportunity for testing current theories of relativistic physics. Also the high luminosities of these objects allow them to be detected at very large redshifts and hence serve as excellent tools with which to study the early universe.

1.2 The AGN model

Observations over the past few decades have provided us with an understanding of the approximate structure of AGN (Fig 1.1 & Fig 1.2). The detailed physics however, is still unclear mainly due the diversity of emission in these objects, which spans a wide frequency range from the radio to the γ-rays. At the center of AGN lies a super-massive black hole which drags the surrounding material into its deep gravitational potential well. If the in-falling material has significant angular momentum, it cannot accrete radially, but forms an accretion disk around the central black hole. As material in the accretion disk spirals towards the black hole it is heated by viscous and turbulent forces to higher and higher temperatures and emits

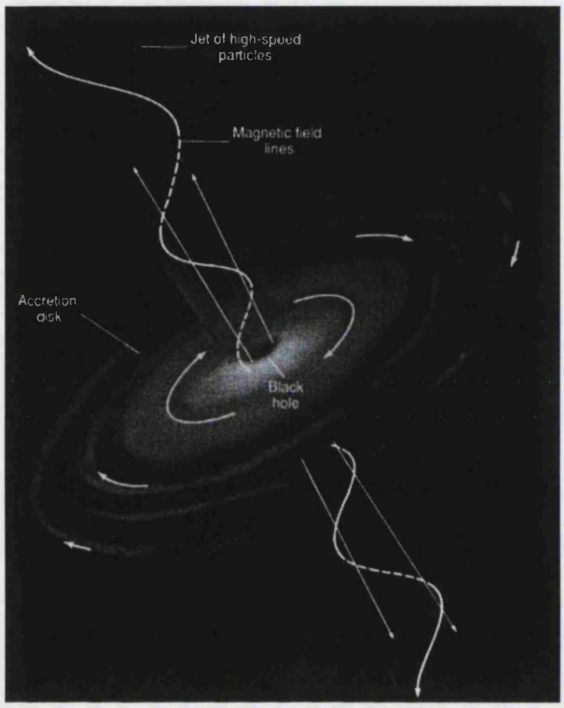

Figure 1.1: A schematic figure of the inner regions of AGN. (*credit*; Hartman & Impey; chapter 25, http://zeba.uoregon.edu/ js/ast123/lectures/lec15.html)

thermally, giving rise to optical emission from the outer cooler parts of the disk and UV and perhaps soft X-ray emission from the inner, hotter parts of the disk. The inner parts of the disk are also thought to be covered by a spherical or 'slab-like' corona where hot electrons Compton up-scatter the cooler disk photons to the X-ray band, giving rise to the observed power-law X-ray emission. It has been suggested that electromagnetic energy can also be directly extracted from the black hole itself, if it is spinning. Magnetic fields are thought to be collimated via some poorly understood processes in regions closest to the black hole giving rise to relativistic jets (and superluminal motion) which are responsible for the observed non-thermal (synchrotron) radiation. This central region is very compact and is though to be a few light days across.

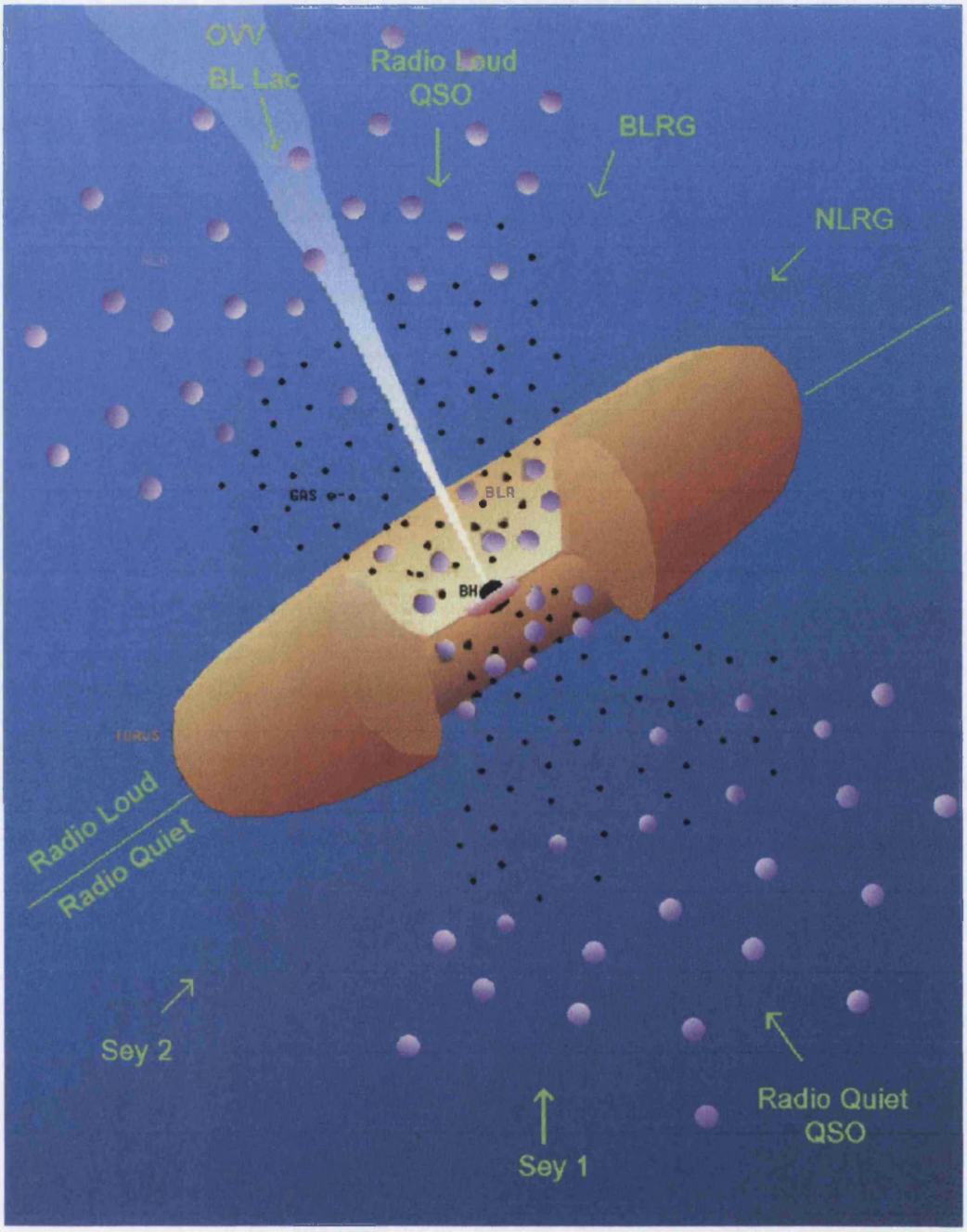

Figure 1.2: A schematic diagram of the physical structure of AGN (*credit* : M. Urry & P.Padovani (Space Telescope Science Institute) isdc.unige.ch/Outreach/Help/help.html). At the center lies the super-massive black hole surrounded by an accretion disk which fuels it and the relativistic jets. Further outward from the accretion disk are the dense rapidly moving broad line clouds (dark blobs). The central regions are surrounded by an optically thick dusty molecular torus. Beyond the torus are the low density slower moving narrow line clouds (light blobs)

At distances of about 100 light days from the center are dense clouds which move around the black hole at relatively high velocities (few thousand km s^{-1}), the so called 'broad line clouds' which give rise to the broad UV and optical emission lines seen in AGN spectra. Further outwards at distances of 100 light years, is a dusty optically thick molecular torus which obscures certain (or all) parts of the central regions depending on the observer's line-of-sight. Beyond the torus, (about 1000 light years from the center) are low density slower moving clouds which produce the narrower emission lines in AGN spectra. Fig 1.2 shows a hypothetical model (not to scale) for the physical structure in AGN.

1.2.1 Classification of AGN

AGN are classified into two main groups based on their radio properties, i.e. radio-loud AGN and radio-quiet AGN. They are further divided into various sub-groups based on their observed broadband properties such as, luminosity, spectral and temporal properties etc. This has led to a confusing zoo of AGN groups which are not well separated from each other as there are several objects that display properties of more than one group. The unified theory predicts, that since the AGN model is axisymmetric, the same AGN would look radically different when viewed from different angles, i.e. when viewed face-on one would see the nuclear as well as the extended emission but when viewed edge-on the nuclear emission would be effectively obscured by the torus (Antonucci 1993). The belief that the observed variety in AGN emission could be largely, a result of observing systems of differing radio-loudness and luminosities at different orientation angles has led to the classification of AGN into three broad categories: Type 1 AGN, Type 2 AGN and Blazars.

Type 1 AGN

When a system is viewed at low inclination angles we have an almost unobstructed view of the central regions of the accretion disk around the black hole and the broad line region. Hence this class of AGN are generally strong X-ray (keV) sources, have bright variable continuua and both broad (line widths $\sim 10^4$ km s^{-1}) and narrow optical/UV emission lines (Antonucci 1993). The high luminosity radio-quiet type 1 AGN were originally known as Quasi Stellar Objects (QSO). Today the term "quasar" is used for both radio-quiet and radio-loud objects. They are highly redshifted and their host galaxies are difficult to observe due to the bright central nuclei. The lower luminosity Seyfert 1s (typically $M_B >$ -23; Schmidt & Green 1983) are relatively nearby sources whose host Galaxies can be resolved. The narrow line Seyfert 1 galaxies (NLS1) are a subclass of this group and are characterised by steep soft X-ray spectra and rapidly variable X-ray emission (Boller et al. 1996, 1997). The low luminosity radio-loud type 1 AGN are called Broad Line radio galaxies (BLRG). The high luminosity radio-loud quasars are further sub-divided into Flat Spectrum Radio Quasers (FSRQ) and Steep Spectrum Radio Quasars (SSRQ) depending on their radio continuum shape.

Type 2 AGN

When a system is viewed almost edge-on the central regions of the AGN are expected to be obscured from view by an optically thick molecular torus. This class of AGN have weak continuua and only narrow emission lines (line widths $<$ 1000 km s^{-1}) as their circumnuclear region is not directly visible and most (but not all) of them are not seen to be strong X-ray (keV) emitters. The Seyfert 2 galaxies and Narrow Emission Line X-ray galaxies (NELG) which exhibit weak or undetectable broad lines (Mushotzky 1982) make up the low luminosity radio-quiet type 2 AGN group. The NLS1 galaxies are distinguishable from the Seyfert 2 galaxies by the presence of Fe II or higher ionisation iron lines (e.g. [Fe VII] and [Fe X]) and [O III] to H_β ratio

< 3 which is typical of Seyfert 1 galaxies. The identification of objects belonging to the high luminosity group has been a challenge; however, in recent years the IRAS infrared luminous AGN have been put forth as prototypes of high luminosity radio-quiet type 2 AGN (Franceschini et al. 2000, Frogel et al. 1989).

Narrow Line Radio Galaxies (NLRG) are examples of radio-loud type 2 AGN and include the Fanaroff-Riley type 1 (FR I) and Fanaroff-Riley type 2 (FR II) radio galaxies (Fanaroff and Riley 1974, Bridle & Perley 1984). The FR I sources are characterised by prominent, usually very symmetric twin jets, whose nuclear power is seen to decrease with distance and as such hot spots at the outer ends of the lobes are never seen (Parma et al. 2002). FR II sources show very prominent, broad lobes and hot-spots at the end of large-scale, highly collimated jets. The edge-on orientation argument for Type 2 AGN is strengthened by the detection of strong broad lines in the polarised light of Type 2 Galaxy NGC 1068 (Barth et al. 1999, Antonucci & Miller 1985).

Blazars

These are an extreme class of Type 1 radio-loud AGN characterised by high variability at all bands from radio to GeV and TeV, polarised emission (Urry & Padovani 1995), the absence of strong emission or absorption lines in their spectra, very high brightness temperatures and superluminal motion. The orientation of these objects is thought to be almost pole-on with the relativistic jets pointed straight at the observer. The lower luminosity blazars are called BL Lacertae (BL Lacs) objects, while the Optically Violent Variable quasars (OVVs) and the Highly Polarised quasars (HPQs) form the high luminosity group.

Their spectral energy distributions show two distinct peaks. One is at IR to X-ray energies and is thought to be due to synchrotron radiation from relativistic jets pointing straight towards the observer (Georganopoulos 2000). The second peak lies at GeV−TeV energies and is thought to be due to Compton up-scattering of synchrotron or external photons by the population of relativistic electrons that give

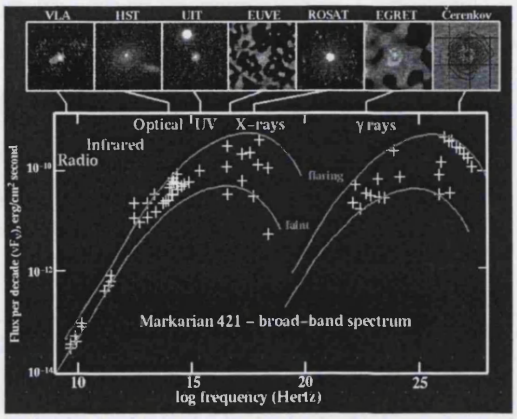

Figure 1.3: Broad band spectral energy distribution (SED) of the blazar Mrk 421. The radio to X-ray emission is synchrotron radiation while the γ-rays are produced by Compton up-scattering of low energy photons by the same energetic electrons that give rise to synchrotron radiation. *credit* : Bill Keel, http://www.astr.ua.edu/keel/agn/

rise to synchrotron radiation (Böttcher 2000). Fig 1.3 shows the energy output of a typical blazar Mrk 421. In this system the radio to X-ray emission is well modelled as synchrotron radiation and the γ-rays as Compton up-scattered emission.

A diagram summarising the AGN sub-groups discussed before is shown in Fig 1.4.

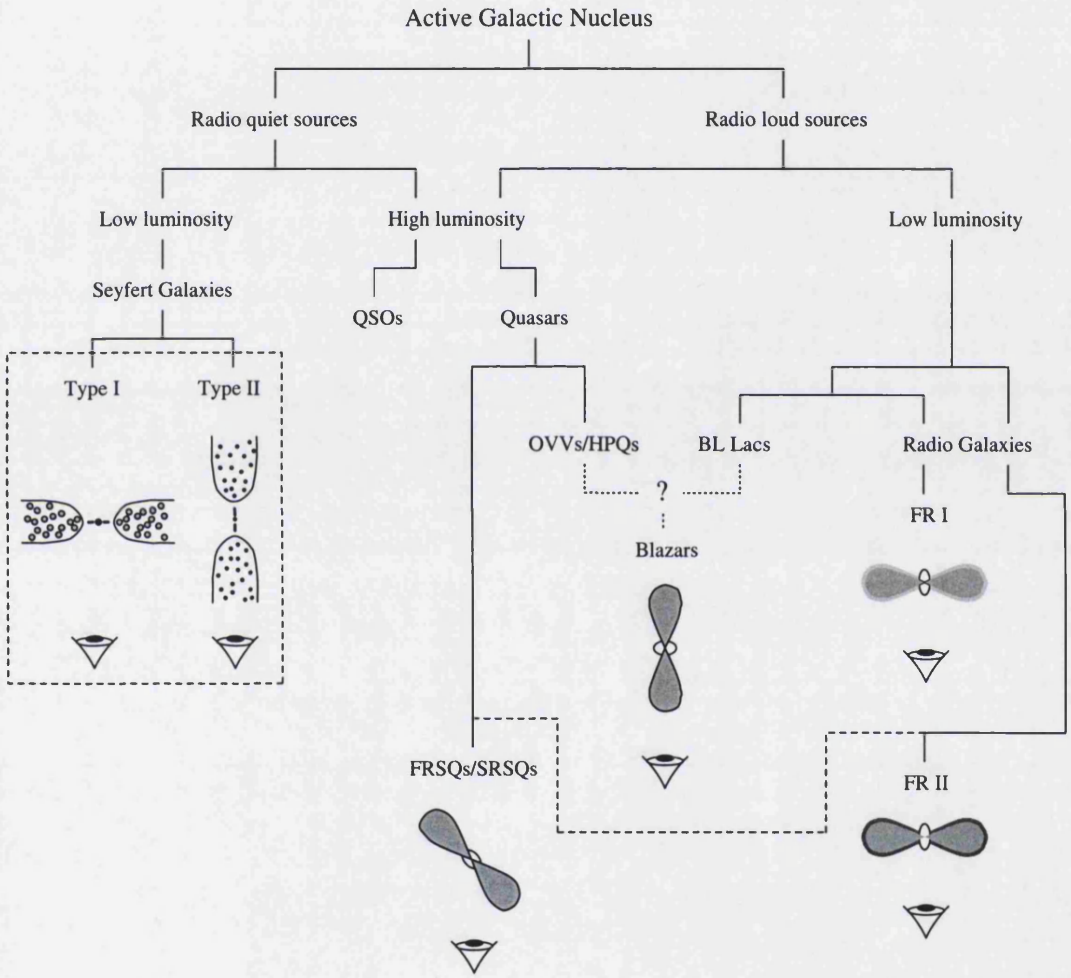

Figure 1.4: A schematic diagram of the subdivisions in the AGN family(*credit* : A. Lawson 1995, Ph.D Thesis).

1.3 Emission mechanism

In this section I briefly discuss the emission mechanism (relevant to this thesis) that can give rise to radio to X-ray radiation.

1.3.1 Thermal black body emission

Electromagnetic radiation emitted by an object in thermal equilibrium with its surroundings is called blackbody radiation. A blackbody is a theoretical object that absorbs all radiation incident on it and does not reflect or transmit any energy. To be in a steady state the blackbody emits the same amount of energy that it absorbs and the re-radiated spectrum is characteristic of the radiating system and depends only upon its temperature. The power per unit area per unit frequency per unit solid angle produced by a blackbody at a certain temperature T is given by Plancks Radiation Law:

$$B_\nu(T) = \frac{2h\nu^3}{c^2} \frac{1}{e^{(h\nu/kT)} - 1} \tag{1.1}$$

where ν is the frequency, c is the speed of light, k is the Boltzmann's constant and h is the Planck constant. As the temperature of the blackbody increases, the total energy emitted (summed over all frequencies and solid angles) per unit time increases rapidly and is represented by the Stefan-Boltzmann Law

$$E = \sigma T^4 \tag{1.2}$$

where σ is the Stefan-Boltzmann constant and T is the temperature in Kelvin . The peak wavelength emitted depends upon the temperature of the blackbody and is represented by,

$$\lambda_{max} = \frac{0.2897}{T} \tag{1.3}$$

where λ_{max} is the wavelength in cm and T is the temperature in Kelvin. Thus, the hotter the object the shorter is the wavelength at which most of the the energy is radiated.

Although no real object is a perfect blackbody, the blackbody curve is, in many cases a good approximation to reality and its properties serve as useful tools for our understanding of the behaviour of real objects. Astrophysical sources that emit thermally in a steady state exhibit blackbody spectra. However, thermal sources can also emit by bremsstrahlung (e.g. clusters; see § 1.3.4)

1.3.2 Compton scattering

Scattering of photons by charged particles is called Compton scattering. The scattering cross section of nuclei is much smaller than that of electrons,

$$\frac{\sigma_N}{\sigma_e} \approx \left(\frac{m_e}{m_N}\right)^2 \tag{1.4}$$

therefore Compton scattering by nuclei is not significant for astrophysical sources and can be neglected. Scattering of the incoming photon off an electron results in a change in the original energy and direction of the photon. If the energy of the electron is much smaller than that of the incoming photon the electron gains energy from the photon and the scattered photon has an energy (hence frequency) lower than the incoming photon. This is generally referred to as the 'recoil effect'. The scattering cross section is the Klein-Nishina cross section σ_{K-N}.

When a low energy photon scatters off an energetic electron, the photon gains energy from the electron. This process is called Inverse Compton scattering (IC). When the up-scattering electrons are thermal (non-relativistic) and $h\nu < 4kT_e$ the energy gained by the photons is given by

$$h\nu_f = h\nu_i exp\left(\frac{4kT}{m_e c^2}N\right) \tag{1.5}$$

where N is the number of scatterings $\sim \tau^2$, and $h\nu_i$ and $h\nu_f$ are the initial and final photon energies respectively.

In the case of relativistic electrons γ h $\nu << m_e c^2$, where, $\gamma = 1/(1-(v/c)^2)^{1/2}$ is the Lorentz factor for the ultra relativistic electrons, the scattering cross section is independent of the photon energy and is approximately equal to the Thompson scattering cross section (σ_T). The energy gained by the photons as a result of Compton up-scattering depends on the Lorentz factor of the scattering electrons and is given by

$$h\nu_f = \gamma^2 h\nu_i \tag{1.6}$$

where, $h\nu_i$ and $h\nu_f$ are the initial and final photon energies respectively. The power radiated in the Inverse Compton process is given by

$$P_{IC} = -\frac{dE}{dt} = \frac{4}{3}\sigma_T c\beta^2\gamma^2 U_{ph} \tag{1.7}$$

$$P_{IC} \propto \gamma^2 U_{ph} \tag{1.8}$$

where U_{ph} is the energy density of the photon field ("particle view" of an electromagnetic field). The Inverse Compton process can produce substantial fluxes of photons in the optical to X-ray region and is very important in the context of astrophysical sources.

1.3.3 Synchrotron radiation

Synchrotron radiation is electromagnetic radiation produced by relativistic charged particles accelerated in an external magnetic field. The total power radiated by a single electron is given by

$$P_{sync} = -\frac{dE}{dt} = \frac{4}{3}\sigma_T c\beta^2\gamma^2 U_B \tag{1.9}$$

$$P_{sync} \propto \gamma^2 U_B \tag{1.10}$$

where $U_B = B^2/2\mu_o$ is the energy density of the electromagnetic field (seen as "wave"). The power emitted in the Synchrotron and Inverse Compton processes is very similar,

$$\frac{P_{IC}}{P_{sync}} = \frac{U_{ph}}{U_B} \tag{1.11}$$

In other words IC and synchrotron are same physical processes described in different ways.

The power radiated by a single electron can also be expressed as proportional to the square of the magnetic field and the electron energy

$$-\frac{dE}{dt} \propto B^2E^2 \tag{1.12}$$

where B is the magnetic field strength and $E = \gamma mc^2$ is the energy of the relativistic electron. The peak of the radiation emitted by a single electron occurs at the critical frequency $\nu_c = \gamma^2\nu_g$ (ν_g is the gyro frequency of the electron) and is proportional to the magnetic field and the square of the electron energy.

$$\nu_c \propto E^2B \tag{1.13}$$

Synchrotron emission is strongly beamed and is concentrated in a narrow cone of half angle $1/\gamma$ in the direction of motion of the electron (which is perpendicular to the acceleration) and is linearly polarised.

For a power-law distribution of electrons $N(E)dE = kE^{-p}dE$ where $N(E)dE$ is the number of electrons per unit volume in the energy interval E *to* $E+dE$ the emissivity is given by

$$J(\nu) \propto kB^{(p+1)/2}\nu^{-\alpha} \propto \nu^{-\alpha} \tag{1.14}$$

where p is the power-law index of the electron energy spectrum and $\alpha = (p-1)/2$ is the spectral index of the synchrotron emission.

The absorption process corresponding to the synchrotron emission process is called synchrotron self absorption (SSA) whereby the photons emitted by the relativistic electrons gyrating in a homogeneous magnetic field are absorbed by other

electrons in the vicinity which gain further energy. Since high densities and low energy photons are required for synchrotron self absorption to occur this process modifies the synchrotron spectrum at low frequencies and is conventionally thought to be responsible for the low energy cut-offs observed at radio, millimeter and centimeter wavelengths in AGN. The flux density (S_ν) in the self absorbed part of the spectrum is given by

$$S(\nu) \propto \frac{\theta^2 \nu^{5/2}}{B^{1/2}} \propto \nu^{5/2} \tag{1.15}$$

where θ is the square root of the solid angle Ω subtended by the source, $\Omega \approx \theta^2$

1.3.4 Bremsstrahlung or free-free emission

An accelerated charged particle emits electromagnetic radiation. Bremsstrahlung means 'braking' radiation and is produced when a free electron is accelerated in the static electric field of an atomic nucleus. For a Maxwellian distribution of electron velocities the total thermal bremsstrahlung emission per unit volume and time can be written as

$$\frac{dP_B}{dV} \propto T^{1/2} N_e N_z Z^2 g_B(T) \tag{1.16}$$

where, N_e is the electron density, N_z is the ion density and g_B is the gaunt factor.

A power-law distribution of electrons gives rise to non-thermal bremsstrahlung. For a flux density $N(E) = N_0 E^{-s}$ of non-thermal electrons, the spectral emission per unit volume can be written as

$$\frac{dP_B}{dV d\nu} \propto Z^2 N_z N_0 \frac{E^{-s-1}}{s} \tag{1.17}$$

where, $E = h\nu$ is the photon energy. Free-free emission is dominant over radiative recombination at temperature $T > 10^7$ K.

1.3.5 Radiative recombination

When a free electron with energy W is captured by an ion with a vacant bound state with binding energy $I_{Z-1,n}$ a photon is emitted with energy $E = W + I_{Z-1,n}$. The excited ion then relaxes in a downward cascade. This process gives rise to line and continuum emission with edges at the ionisation energies of different elements in the gas. Line radiation dominates at $T < 5\times10^6$ K while radiative recombination is dominant only at $T < 10^6$ K.

1.3.6 Line emission

X-ray line emission in hot optically thin astrophysical plasmas occurs when an ion or atom in an excited state decays via downward radiative transitions of electrons from higher energy levels to lower energy levels.

The fluorescence line emission is emitted when one of the two K shell (i.e. n = 1) electrons is ejected following photo-electric absorption of X-rays or inelastic Coulomb collisions with other electrons. The resulting excited atom can decay either via a L shell (n = 2) electron dropping into the K shell and releasing a photon or by the release of an Auger electron. The latter process can also be seen as the absorption of the photon released in the n = 2 to n = 1 transition by another electron which is ejected out of the atom.

Line emission from H-like and He-like ions is by capture of free electrons i.e. by the radiative recombination process described above.

1.4 X-ray emission in AGN

AGN emit over a wide frequency range from the radio to γ-rays however, a large fraction of their energy is released in the optical/UV and X-ray region. Since these objects are thought to be powered by the release of gravitational potential energy via viscous and turbulent dissipation in an accretion disk around a black hole, a

thorough understanding of the physics and spectra of accretion disks is required, to understand the emission mechanisms responsible for their energy output. The first major advance in the understanding of accretion disks came through the 'standard disk model' proposed by Shakura & Sunyaev (1973) and subsequently developed by several other authors (Pringle 1981, Novikov & Thorne 1973). This is a one-dimensional model (i.e. H (thickness of the disk) << R (the radius)) and only the radial structure of the disk is studied in detail. All other properties of the disk are assumed to be independent of azimuthal angle and time and are averaged in the vertical direction. The viscosity of the material in the disk is parameterised by the viscosity parameter α. The gas rotates with Keplerian angular momentum which is transported radially outwards by viscous stress and the disk spectrum at every radius is assumed to be black body radiation with a local effective temperature T_{eff}.

The standard disk model was found to be in fair agreement with the observed spectral energy distribution of AGN in the optical to UV region (Malkan & Sargent 1982, Shields 1978) but not the X-rays. The broad band spectral energy distribution in AGN shows a broad bump (popularly known as the Big Blue Bump) between optical and soft X-ray energies (Walter & Fink 1993) and a hard X-ray power-law at E > 1 keV, with roll-over energies of several hundreds of keV (Zdziarski 1995). The observed hard power-law X-ray emission cannot be reproduced by the standard disk model nor can the observed optical to soft X-ray spectra be fit simultaneously for disk luminosities $\leq L_{Edd}$. If the observed UV emission comes from the innermost regions of the disk and the turnover at around 2000 $\AA$ is indicative of the peak disk temperature, the standard disk model predicts soft X-rays much lower than observed.

Several authors attempted to modify the standard disk theory, so as to distort the accretion disk spectrum at higher energies. Inclusion of Comptonisation effects within the disk, in the vertical direction and general relativistic effects allows for higher X-ray emission, in better agreement with the observations (Czerny & Elvis 1987, Sun & Malkan 1989, Laor & Netzer 1989, Ross et al. 1992). However,

these models still cannot reproduce the hard X-ray emission nor reproduce the observed soft X-ray photon indices ($\Gamma \sim 2.4{-}2.6$; where $\Gamma = \alpha + 1$ and $F(\nu) \propto \nu^{-\alpha}$) for the obvious reason that the high energy tail of these models falls off exponentially (Laor et al. 1997, Walter & Fink 1993). Observations of near simultaneous changes in the X-rays and the UV lines and continuum (NGC 5548; Clavel et al. 1992) further challenged the model in which the optical/UV to soft X-ray emission was entirely produced by viscous dissipation in an accretion disk and instead pointed towards an X-ray illuminated disk (Ross & Fabian 1992).

In order to explain the power-law X-ray emission in AGN Haardt & Maraschi (1991, 1993) proposed a two phase model where the cold phase – the UV emitting standard accretion disk is covered by a hot phase modeled as a Comptonising corona, responsible for the hard X-ray emission. In this model, half of the isotropically emitted X-rays from the corona escape towards the observer and the other half are directed towards the disk, where they are absorbed and re-radiated as UV emission. This emission again enters the corona, cooling the electrons, thus creating a coupling between the cold and the hot phase, whereby the coronal heating rate is balanced by the cooling rate, thus giving rise to the observed almost universal photon index. Although this model requires the dissipation of almost all the gravitational energy in the corona instead of the disk it has been extremely successful mainly because of its ability to reproduce the narrow range of photon indices commonly observed in Seyfert galaxies ($\Gamma \approx 1.95 \pm 0.15$; Nandra & Pounds 1994).

The *full* corona model predicts equal UV and X-ray luminosities since approximately half of the hard X-rays are reprocessed into UV radiation. This is not compatible with observations which show UV luminosity in AGN to be comparable or a few times higher than the X-rays (Elvis et al. 1994). To account for the additional observational constraints Haardt, Maraschi & Ghisellini proposed the *patchy* corona model. The patchy structure of the corona is due to the presence of magnetic loops which are expected to form in turbulent accretion disks where the strongly ionised plasma is rotating differentially. Reconnection events transfer

the energy stored in these magnetic loops to the plasma within the flux tubes, thus producing hot active regions, the "*patches*" in the corona. The energetic particles resulting from reconnection events produce X-rays by Compton up-scattering of the soft photons, mainly from the disk. In this model the X-ray sources are separate active regions and some fraction of the disk emission (intrinsic and reprocessed) can escape directly towards the observer thus making a larger L_{UV}/L_X ratio possible. The L_{UV}/L_X ratio is determined by the fraction f (≤ 1) of the total gravitational energy dissipated in the corona.

The two phase model (cold disk illuminated by an X-ray source above) has been very successful in explaining the X-ray features in AGN. However, an alternative, the Advection Dominated Accretion Flows model (ADAF; Abramowicz et al. 1995, Narayan & Yi 1994) has generated a lot of interest in recent years. In this model the inner accretion disk is composed of just a single hot phase and is geometrically thick (i.e. the disk scale height H is comparable to the local radius R). The gas is optically thin and is significantly hotter than that in the Shakura & Sunyaev (1973) solution. The accretion disk plasma is two temperature with the ions being significantly hotter than the electrons and as such it does not radiate as efficiently as the optically thick Shakura-Sunyaev disk. In this model it becomes possible for viscously generated energy to be advected into the black hole rather than released through radiation as the advective energy flux is larger than in the standard disk theory.

Although this model agrees qualitatively with X-ray observations of some sources, mainly Galactic Black Hole Candidates (Wilms et al. 1999, di Salvo et al 1998), it has its drawbacks. Observations of strong Fe K_α lines with extended red wings in the X-ray spectra of several AGN does not support the ADAF scenario. The model is also unable to explain the radio observations of low luminosity giant elliptical galaxies which are thought to be promising candidates for the presence of ADAF. The observed radio flux in these galaxies is much lower than that predicted by the ADAF model (de Matteo et al 1999) and the observations of flat radio cores ($\alpha \approx 0$) seriously conflict with model predictions of highly inverted radio cores (Falcke et

al. 2001).

X-ray observations by very low resolution detectors like OSO-8 and Ariel-V established a power-law shape for the X-ray continuum in the early seventies (Mushotzky 1978, Stark et al. 1977, Barr et al. 1977, Ives et al. 1976). However, the relative increase in sensitivity of subsequent detectors revealed additional features, like spectral hardening at X-ray energies $\gtrsim$ 10 keV and Fe K_α lines at 6.4 keV (Nandra 1991, Matsuoka et al. 1990) which were too strong to be accounted for by material in our line of sight (Inoue 1990). The Compton reflection model (Lightman & White 1988, George & Fabian 1991) explained these observations by suggesting that the 6.4 keV line and the flattening of the high energy spectrum could be a result of reflection of the primary power-law X-ray emission in a dense, optically thick material of constant density in the vertical direction (possibly an accretion disk) subtending a large solid angle to the illuminating source. According to this model an X-ray photon entering an optically thick material is either Compton scattered by electrons or undergoes photo-electric absorption followed by either Auger de-excitation or fluorescent line emission. Most of the lower energy photons (E $<$ 2 keV) are photo-electrically absorbed in the material due to the high abundance of medium-Z elements like C, N, O. The elemental abundances decrease with increasing Z, which results in fewer higher energy photons being absorbed and the reflection albedo increases towards higher energies. At energies greater than $\sim$ few tens of keV Compton recoil and reduction of scattering cross section leads to a drop in the number of photons being reflected. These effects give rise to a hump-like feature peaking at $\sim$ 20$-$30 keV which is thought to be responsible for the spectral hardening observed in AGN, at E $\gtrsim$ 10 keV. In addition there is fluorescence line emission (mostly K_α) from abundant elements with Fe K_α being the strongest. The Compton reflection model has been able to reproduce the (relatively low signal to noise) high energy spectra of Seyfert galaxies obtained by observatories like *GINGA*, *RXTE* and *BeppoSAX*. The inferred solid angle of the reflecting material (from model fits to *GINGA* data) as seen by the X-ray source is found to be a large fraction of 2π (Pounds 1990,

Nandra 1991). This along with the observations of broad iron lines provides further support for the geometry in which the X-ray source is placed above a plane of dense, optically thick material extending down to almost $3R_g$ (i.e. an X-ray illuminated disk).

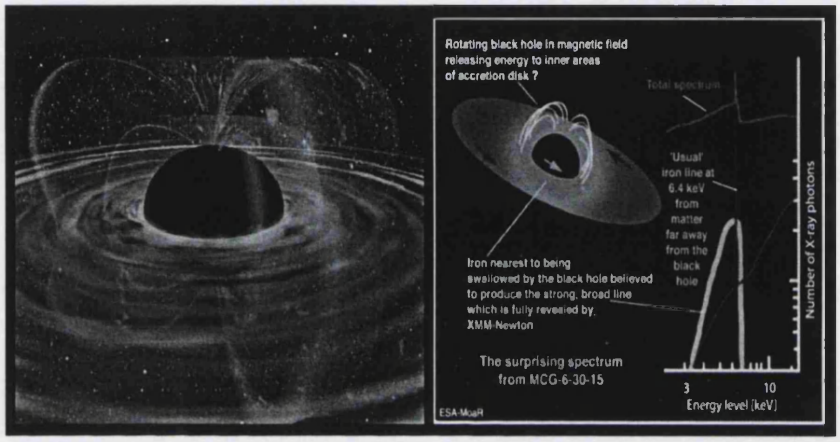

Figure 1.5: A schematic diagram of the innermost regions of the accretion disk (left) and on the right the X-ray spectrum showing the broad Fe K_α line from the accretion disk around black holes (*credit* : ESA image archive)

The presence of Fe K_α lines in a majority of Seyfert 1s was established by the *GINGA* observations. However, it was the *ASCA* observatory, that resolved the Fe K_α emission in one Seyfert 1 galaxy, MCG-6-15-30 (Tanaka et al. 1995). The line profile was found to be broad ($v \sim 0.3c$) and asymmetric with an extreme red extension down to 3 keV. The observed Fe K_α emission in MCG-6-30-15 was in good agreement with an iron line profile expected from a disk around a maximally rotating Kerr black hole (Laor 1991), indicating emission from within 6 R_g. The skewed Fe K_α profile in MCG-6-15-30, displaying characteristic relativistic distortions expected from around a region of extreme gravity, is one of the best pieces of evidence we have in the favour of black holes at the centers of AGN. Broad iron lines were subsequently detected in several other Seyfert 1 galaxies with *ASCA* and appeared

to be a common feature in the X-ray spectra of these sources. The Fe K_α lines showed core energies close to 6.4 keV, broad red wings and relatively little flux blueward of 6.4 keV (Nandra et al 1997). The shape and the strength of the iron lines also appeared to change with luminosity, with the line equivalent width decreasing with increasing source luminosity (Nandra et al 1997).

Currently, there is some uncertainty regarding broad iron lines in *ASCA* data. Re-analysis of data by Lubinski & Zdziarski (2001) suggests that the iron lines in *ASCA* may be narrower and weaker than had originally been thought, maybe due to changes in calibration. However, this claim has been strongly disputed by Yaqoob et al. (2001), who show that the changes in *ASCA* calibration have had an insignificant effect ($\leq$ 8%) on the velocity widths and equivalent widths of Fe K_α lines. They argue that a simple Gaussian model is inadequate to describe the complex iron line profiles in some sources, and that the findings of Lubinski & Zdziarski (2001) are probably a result of incorrect modeling of data.

Observations of ionised iron lines with EW much larger than that predicted by the Compton reflection model (EW $\sim$ 50$-$150 eV; George & Fabian 1991) suggested that the accretion disks in at least some AGN may not be neutral and instead, may be heavily ionised. When an accretion disk is illuminated from above the ionisation structure of the disk is likely to be affected by the intensity of the X-ray illumination. It is also expected that some of the incident radiation will be Compton reflected and some will be reprocessed by the disk. In recent years reflection models have been improved by relaxing the assumption of constant density and instead computing the density via the condition of hydrostatic balance and including the effects of reprocessing in the disk in a self consistent manner along with Compton reflection (Nayakshin et al. 2001, Ballantyne et al. 2002). Although the details of individual model calculations vary they all predict the existence of a highly ionised skin on top of the accretion disk with trace abundances of H-like and He-like ions from low to medium-Z elements and iron-L species. The temperature of the skin ranges between 10^6-10^8 K depending on the strength of the ionising continuum (Nayakshin

et al. 2000, Nayakshin et al. 2001). These models predict that the presence of a hot ionised layer on top of the accretion disk would give rise to H-like and He-like recombination X-ray lines from medium-Z elements and ionised species of iron in addition to the fluorescence lines.

The limited resolution and sensitivity of previous detectors did not allow these advanced models to be tested against observations. However, the high resolution and signal to noise *XMM − Newton* and *Chandra* data allows for a meaningful comparison of data with models which will provide us with valuable insights into the ionisation structure of the accretion disk and the physical conditions in the inner regions of AGN. The reflection model by Nayakshin et al. 2001 also provides an opportunity to test two different geometries of the X-ray source with respect to the reflecting material: the lamppost model, where the inner disk is assumed to be evenly illuminated by a point-like X-ray source high above the black hole and the magnetic flare model, where the disk is assumed to be unevenly illuminated by separate X-ray sources close to the disk surface (i.e. active regions). This should allow us to obtain better constrains on the structure and geometry of the region closest to the black hole.

An important question is, whether the central engine in all AGN is fundamentally similar or not. X-ray emission, relativistic jets and superluminal motion are phenomena that occur close to the central black hole and can be used to probe the structure and conditions in the innermost regions of AGN. In this thesis I have used new XMM-Newton data along with data from other observatories to study the geometry and the energy generation mechanism in the inner regions of AGN.

In chapter 2, the X-ray observatories, from which data have been used in this thesis are discussed briefly. In chapter 3, I study the X-ray to radio emission in III Zw2: a luminous ($L_{2-10} \sim 10^{45}$ erg s^{-1}) radio-intermediate quasar (i.e. intrinsically radio weak but with relativistic jets pointed straight at the observer), over a period of 25 years. I use the X-ray and multi-wavelength, spectral and variability information to understand the dominant emission mechanism in this source. The

broadband X-ray emission (0.3−100 keV) in a bright ($L_{2-10} \sim 10^{44}$ erg s^{-1}) radio quiet Seyfert 1 Galaxy MCG-2-58-22 is studied in chapter 4. I compare the X-ray data with advanced reflection models incorporating Compton reflection and re-processing of X-rays in an accretion disk in a self consistent manner. In chapter 5, I study the rapidly variable X-ray emission in a low luminosity ($L_{2-10} \sim 10^{40-41}$ erg s^{-1}) narrow line Seyfert 1 Galaxy NGC 4051. Time resolved spectra are used to better understand the properties of various components in the X-ray emission of NGC 4051. The long and the brief low states of NGC 4051 are compared and discussed. In chapter 6, I discuss how the findings of chapter 3, 4 and 5 have contributed to our understanding of the AGN phenomenon. The results of this thesis are summarised in chapter 7.

Chapter 2

X-ray observatories

In this chapter I briefly discuss the X-ray observatories from which data have been used in this thesis, starting with the oldest X-ray mission *Einstein* and moving forward to most recent $XMM - Newton$ observatory.

2.1 Einstein

$HEAO - 2$ (renamed *Einstein* after launch) was the second of NASA's three High Energy Astrophysical Observatories and was launched on 1978 November 12 into a low Earth orbit by an Atlas-Centaur rocket and was operational up to 1981 April. It was the first imaging X-ray telescope in space with an active attitude control system capable of arcminute pointing and had an energy range of 0.2−20 keV. Its sensitivity was several 100 times greater than any mission before it, which combined with its field of view of tens of arcminutes and few arcsecond angular resolution made it possible, for the first time to image extended objects, diffuse emission, and to detect faint sources.

Its payload consisted of a Wolter Type-I grazing incidence telescope with an energy range of 0.1−4 keV. Four different detectors could be rotated into its focal plane one at a time:

- The High Resolution Imager (HRI) was a digital X-ray camera which was

sensitive over the 0.15−3 keV range. It had an effective area of 5−20 cm^2 and provided high temporal (8 ms) and spatial ($\sim$ 2" within 5' of the axis) resolution over a 25' field of view. It had no intrinsic spectral resolution but spectral information could be obtained using the interchangeable broad band filters and the Objective Grating Spectrometers (OGS).

- The Imaging Proportional Counter (IPC) was a position sensitive proportional counter with an energy range of 0.4−4 keV. It provided full focal plane coverage, good efficiency and low spatial and spectral resolution. It had a 75' field of view with an effective area of 100 cm^2 and $\sim$ 1' spatial resolution.

- The Solid State Spectrometer (SSS) had an energy range of 0.5-4.5 keV and energy resolution $\Delta E/E$ of 0.3−0.04. It had a narrow field of view of 6' with an effective area of 200 cm^2.

- The Focal Plane Crystal Spectrometer (FPCS) operated in the 0.42−2.6 keV range and had a small effective area of 0.1−1 cm^2.

The Monitor Proportional Counter (MPC) was a collimated proportional counter and was a non-focal plane instrument. It was co-aligned with the X-ray telescope and monitored the 1.5−20 keV X-ray flux of sources that were being simultaneously observed by the focal plane instruments. It had a circular field of view of 1.5° diameter (FWHM) with an effective area of 667 cm^2 and an energy resolution of $\Delta E/E$ = 0.2 at 6 keV. *Einstein*, the first imaging observatory was a key X-ray mission and its scientific discoveries provided a major stepping stone towards understanding X-ray emission in the universe.

2.2 EXOSAT

The European Space Agency's (ESA) *EXOSAT* satellite was launched on 1983 May 26 from the Vandenberg complex in the USA into a highly eccentric orbit (e $\sim$

0.93) with an inclination of 73° and a period of 90.6 hours. The orbit of *EXOSAT* was quite different from that of any previous X-ray astronomy satellite and allowed for uninterrupted observations for almost 76 hours. Also the satellite was visible from the ground station during the entire observational period and on-board data storage was not required. This spacecraft was operational for almost three years and re-entered the atmosphere on 1986 May 6 following a natural decay of orbit caused by the failure of the attitude control system.

The scientific payload consisted of three instruments, the Low Energy instrument (LE), the Medium Energy instrument (ME) and the gas scintillation proportional counter (GSPC) which allowed observations over a broader energy range of 0.05−50 keV compared to previous detectors. A Channel Multiplier array detector (CMA) could be rotated into the focal plane of each of the two low energy imaging telescopes which were sensitive to 0.05-2.5 keV energy range. The CMA was an imaging detector and had no intrinsic energy resolution in the X-ray band but coarse spectral information could be obtained using the different filters available (analogous to UBV photometry) . It had a large field of view $\sim$ 2 degrees with a small effective area of 10 cm^2. The Medium Energy (ME) instrument consisted of an array of eight proportional counter and operated in the 1−50 keV energy range. It had a 45 arcminute FWHM field of view with a total effective area of 1600 cm^2 and had an energy resolution of $\Delta E/E = 0.2$. The gas scintillation proportional counter, GSPC, (Peacock et al (1981) was sensitive to the 2−20 keV range and provided a factor of 2 improvement in spectral resolution over the ME. However, its effective area was a factor of 20−30 lower than the ME.

2.3 ROSAT

ROSAT (the ROentgen SATellite) a joint venture between Germany, the United States, and the United Kingdom was launched by the United States on June 1,

1990. The mission came to an end in on February 12, 1999 after nine years of operation. The scientific payload consisted of co-aligned X-ray and EUV telescopes which allowed for simultaneous multi-wavelength observations of the sources in the field of view. The X-ray mirror assembly (XMA) consisted of 4 nested grazing incidence Wolter-I mirrors with a focal length of 240 cm. At its focus was a carousel on which there were 2 Position Sensitive Proportional Counters (PSPCs), each with a filter wheel carrying a boron filter, and a High Resolution Imager (HRI). The PSPC's were multi-wire proportional counters with over a 2 degree diameter field of view and were sensitive to the 0.1−2 keV band. Their energy resolution was modest $\Delta E/E = 0.43$ and they provided spatial resolution of $\sim$ 25 arcsecond at 1 keV and relative time resolution down to $\sim$ 130 microseconds. The *ROSAT* High Resolution Imager (HRI) comprised of two cascaded micro-channel plates (MCPs) with a crossed grid position readout system and was similar to the Einstein HRI detector. It had almost no energy resolution but it provided very high spatial resolution of $\sim$ 5 arcsecond FWHM and a relative time resolution down to 61 microseconds over a 38×38 arcminute^2 field of view. The EUV telescope was called the Wide field Camera. It had a 5 degree field-of-view with spatial resolution 2.3 arcminute HEW and the use of various filters at its focus allowed for very crude spectral resolution.

2.4 ASCA

The Advanced Satellite for Cosmology and Astrophysics (*ASCA*), Japan's fourth X-ray astronomy mission was launched on February 20, 1993 in to an almost circular orbit of altitude 520−620 km. It was the first satellite to use charge coupled devices (CCDs) for X-ray astronomy. The scientific payload consisted of four X-ray telescopes with a combined effective area of 1300 cm^2 (600 cm^2) and field a of view of 24' (16') at 1 keV (7 keV). At the foci of two of the telescopes were Gas Imaging spectrometers (GIS) which were gas imaging scintillation proportional counters and at the foci of the other two telescopes were Solid-state Imaging Spectrometers (SIS)

which were charge coupled devices. The two GIS detectors (GIS-1 and GIS-2) had a circular field of view of 50' diameter and had an energy resolution of $\Delta E/E = 0.08$ in the 0.7−10 keV. The two CCD cameras (SIS-1 and SIS-2) operated in the 0.4−10 keV range. They had a 22×22 arcminute^2 field of view and a energy resolution of $\Delta E/E = 0.02$ at 5.9 keV. The scientific instruments on board, made ASCA the first X-ray astronomy mission to combine imaging capability with a broad pass band, good spectral resolution, and a large effective area.

Although the solid state detectors (SIS) had better energy resolution (4 times better at most energies), greater low energy ($E < 1.5$ keV) area, and better angular resolution compared to the GIS, their efficiency below 1 keV steadily decreased over time and by late 1994 the discrepancy between the SIS and GIS was as much as 40% at 0.6 keV. Because this could not be corrected by the existing software, SIS data below 1 keV were rendered useless. The attitude control for *ASCA* was lost during a geomagnetic storm in July 2000, after which no scientific observations were performed. After more than 8 years in orbit it re-entered the atmosphere on March 2, 2001.

2.5 The BeppoSAX mission

The X-ray satellite *BeppoSAX* (named in honour of Giuseppe Occhialini), a joint venture of the Italian Space Agency (ASI) and the Netherlands Agency for Aerospace Programs (NIVR) was launched on April 30 1996 from Cape Canaveral into an circular equatorial orbit of 3° inclination and 600 km altitude. The spacecraft was three axis stabilised and weighed 400 kgs. The scientific payload covered more than three decades of energy and was made up of four co-aligned narrow field instruments (NFI) each with a geometric area of 124 cm^2 and imaging gas scintillation proportional counter detectors at their foci and two wide field cameras (WFI) positioned perpendicular to the the NFI and pointed in opposite directions. The Low Energy Concentrator Spectrometer (LECS) was sensitive to the 0.1−10 keV range and had a

field of view of 37 ' diameter. The identical set of three Medium Energy Concentrator Spectrometers (MECS) had a narrower energy range (1.3−10 keV) but a wider field of view of 56'. They had an energy resolution of $\Delta E/E = 0.08$ (comparable to the *ASCA* GIS detectors) and a spatial resolution of 0.7' (Boella et al. 1997) at 6 keV. The HPGSPC was a collimated High Pressure Gas Scintillation Proportional Counter which operated in the energy range of 4-120 keV. The Phoswich Detector System (PDS) was sensitive in the 15−300 keV range and was instrumental in extending the the energy range of BeppoSAX to hard X-rays. The PDS detector consisted of 4 actively shielded NaI(Tl)/CsI(Na) phoswich scintillators with a total geometric area of 795 cm^2. It has no spatial resolution and had a wide field of view of 1.3° (FWHM) and an energy resolution of $\Delta E/E = 0.15$ at 60 keV.

Overall *BeppoSAX* provided simultaneous coverage over a large energy band (0.1−300 keV), imaging with angular resolution at the arcminute level, timing variability on time scales down to the millisecond and low resolution spectroscopy. BeppoSAX required much larger exposures due to its relatively low effective area (150 cm^2 at 6.4 keV) compared to current X-ray missions and suffered from pointing accuracy problems during its lifetime as a result of failing gyros. Its in orbit operations were finally terminated in April 2002 as a result of poor and degrading spacecraft conditions and rapid orbital decay.

2.6 XMM-Newton

The X-ray Multi-mirror Mission ($XMM - Newton$) is the second corner stone in the European Space Agency's (ESA) Horizon 2000 program and was was launched on Ariane 504 on December 10 1999. The satellite is three axis stabilized and has an absolute pointing accuracy of ±1 arcminute. It has a highly eccentric orbit (7000 km perigee, 114000 km apogee) with 40 hour synchronous period which allows for long continuous observations uninterrupted by earth occultations. The inclination (70°) and azimuth (18°) of the orbit is such that it allows for almost continuous

ground station coverage from Europe.

XMM – Newton payload consists of two distinct types of telescopes: three Wolter type-1 co-aligned, high throughput X-ray telescopes with 6 arc second FWHM (15 arc second HPD) angular resolution and a 30-cm Cassegrain optical/UV telescope (the optical monitor (OM)). At the foci of the X-ray telescopes are two types of X-ray instruments: the EPIC (European Photon Imaging Camera) (Strüder et al. 2000; Turner et al. 2000), which is made up of three CCD cameras (MOS1, MOS2, PN), and the dispersive Reflection Grating Spectrometer (RGS) (den Herder et al. 2000). At the focal plane of two X-ray telescopes half of the X-ray beam is diverted to the RGS for high resolution spectroscopy and the other half is focussed on to the EPIC-MOS. The third X-ray telescope is focussed directly on to the EPIC-PN.

The three CCD cameras of EPIC (MOS1, MOS2 and PN) provide very sensitive X-ray imaging capability in the 0.1−15 keV energy range over a 30' field of view with a spectral resolution of $\Delta E/E \sim 0.05-0.02$. The PN camera can also be operated with high time resolution (0.03 ms) in the timing mode. RGS allows for high resolution X-ray spectroscopy ($\Delta E/E \sim 0.005-0.0013$) in the energy range of 0.35−2.5 keV. The optical monitor is sensitive over the 160 - 550 nm spectral range and provides optical/UV images over a 17' field of view, simultaneous with the X-ray observations. It can also be used to obtain low resolution grism spectra of the optical counterparts of sources in the X-ray field of view and for high time-resolution photometry (0.5 s in the fast mode).

XMM – Newton, with its three telescope modules providing the largest effective area ever for a focusing telescope (4650 cm^2 at 1.5 keV), is the most sensitive imaging X-ray observatory in the 250 eV to 12 keV energy range ever flown.

The combination of imaging telescopes with huge effective areas allows us to probe deeper into the universe than ever before. Additionally the simultaneous operations of the high spectral resolution RGS and high angular resolution EPIC

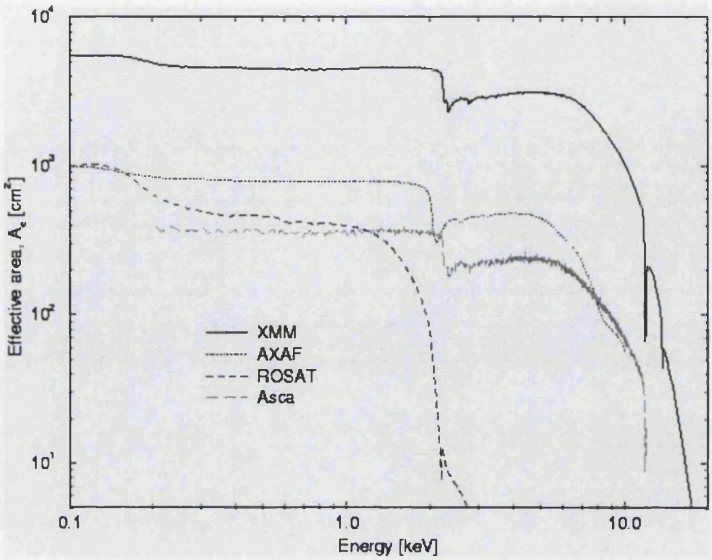

Figure 2.1: A comparison of the XMM-Newton mirror areas with those of of few recent X-ray observatories; *credit* : XMM-Newton users handbook & HEASARC

(CCD) detectors in the X-rays along with simultaneous observations in the optical/UV band with the optical monitor (OM) and long continuous observations of a single source provided by the highly eccentric $XMM-Newton$ orbit allows unique opportunities to study astrophysical objects. The scientific results from this mission are sure to revolutionise our understanding of the universe. Some of the important characteristics of $XMM-Newton$ are compiled in Table 2.1

Instrument	EPIC-MOS	EPIC-PN	RGS	OM
Bandpass	0.15-12 keV	0.15-15 keV	0.35-2.5 keV[1]	160-550 nm
Orbital target vis[2]	5-135 ks	5-135 ks	5-145 ks	5-145 ks
Sensitivity[3]	$\sim 10^{-14}$[4]	$\sim 10^{-14}$[4]	$\sim 8\times10^{-5}$[14]	24 mag[12]
Field of view (FOV)	30'[5]	30'[5]	$\sim$ 5'	17'
PSF (FWHM/HEW)[6]	5"/14"	6"/15"	N/A	$\sim$ 1"
Pixel size	40 μm (1.1")	150 μ m (4.1")	81 μm (9×10^{-3} Å)[13]	0.5" [7]
Timing resolution[8]	1.5 ms	0.03 ms	16 ms	500 ms
Spectral resolution[9]	$\sim$ 70 eV	$\sim$ 80 eV	0.04/0.025 Å[10]	0.5/1.0 nm[11]

Notes:

[1] In the -1. grating order (wavelength range: 5-35 Å)

[2] Total time available for science per orbit; minimum of 5 ks

[3] After 10 ks

[4] In the range 0.15-15.0 keV, in units of erg s^{-1} cm^{-2}

[5] See Figs. 16, 17 and 18 of the XMM-Newton Users handbook for details

[6] See Fig. 4 of the XMM-Newton Users handbook for details

[7] 1" with default binning

[8] In fast data acquisition mode

[9] At 1 keV energy. At the energy of Fe K (6.4 keV), the energy resolution of both EPIC cameras is $\sim$ 150 eV

[10] In -1. and -2. order, resp.; at 1 keV, this corresponds to 3.2/2.0 eV (HEW)

[11] With grism1 (UV) and grism2 (optical), respectively

[12] For a 1000 s white light filter observation of a B0 star

[13] In spectroscopy mode

[14] OVII 0.57 keV line flux in photons cm^{-2} s^{-1}, for an integration time of 10 ks and a background of 10^{-4} photons cm^{-2} s^{-1} keV^{-1}

Table 2.1: An overview of the *XMM – Newton* characteristics. This table has been taken from the *XMM – Newton* Users handbook

Chapter 3

Correlated multi-wavelength emission from the X-ray bright Seyfert Galaxy III Zw2

3.1 Introduction

III Zw2 is a triple galaxy group. The brightest of the group, III Zw2A (also known as Mrk 1501, PG 0007+106) hosts a Seyfert 1 AGN and will be referred to as III Zw2 throughout this thesis. III Zw2 is a bright X-ray source ($F_{0.2-10} \approx 4\times10^{-11}$ erg cm^{-2} s^{-1}, Schnopper 1978) with z = 0.089 (de Robertis 1985) and is the most luminous Seyfert 1 ($L_{2-10} \approx 10^{45}$ erg s^{-1}) in the Piccinotti et al. (1982) sample which is made up of sources with 2–10 keV luminosity $\geq 10^{42}$ erg s^{-1}. Superluminal motion of radio emitting plasma has been observed recently in the source; notably this is the first detection of its kind in a spiral galaxy (Brunthaler et al. 2000). III Zw2 has long been known to show large amplitude flux variations in the radio (Wright et al. 1977; Schnopper et al. 1978; Landau et al. 1980; Aller et al. 1985; Falcke et al. 1999) and the optical (Lloyd 1984, Clements et al. 1995). Variations of smaller amplitude (of less than 50 %), have also been detected in the IR (Lebofsky & Rieke

1980; Sembay, Hanson & Coe 1987) and the UV (Chapman, Geller & Huchra 1985). The X-ray temporal behavior is less well studied, but comparison of observations at different epochs hints that the X-ray flux may vary substantially. The X-ray spectra of III Zw2 obtained by *SAS*-3 (Schnopper et al. 1978), *Ariel* VI (Hall et al. 1981) and the *Einstein* SSS (Petre et al. 1984), can be described by power-laws with photon indices $\Gamma = 1.3-1.7$, and neutral absorption consistent with that of the line of sight Galactic column density. No soft X-ray excess has been detected in this source.

In this chapter I study the X-ray to radio emission in III Zw2 over a period of 25 years, from 1975 to 2000. I discuss the different X-ray observations, starting with the most recent *XMM – Newton* observation in July 2000 and going back to the *SAS*-3 observation of 1977. I present an analysis of the X-ray spectra of III Zw2 taken by 4 different observatories and examine the short and long term temporal variations in X-ray flux (§3.2). I also present the multi-wavelength light curves and Spectral Energy Distribution (SED) incorporating data from 1975 - 2000 (§3.3) and discuss the emission mechanisms in the source (§3.4).

3.2 X-ray emission

3.2.1 Observations

III Zw2 has been observed in the X-ray band fifteen times during the last three decades (see Table 3.1 for details). To build up a reliable X-ray history for this source I have only considered data with good positional resolution i.e. data taken with an imaging telescope or the *SAS*-3 Rotating Modulation Collimater (RMC). This is because of the presence of a bright X-ray source, HD 560, approximately 12' from III Zw2. This source may have been responsible for the contamination of the non-imaging *EXOSAT* ME flux measurements of III Zw2 in 1985 (Tagliaferri et al. 1988).

Date	Instrument	Energy (keV)	Spectra	Exposure (s)	Rate (cts s^{-1})	Flux 1-2 keV (erg cm^{-2} s^{-1})
2000 Jul 04	XMM-Newton MOS	0.1-10.0	Y	7500	1.078	1.910e-12
	XMM-Newton PN	0.1-10.0	Y	10152	2.740	1.910e-12
	XMM-Newton RGS	0.3-2.3	Y	16000	0.119	1.830e-12
1997 Jul 01	ASCA SIS	0.4-10.0	Y	40352	0.41	3.100e-12
	ASCA GIS	0.7-10.0	Y	43744	0.360	3.100e-12
1994 Dec 26	Rosat HRI	0.1-2.0	N	2605	0.089	1.460e-12
1994 Jun 16	Rosat HRI	0.1-2.0	N	1601	0.205	3.370e-12
1992 Jul 18	Rosat PSPC	0.1-2.0	Y	9013	0.288	1.800e-12
1992 Jun 12	Rosat PSPC	0.1-2.0	Y	9111	0.314	1.960e-12
1990 Dec 22	Rosat PSPC	0.1-2.0	N	563	0.480	2.840e-12
1985 Dec 20	EXOSAT LE (*Lx3*)	0.05-2.0	N	14948	0.036	1.080e-11
1985 Nov 30	EXOSAT LE (*Lx3*)	0.05-2.0	N	16655	0.028	8.370e-12
1985 Aug 18	EXOSAT LE (*Lx3*)	0.05-2.0	N	5847	0.038	1.136e-11
1983 Dec 18	EXOSAT LE (*Lx3*)	0.05-2.0	N	4521	0.013	3.887e-12
1980 Dec 19	Einstein IPC	0.4-4.0	Y	4233	0.077	7.950e-13
1980 Jan 9	Einstein IPC	0.4-4.0	Y	3270	0.365	2.960e-12
1979 Jun 21	Einstein IPC	0.4-4.0	Y	805	0.772	6.210e-12
1977 Aug 17-22	SAS-3 (RMC)	2.0-11.0	N	-	-	7.580e-12

Table 3.1: X-ray observations of III Zw2 over a period of 25 years, from 1975 to 2000. The 1−2 keV model flux has been obtained from power-law spectral fits. For data with no spectral information, count rates have been converted to flux via the *PIMMS* flux converter assuming a power-law spectral model using $\Gamma = 1.7$ and $N_H = 5.72 \times 10^{20}$ cm^{-2}.

XMM-Newton

III Zw2 was observed with *XMM − Newton* (Jansen et al. 2001) on 2000 July 4. MOS data were taken in the full frame mode while the PN data were taken in small window mode. Thin filters were used in all three EPIC cameras. EPIC data were reduced using the *XMM − Newton* Standard Analysis System (SAS), version 5.2. Source spectra and light curves from the MOS and PN detectors were extracted using circles of radius 2' with pattern 0-12 (MOS) and 50" with pattern 0 (PN) in *XMMselect*. The background spectra and light curves were extracted using circular apertures from a source free region on the same chip.

RGS data were reduced using *XMM − Newton* SAS V5.0.1. The data were further processed by M. Page, to obtain the final combined RGS spectrum (RGS1 + RGS2) using his own recipe, which is as follows. Source spectra are extracted from spatial region containing 90% of the source flux in the cross dispersion direction. First and second orders are selected from pulse height-dispersion regions containing 95% of the source counts. Background spectra are obtained using the same order-sorting regions as for the source, but spatial regions excluding 95% of the source flux in the cross dispersion direction. First and second order background subtracted spectra from RGS1 and RGS2 are re-sampled to match the first order RGS1 spectrum and added together. The corresponding response matrices are divided by the data/model ratio of a power-law fit to the RGS spectra of the continuum source Mrk 421 to correct systematic residuals in the effective area calibration. The response matrices are then re-sampled and combined into a single response matrix. Finally, the RGS spectrum is grouped by a factor of 10 to improve signal to noise.

Archival data

Archival data from *ASCA*, *Rosat*, *EXOSAT* and *Einstein* observatories were also included in this study. The *Xselect* software was used to generate all spectra and light curves. Background spectra and light curves were extracted from source free

regions using circular apertures.

The *ASCA* (Inoue 1993), GIS (Gas Imaging Spectrometer: hereafter GIS2 and GIS3) data in high bit rate mode and the SIS (Solid-state Imaging Spectrometer: hereafter SIS0 and SIS1) data in bright2 mode were screened using ASCASCREEN applying the standard screening criteria. FTOOLS were used to apply dead time correction and to generate the response matrices. Source spectra and light curves were extracted using a circle of 6' radius.

I analyzed data from the *ROSAT* Position Sensitive Proportional Counter (PSPC) (Briel et al. 1989; Pfeffermann et al. 1987), which was an imaging spectrometer and the High Resolution Imager (HRI) (Harris et al. 1990). Spectra and light curves were extracted from the PSPC data using a source circle of 2'. The All Sky Survey (Voges et al. 1999) count rate of Dec 1990 22 was obtained from the Rosat archives. The HRI data have no useful energy resolution but have a spatial resolution of $\sim$ 5" and were used to generate source and background light curves using a circle of 1.3' radius.

EXOSAT observations of III Zw2 were made using both the LE (Low Energy) and the ME (Medium Energy) detectors (Andrews 1984; Bleeker et al. 1975; Turner et al. 1981). For my analysis, I have used the LE imaging Channel Multiplier Array (CMA) data. Different LX3 filter exposures for each observation were merged and corrected for dead-time using the FTOOL Tkexomerge and cmadead respectively. Count rates for the LX3 filter exposures were determined (from the merged file) using a circle of 1.5' radius.

Spectra and light curves from the *Einstein* Imaging Proportional Counter (IPC), were extracted from screened event lists using a circle of 1' radius.

The X-ray flux for the SAS-3 observation is taken from Schnopper et al (1978). The $SAS-3$ 90% error circle on the position of III Zw2 has a radius of 40". This uncertainty is small enough to safely exclude the possibility of flux contamination of III Zw2 from the X-ray source 12' away.

3.2.2 X-ray spectra

Spectral fitting of X-ray data was done using the XSPEC software package version 11.1. All emission line energies quoted in the text are in the rest frame of the source and errors are quoted at 90% confidence level ($\Delta\chi^2 = 2.7$ for one interesting parameter) unless specified otherwise. Spectral fitting results are summarized in Table.4.3.

XMM-Newton

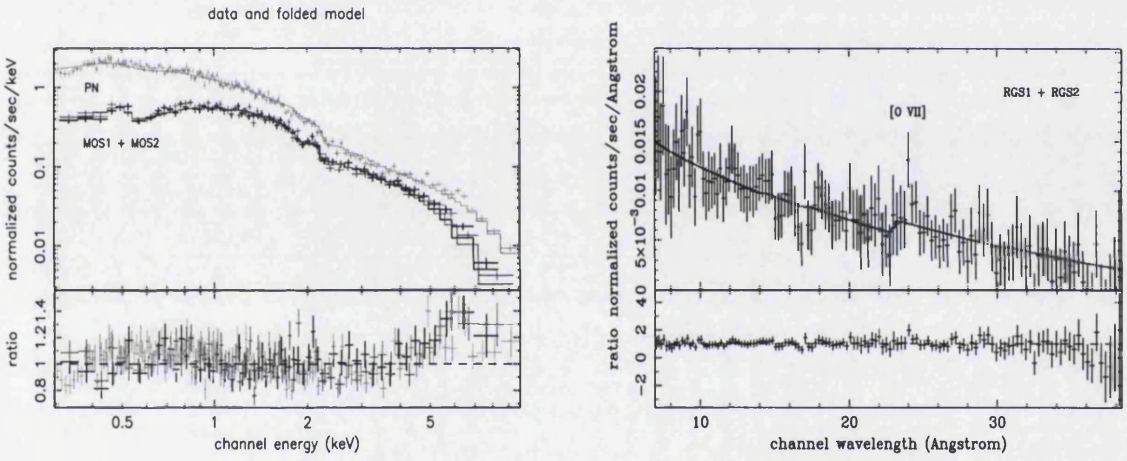

Figure 3.1: *Left* : Simultaneous power-law fit to the $XMM - Newton$ MOS1, MOS2 and PN data.(Γ =1.75±0.01, χ^2/dof = 764/598). The data have been plotted with a signal-to-noise ratio of 10. *Right* : Power-law fit to the RGS data (Γ=1.61±0.12, χ^2/dof = 65/129). The Galactic column is fixed at N_H=5.72×10^{20}cm^{-2} for both spectral fits.

The MOS and PN spectra were grouped to a minimum of 35 and 70 counts per bin respectively, and fitted over an energy range of 0.3−10.0 keV.

Initially I fitted the MOS1, MOS2 and PN spectra individually with a power-law and neutral absorption. This gives a photon index of $\Gamma = 1.66\pm0.03$ and $N_H = 4.50^{+1.29}_{-1.25} \times 10^{20}$ cm^{-2} for the MOS1 spectrum (χ^2/dof = 175/156), $\Gamma = 1.69\pm0.03$

and $N_H = 4.43^{+1.29}_{-1.08} \times 10^{20}$ cm^{-2} for the MOS2 spectrum ($\chi^2/dof = 199/157$) and $\Gamma = 1.76 \pm 0.03$ and $N_H = 5.53^{+0.53}_{-0.47} \times 10^{20}$ cm^{-2} for the PN spectrum ($\chi^2/dof = 367/281$). The fitted absorption column density is consistent with that expected from the Galactic ISM along the line of sight to III Zw2 ($N_H = 5.72 \times 10^{20}$ cm^{-2}). To investigate the presence of absorption over and above the Galactic column I added another neutral column in the rest frame of the source. This did not significantly improve the fit. I find upper limits on the absorption intrinsic in III Zw2 of $N_H < 2.30 \times 10^{20}$ cm^{-2}, $N_H < 3.54 \times 10^{20}$cm^{-2} and $N_H < 1.04 \times 10^{20}$ at 90% confidence level for MOS1, MOS2 and PN respectively. Addition of a blackbody soft excess component to the power-law model makes no improvement to the fit in either the MOS or PN spectra.

Residuals with respect to the power-law fit show an excess between 5.5−7.5 keV in both MOS and PN spectra, probably due to the presence of an Fe K_α line. To account for these residuals I added a single Gaussian to the underlying power-law keeping the absorption fixed to the Galactic value. This yields a broad line with the energy centered at E = 6.67 ±0.40 keV in MOS1 (σ = 1.10 ±0.30 keV, χ^2/dof = 163/154), at E = 6.82 ±0.29 keV in MOS2 ($\sigma = 1.20 \pm 0.35$ keV, $\chi^2/dof = 176/155$) and at E = 6.24 ±0.25 keV in PN (σ = 1.37 ±0.29 keV, $\chi^2/dof = 314/279$)

To better constrain the fit I fitted the same model to the MOS and the PN spectra simultaneously. Hereafter, the neutral absorption was fixed at the Galactic value of $N_H = 5.72 \times 10^{20}$ cm^{-2} for all spectral fitting. The simultaneous power-law fit gives a photon index of $\Gamma = 1.75 \pm 0.01$ ($\chi^2/dof = 764/598$). Residuals with respect to the power-law fit again show a broad feature between 5.5−7.5 keV (Fig. 3.1). Addition of a single broad Gaussian to the underlying power-law yields a line at E = 6.44 ± 0.35 keV ($\sigma = 1.25 \pm 0.35$ keV, EW = $1.25^{+0.31}_{-0.35}$ keV) and makes a significant improvement to the fit ($> 4\sigma$) with χ^2/dof = 680/595 ($\Delta\chi^2$ = 84 for 3 extra parameters). The upper limit on a O VIII line is EW < 100 eV and on a narrow line at 6.4 keV is EW < 48 eV.

One model for the broad line emission at around 6.4 keV is fluorescence Fe K_α

originating in an accretion disk around a central black hole. I thus fitted the excess between 5.5−7.5 keV, with a "Diskline" model (Fabian et al. 1989), for line emission from an accretion disk around a Schwarzschild black hole. Adding this component (with fixed $R_{in} = 6R_s$ and $R_{out} = 1000R_s$) to the underlying power-law with line energy, inclination and emissivity free to vary, yields a line at E= $5.95\ ^{+0.45}_{-0.14}$ keV (EW = $0.96^{+0.24}_{-0.18}$ keV) for a high inclination of $88°^{+2}_{-15}$ and emissivity (q) = -3.07 ± 0.35 (where emissivity varies as R^q). The goodness of fit (χ^2/dof = 685/594, $\Delta\chi^2$ =79 for 4 extra parameters) is comparable to the broad Gaussian model. The best fit inclination of $\approx 90°$ conflicts, however with the observation of superluminal motion in the source, which implies an inclination in the range of 0°−40° for the radio jet (Brunthaler et al. 2000). With the inclination restricted to $\leq 40°$ the diskline model yields a line at $7.63^{+0.63}_{-0.58}$ keV (EW = $0.81^{+0.07}_{-0.20}$ keV) with $q = -5.54 \pm 1.44$, inclination = $25°^{+8.0}_{-7.6}$ and the overall fit statistic of χ^2/dof = 694/594.

I also fitted the excess between 5.5-7.5 keV, with a "Laor" model (Laor 1991), for line emission from an accretion disk around a rotating black hole. A power-law and Laor line model (inclination $\leq 40°$ and emissivity free to vary), yields a line at $8.60^{+1.00}_{-0.70}$ keV (EW = $1.46^{+0.87}_{-0.80}$ keV) with $q = 3.77 \pm 0.36$, inclination = $21°^{+19}_{-21}$ and the overall fit statistic of χ^2/dof = 689/593.

I checked for the presence of an iron edge at E > 7 keV. Addition of an edge to the underlying power-law with the energy of the edge constrained between 7 and 9 keV, makes no improvement to the fit ($\Delta\chi^2 = 0$). A model consisting of a power-law plus a reflection component ($i \leq 40°$) from either neutral (PEXRAV model; Magdziarz & Zdziarski 1995) or ionized matter (PEXRIV model) is a significantly better fit than only a power-law model ($\Delta\chi^2$ = 60 and $\Delta\chi^2$ = 71 for neutral and ionised matter respectively for 3 extra parameters). The reflection component is strong with R = $1.82^{+0.87}_{-0.70}$, where R = $\Omega/2\pi$.

Adding a Gaussian to the PEXRAV and PEXRIV models yields a broad line at 6.45±0.35 keV (σ = 1.24 ±0.60 keV, EW = $0.87^{+0.73}_{-0.47}$ keV, $\Delta\chi^2$ = 27 for 3 extra parameters) and 6.49 ±0.44 keV (σ = 1.22 ±0.74 keV, EW = $0.88^{+0.52}_{-0.38}$ keV, $\Delta\chi^2$

= 17 for 3 extra parameters) respectively. Addition of a Gaussian improves the goodness of the fit at greater than 99.99% confidence level for both neutral and ionised reflection. Replacing the Gaussian in the above model with a diskline (with inclination restricted to $\leq 40°$) yields a line at 7.84±0.40 keV and 7.94±0.90 keV for the PEXRAV PEXRIV models respectively.

Apart from the Fe emission the EPIC spectra are apparently featureless. The higher resolution RGS spectrum can be described by a power-law of $\Gamma = 1.61 \pm 0.12$ with neutral absorption corresponding to the Galactic column ($\chi^2/dof = 65/129$), which is consistent with the EPIC spectra. Although the χ^2 value is very low due to the relatively low signal to noise of the spectrum, the largest residual (2σ) is seen at 22.08±0.015 Å in the rest frame of the source which is consistent with forbidden [O VII] line emission.

Archival Spectra

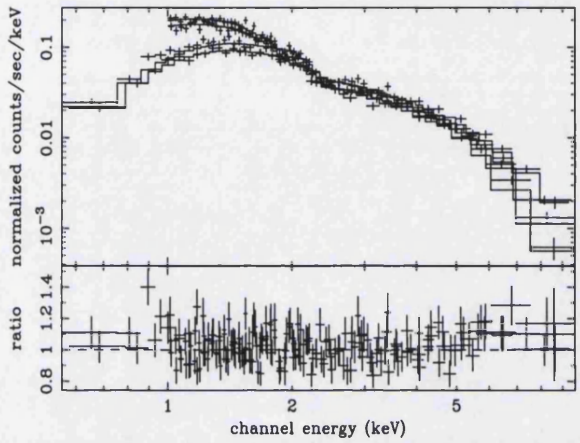

Figure 3.2: Simultaneous power-law fit to the SIS and GIS data (Γ =1.72±0.02, χ^2/dof = 620/599). The data are plotted with a signal-to-noise ratio of 10. The Galactic column is fixed at N_H=5.72×10^{20}cm^{-2}).

The *ASCA* GIS and SIS data were grouped to give a minimum of 35 counts per bin. SIS data below 1.0 keV were ignored due to decrease in efficiency below that energy for observations after 1994, which is not corrected for by the current software for generating response matrices. A power-law fit to all the data (energy range of 0.7−10.0 keV for GIS and 1.0−10.0 keV for SIS) gives a photon index Γ = 1.72±0.02 (χ^2/dof = 620/599) consistent with the $XMM-Newton$ observation (Fig. 3.2). Addition of a broad Gaussian to the underlying power-law yields a line at E = 6.72±0.26 (σ = 0.83±0.33 keV, $\Delta\chi^2$=16 for 3 extra parameters) making a $> 3\sigma$ improvement over the power-law fit (χ^2/dof = 604/596). The line has an equivalent width of EW = $0.43^{+7.6}_{-0.24}$ keV and a velocity width FWHM = 87,000±34000 km s^{-1}. Just as in the $XMM-Newton$ observation, there is no evidence of intrinsic absorption or of an excess at the soft X-ray end of the spectrum.

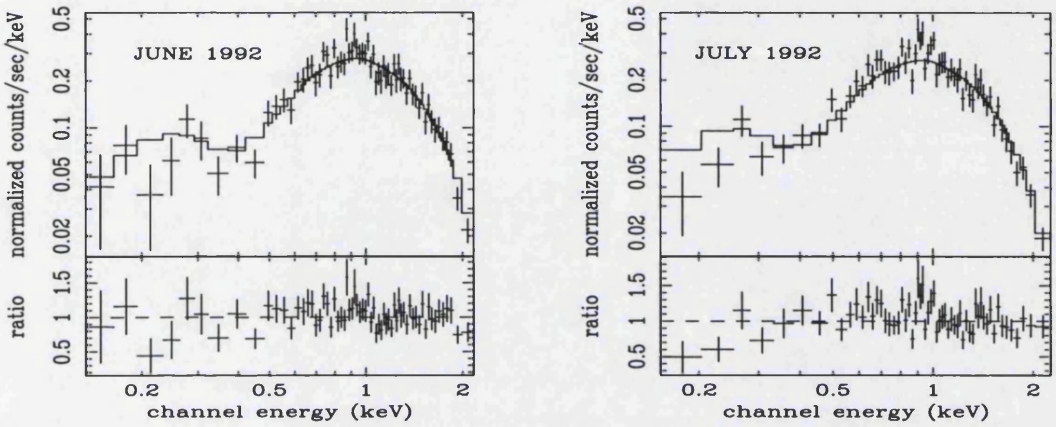

Figure 3.3: *Left* : Power-law fit to the *ROSAT* June spectrum ($\Gamma = 1.52 \pm 0.06$, $\chi^2/dof = 70/63$). *Right* : Power-law fit to the *ROSAT* July spectrum ($\Gamma = 1.61 \pm 0.08$, $\chi^2/dof = 79/58$). The Galactic column is fixed at $N_H = 5.72 \times 10^{20} cm^{-2}$).

Spectra from the 1992 *ROSAT* PSPC observations were grouped to give a minimum of 35 counts per bin. Both spectra are essentially featureless (Fig. 3.3) and can be described by a power-law and a Galactic column similar to the previous observations. Spectral fitting in the energy range of 0.1−2.0 keV results in a photon index $\Gamma = 1.52 \pm 0.06$ for the June spectrum ($\chi^2/dof = 70/63$) and $\Gamma = 1.61 \pm 0.08$ for the July spectrum ($\chi^2/dof = 79/58$). There is no significant intrinsic absorption over and above the Galactic column or an excess at softer energies, consistent with results from the *ASCA* and *XMM − Newton* observations.

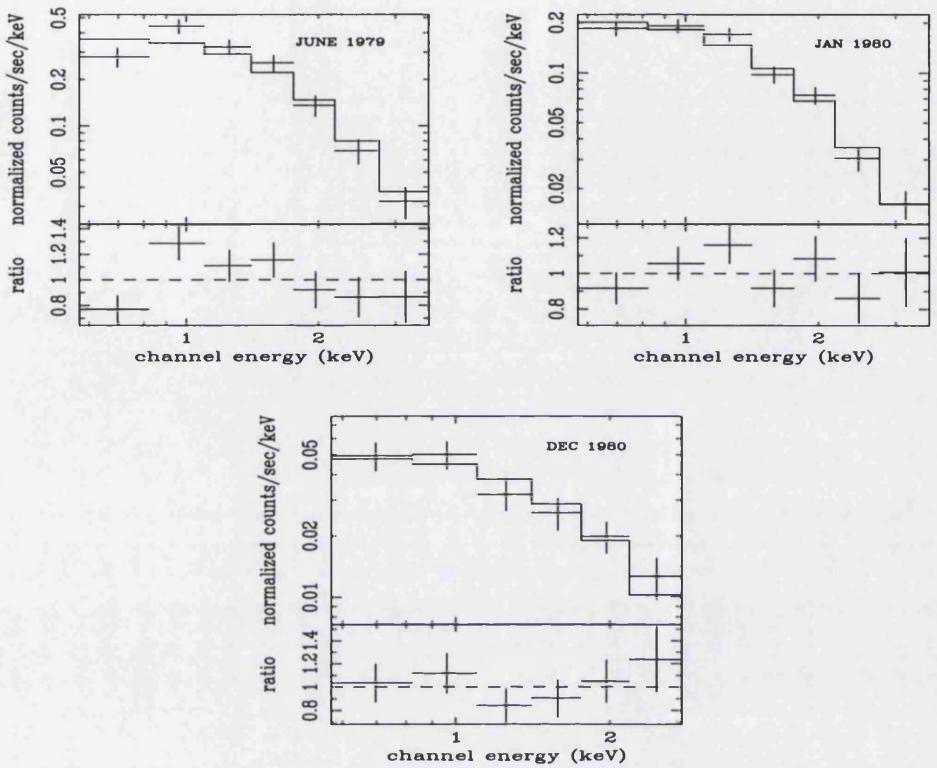

Figure 3.4: *Einstein* IPC spectra: 1979 June ($\Gamma = 2.06\pm0.30$, $\chi^2/dof = 13/5$), 1980 January ($\Gamma = 2.26\pm0.27$, $\chi^2/dof = 6/6$), 1980 December ($\Gamma = 1.91\pm0.40$, $\chi^2/dof = 4/5$).

Spectra obtained from the *Einstein* IPC were grouped to a minimum of 20 counts per bin and fit in the energy range of 0.4–4.0 keV. The 1980 December spectrum can be well described by a single power-law of $\Gamma = 1.91 \pm0.40$ ($\chi^2/dof = 4/5$). A power-law fit to the 1980 January and 1979 June spectra gives a photon index $\Gamma = 2.26\pm0.27$ ($\chi^2/dof = 6/6$) and $\Gamma = 2.06\pm0.30$ ($\chi^2/dof = 13/5$) respectively. We caution that there are large uncertainties in the IPC response matrices and the data are of low signal to noise.

		Powerlaw		Line				
Date	Model	Γ	norm	Energy (keV)	σ (keV)	EW (keV)	Incl	χ^2/dof
XMM-NEWTON (MOS1 + MOS2 + PN)								
2000 Jul 4	PL	1.75±0.01	1.67e-3±0.34e-4	-	-	-	-	764/598
	PL+GAU	1.79±0.01	1.67e-3±0.34e-4	6.44±0.35	1.25±0.35	$1.25^{+0.31}_{-0.35}$	-	680/595
	PL+Diskline[a]	1.79±0.01	1.67e-3±0.34e-4	$5.95^{+0.45}_{-0.14}$	-	$0.96^{+0.24}_{-0.18}$	$88°^{+2}_{-15}$	685/594
	PL+Diskline[b]	1.77±0.01	1.67e-3±0.34e-4	$7.63^{+0.63}_{-0.58}$	-	$0.82^{+0.07}_{-0.20}$	$25°^{+8.0}_{-7.6}$	694/594
	Pexrav+Gau[b]	1.79±0.01	1.66e-3±0.34e-4	6.45±0.35	1.40±0.60	$0.87^{+0.73}_{-0.47}$	$10°^{+8}_{-2}$	677/593
	Pexriv+Gau[b]	1.79±0.01	1.66e-3±0.34e-4	6.49±0.44	1.22±0.74	$0.88^{+0.52}_{-0.38}$	$9°^{+12}_{-4}$	677/592
ASCA (GIS2 + GIS3 + SIS0 + SIS1)								
1997 Jul 01	PL	1.72±0.02	2.71e-3±0.74e-4	-	-	-	-	620/599
	PL+GAU	1.75±0.02	2.75e-3±0.79e-4	6.72±0.26	0.83±0.33	$0.40^{+7.60}_{-0.24}$	-	604/596
ROSAT (PSPC)								
1992 Jul 18	PL	1.61±0.08	1.54e-3±0.56e-4	-	-	-	-	79/58
1992 Jun 12	PL	1.52±0.06	1.59e-3±0.56e-4	-	-	-	-	70/63
Einstein (IPC)								
1979 Jun 21	PL	2.06±0.30	6.07e-3±0.43e-3	-	-	-	-	13/5
1980 Jan 09	PL	2.26±0.27	3.18e-3±0.19e-3	-	-	-	-	6/6
1980 Dec 19	PL	1.91±0.40	7.56e-4±1.1e-4	-	-	-	-	4/5

Notes: [a] Disk inclination free to vary.
[b] Disk inclination constrained between 0°−40°.

Table 3.2: Model fit parameters for the X-ray spectra of III Zw2 taken by different observatories over the last 20 years. The Galactic column is fixed at $N_H = 5.72 \times 10^{20}$ cm^{-2} for all spectral fits.

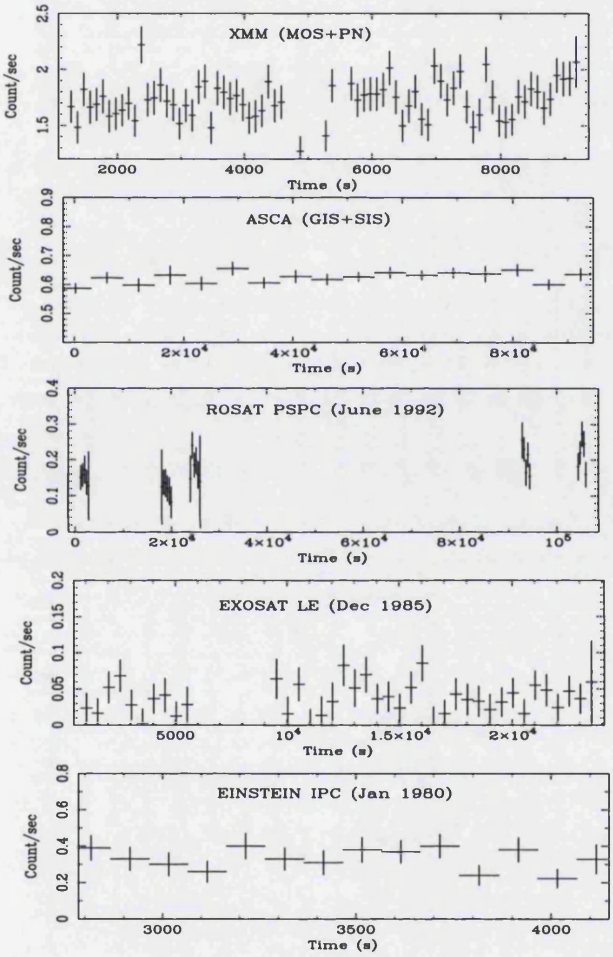

Figure 3.5: Typical light curves of III Zw2 from different observatories.

Mission	Date	Bintime sec	χ^2/dof	Prob of constancy
XMM-MOS	2000 Jul 04	100	27/29	0.54
ASCA	1997 Jul 01	5760	15/16	0.52
ROSAT	1994 Dec 26	400	2/6	0.87
	1994 Jun 16	400	4/3	0.29
	1992 Jul 18	400	6/18	0.99
	1992 Jun 12	400	25/26	0.48
EXOSAT	1985 Dec 20	100	170/187	0.98
	1985 Nov 30	100	174/215	0.98
	1985 Aug 18	100	76/85	0.74
	1983 Dec 18	100	40/48	0.80
EINSTEIN	1980 Jan 09	100	4/12	0.98
	1980 Dec 19	100	27/36	0.85
	1979 Jun 21	100	6/8	0.64

Table 3.3: Results of the statistical test to determine the constancy of light curves for the different missions. There is no significant variation in X-ray flux of III Zw2 during any of the observations.

3.2.3 X-ray variability

Light curves from observations between 1975−2000 were compiled to study short term variability of the source. No significant flux variations are observed during any of the observations. Fig. 3.5 shows typical light curves from different observatories. I performed statistical analysis for each time series to determine the constant source probability associated with the χ^2 value. Results of the analysis are listed in Table. 4.2 and confirm the absence of significant X-ray variability in any of the observations which probed time-scales between 100−45,000 s.

To study long term X-ray behavior of the source I determined the 1−2 keV flux for each observation. Model flux for data with spectral information was obtained directly from spectral fits. For other observations broad band count rates were converted to equivalent flux in the 1−2 keV band using the PIMMS flux converter, assuming a power-law spectral model. As the spectral photon indices and neutral absorption are similar in the *XMM* observation and in previous X-ray observations (e.g. Hall et al. 1981; Petre et al. 1984), I have used the power-law index Γ = 1.7 (deduced from the XMM-EPIC data) and $N_H = 5.72\times10^{20}cm^{-2}$ for conversion. The 1−2 keV flux for SAS-3 was determined (assuming a power-law spectral model) using the 1-10 keV flux and the best fit photon index Γ = 1.3 from Schnopper et al. 1978. Fig. 3.6 shows the 1-2 keV flux variations in III Zw2. The light curve shows 10-fold flux variations, over time-scales of years.

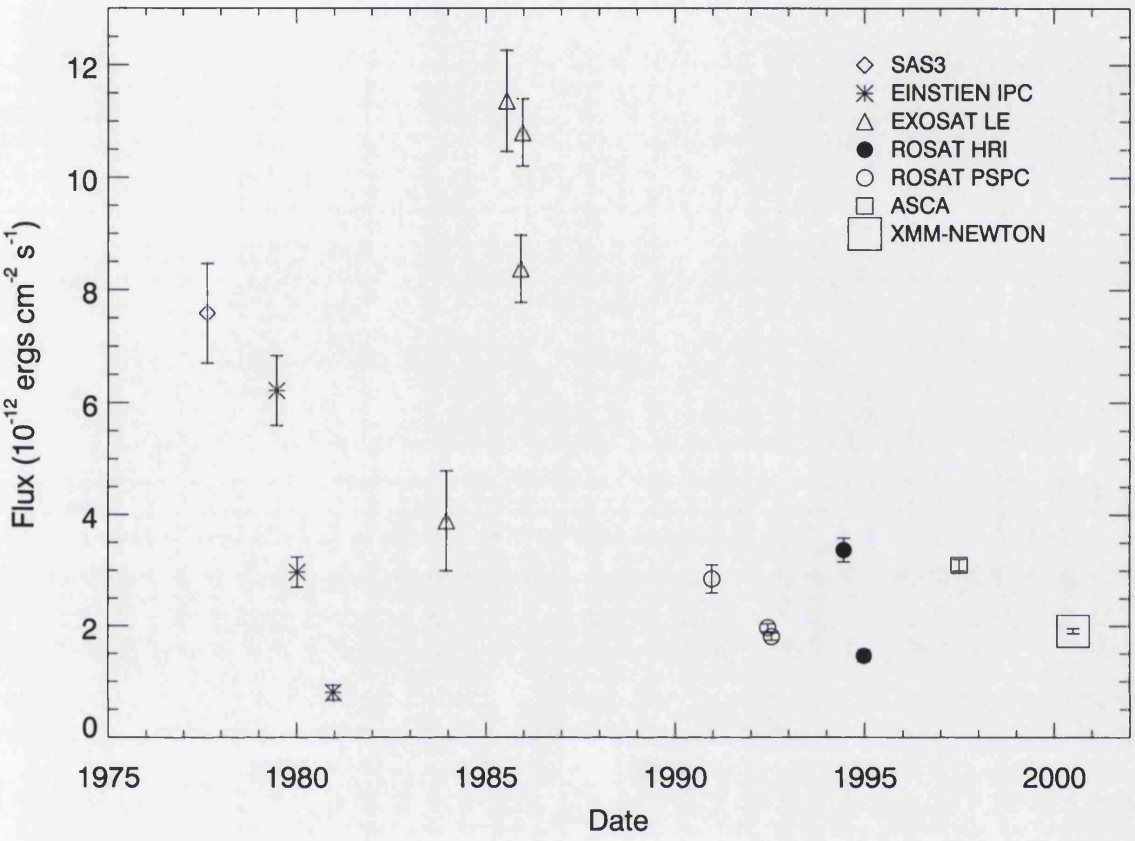

Figure 3.6: X-ray (1-2 keV) light curve of III Zw2 from 1975 to 2000. Model flux for data with spectral information was obtained directly from spectral fits (*XMM*, *ASCA*, *Rosat*(1992) and *Einstein*). For other observations, broad band count-rates were converted to equivalent flux in the 1-2 keV band using the PIMMS converter (assuming a power-law model with a photon index Γ =1.7, N_H=5.72×10^{20} cm $^{-2}$). The *SAS*-3 flux was determined via PIMMS (assuming a power-law spectral model) using the 1-10 keV flux and the best fit photon index Γ = 1.3 from Schnopper et al. 1978.

3.3 Multi-wavelength emission

All available data at UV, optical, infrared and radio wavelengths, from 1975 to 2000 were obtained from archives, literature and other sources. These data were combined along with the X-ray data to study the long term behavior of the source over a broad spectral range.

3.3.1 Multi-wavelength data

Ultraviolet data are from the *IUE* archives (see also Chapman et al. 1985). Optical B band data from 1975 to 1991 are a combination of photometry from different photographic monitoring experiments. Data from 1975 to mid 1977 were taken from Lloyd (1984) and data from mid 1977 to 1991 are from Clements et al (1995). The CCD photometry data for 1989, 1992 and 1998 were obtained from the LaPalma ING (Issaac Newton group of telescopes) archives.

The infrared data of Oct 2000 are from the SAAO and the rest are compiled from various publications listed below: Dec 1975 and Jan 1978 (Rieke et al 1978), Sept 1985 (Elvis et al 1994), Jul 1977 (Neugebauer et al 1978), June 1978 (Condon et al 1981), Aug 1979 McAlary et al. 1983), Nov 1977 (Hyland et al. 1982), Jun 1983 (Edelson et al. 1987), (Lebofsky & Rieke. 1980) and Oct 1988, Sept 1989 (Kotilainen et al. 1992). The May/Jun 1998 millimeter data were obtained from the JCMT archives and the rest from Landau et al (1980). The radio data at 22 GHz and 37 GHz are from Metsähovi (see Teräsranta et al. 1998) and at 14.5 GHz and 8 GHz are from Michigan (Brunthaler et al. 2000).

Data reduction

Optical images from the INT (Isaac Newton telescope, 2.5 m) and the JKT (Jacobus Kapteyn Telescope, 1.0 m) of the ING archives were used to obtain magnitudes for III Zw2 via differential photometry. The optical data was reduced using the *IRAF* software package. The electronic bias level was subtracted and blank strips removed

from each frame by applying the overscan and trim corrections respectively. The images in various filters were processed using the combined bias and flat frames using the procedure *ccdproc*.

The instrumental magnitudes were extracted from the processed images via aperture photometry using the GAIA software. UBVRI zero points were determined using the standard stars LA97284 (JKT) and 95Z96 (INT). For those images not accompanied by standard star observations, magnitudes for III Zw2 were obtained via differential photometry using the calibrated magnitudes of other stars in the III Zw2 field (see Appendix A). The UBVRI magnitudes for III Zw2 were corrected for extinction using the airmass and atmospheric extinction measured at LaPalma for the individual days. B magnitudes were converted to flux using the relation $f = 4.39\times10^{6}(10^{-0.4M})$ mJy (Clements et al. 1995). Additional 10% errors were included to account for the systematic differences between the photographic and CCD measurements.

J, H and K photometric observations were made with the MkII Infrared Photometer on the 1.9-m telescope at the SAAO in Sutherland. These data were reduced by E. Romero-Colmenero to the current standard SAAO photometric system (Carter 1990) using standard SAAO IR photometry reduction software. Each observation was then corrected to a nearby standard from the Carter (1990) list.

Data from the JCMT (James Clerk Maxwell Telescope) archives were taken with the Submillimetre Common user Bolometer Array (SCUBA; Holland et al. 1999). SCUBA was used in photometry mode to make observations at 2000 μm, 1350 μm and 850 μm. These observations were retrieved from the JCMT archive and reduced in the standard manner by J. Stevens. At 850μm the off-source bolometers were used to remove correlated sky noise from the source signal. Flux calibration was made with respect to either Uranus or the JCMT secondary calibrator CRL2688.

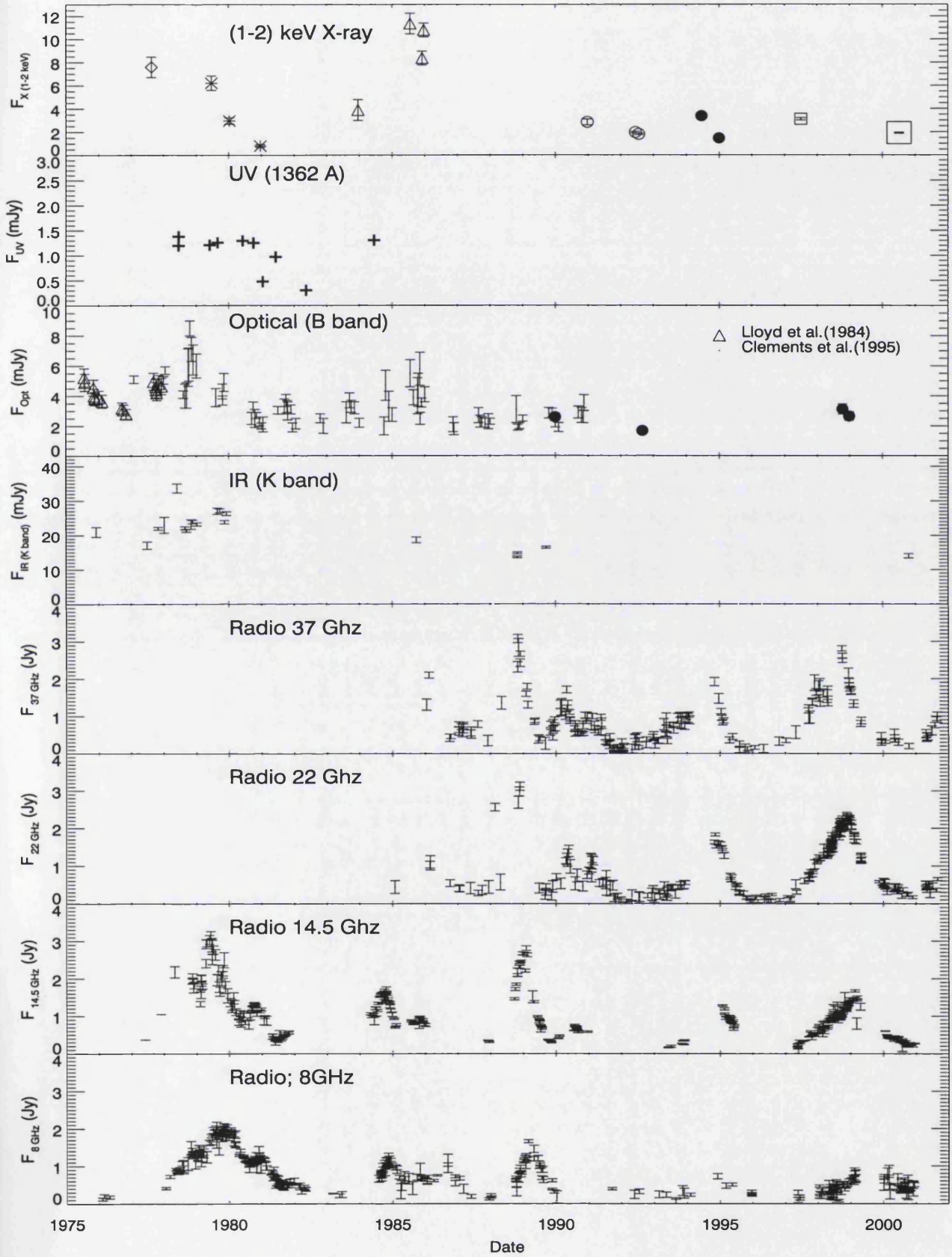

Figure 3.7: Multi-wavelength light curves of III Zw2 showing flux variations, with increasing wavelengths from top to bottom. (See §3 for the sources of data.)

3.3.2 Multi-wavelength emission

Variability

Multi-wavelength emission from X-rays to radio for III Zw2 over a period of 25 years from 1975 - 2000 is presented in Fig. 3.7. The radio and optical (up to 1990) wavelengths are better sampled than the other bands. The source shows 10- and 20-fold variations in the X-rays and radio respectively. The amplitude of variations is somewhat smaller in the optical (4-fold) and IR (2-fold). Visual inspection of the multi-band light curves shows related behaviour from X-rays to the radio. The X-rays and the optical appear to be coincident in time but the radio flux is seen to peak later (a lag of about 13 months between the optical and 8-GHz emission has been reported by Clements et al. 1995).

Wavelengths	coefficient(r)	probability
X-ray/Opt	0.86	0.00072
UV/Opt	0.78	0.008
IR/Opt	0.75	0.03

Table 3.4: The table gives the Pearson linear correlation coefficient and probability, that there is no linear correlation between the light curves at these wavelengths.

I performed a Pearson linear correlation test to determine correlation, if any between X-ray, UV, optical and IR emission. Except for the optical the other wavelengths are not very well sampled and hence I used a simple approach. The optical light curve was interpolated and was used to determine the optical flux corresponding to the individual X-ray, UV and IR flux points. The Pearson linear correlation coefficient for different wavelengths are listed in Table 3.4. The X-rays are found to be significantly ($> 3\sigma$) correlated with the optical (Fig 3.8). The correlation of light

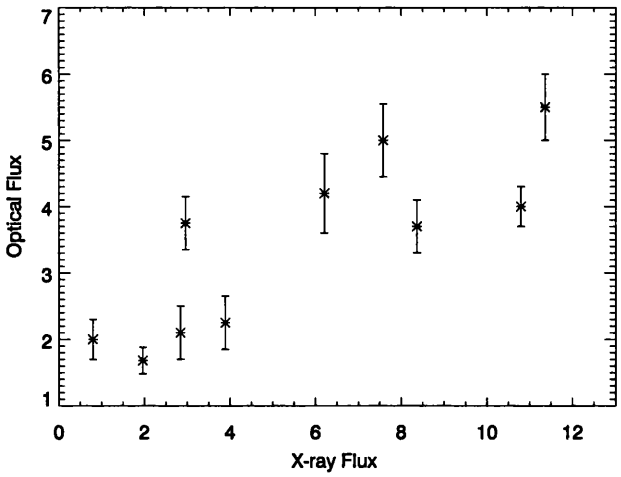

Figure 3.8: Correlation between the X-ray and the optical emission in III Zw2. The Pearson linear correlation coefficient is 0.86 and the correlation significance is 0.00072

curves at the UV and IR wavelengths is less significant ($> 2\sigma$).

Spectral energy distribution

Fig. 4.9 shows the total spectral energy distribution of III Zw2, incorporating data from 1975 to 2001. The lack of spread in data in the frequency range 10^{11}-10^{14} Hz is probably due to fewer observations in that region. The spectrum peaks at the optical/IR wavelengths, with no evidence for an excess in UV and soft X-rays. The overall spectral energy distribution shows a power-law over a broad frequency range (10^{11}-10^{14} Hz). A change in power-law gradient (hardening) is observed below 10^{11} Hz. The SED would have to be steeper between 10^{15}-10^{16} Hz, than at lower frequencies in order for the UV to connect with the X-rays. Above 10^{16} Hz the spectrum becomes hard again.

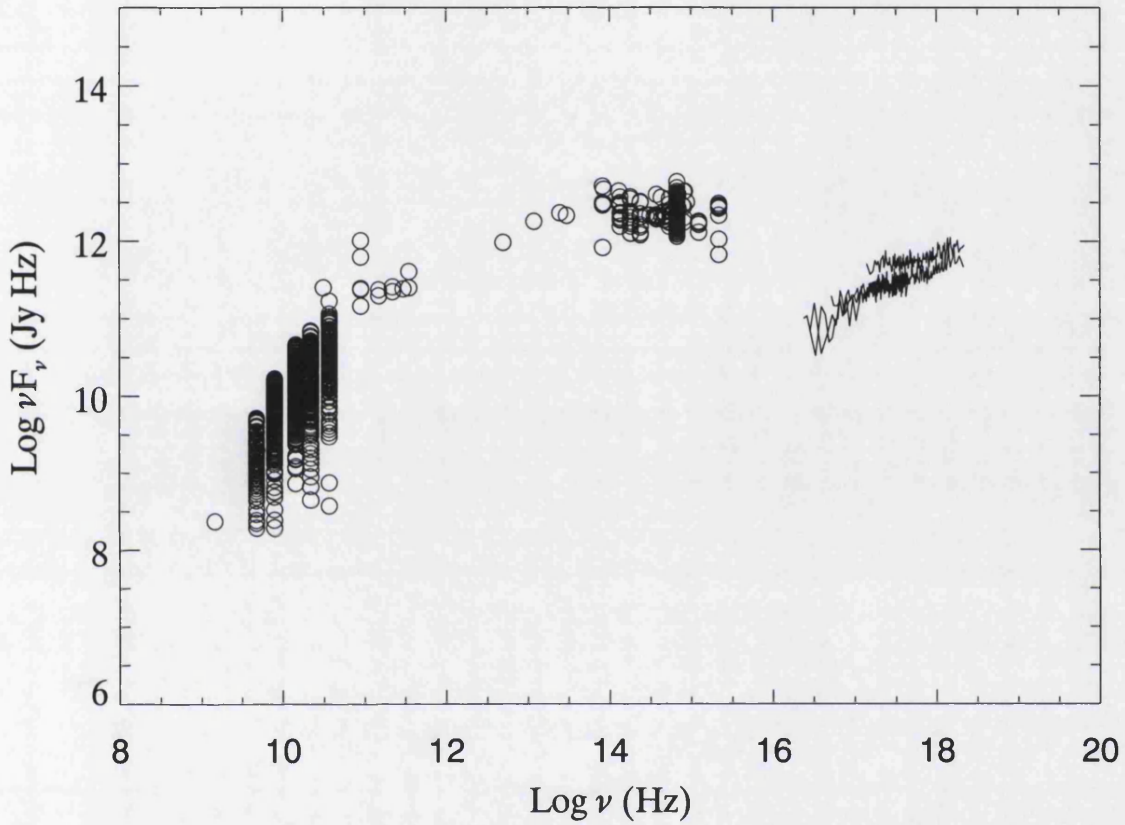

Figure 3.9: Spectral energy distribution for III Zw2. It includes radio to X-ray data taken over the last three decades. The overall spectral energy distribution is a power-law over a broad frequency range (10^{11}-10^{14} Hz). A change in power-law gradient (hardening) is observed below 10^{11} Hz. The SED would have to be steeper between 10^{15}-10^{16} Hz, than at lower frequencies in order for the UV to connect with the X-rays. Above 10^{16} Hz the spectrum becomes hard again

3.4 Discussion

3.4.1 X-ray emission

Study of the *XMM−Newton*, *ASCA* and *ROSAT* X-ray spectra reveals that there is relatively little change in the power-law photon index ($\Gamma \approx 1.6-1.8$) between 1992−2000. Spectra obtained from the *Einstein* IPC (with the exception of 1980 Jan) and previous missions like the *Ariel* VI (Hall et al. 1981) and *SAS*-3 can also be described, within errors by $\Gamma \approx 1.6-1.8$.

A power-law slope of $\Gamma \approx 1.7$ is typical of Seyfert 1 galaxies (Reynolds 1997, Turner & Pounds 1989). Current models for production of the X-ray continuum explain these spectroscopic observations by the presence of a hot electron or electron-positron cloud which Compton up-scatters thermal soft photons from the accretion disk to generate the hard X-ray power-law (e.g. Haardt et al. 1994). A power-law slope of $\Gamma \approx 1.7$ (at radio wavelengths) is also typically observed for synchrotron radiation in many radio sources (Kukula et al. 1998, Bloom et al. 1998). III Zw2 is a strong radio source with relativistic jets and therefore it is also possible that synchrotron or synchrotron self Compton makes a significant contribution to the X-ray continuum. Thus, on its own the power-law slope does not allow us to distinguish between the possible origins for the X-ray continuum.

A soft X-ray excess is common amongst quasars (Wilkes et al. 1990, Masnou et al. 1992, Saxton et al. 1993) and Seyfert I galaxies (Piro, Matt & Ricci 1997, Fabian et al. 1986) and is observed in both radio-loud (e.g. 3C 273) and radio-quiet (e.g. E1821 +643) sources (Warwick et al. 1989; Turner et al. 1990). Almost half of the 48 Seyfert-type AGN surveyed by Turner and Pounds (1989) showed evidence for a soft excess. This excess at soft X-ray energies is generally interpreted as optically thick thermal emission from inner regions of an accretion disk (Saxton et al. 1993). Although III Zw2 is extremely luminous $L_{X(2-10)} = 10^{44} - 10^{45}$ erg s^{-1}, study of spectra over a 25 year period do not reveal an excess at soft X-ray energies. One possible explanation for this absence could be that the soft excess

in III Zw2 contributes significantly only at energies below 0.2 keV. This suggests a lower disk temperature with a peak possibly in the UV region, but this is also not observed. Another possibility is that the soft excess is relatively weak compared to the power-law continuum emission, for example as could be the case if the power-law continuum has contributions from other sources (e.g. synchrotron or synchrotron self Compton emission from the jets) in addition to the Comptonised and reflected component.

We do not find significant evidence of absorption intrinsic to the source in the XMM-Newton or archival data studied here. This is in agreement with the findings of previous observations (Hall et al. 1981; Petre et al. 1984; Kaastra & de Korte 1988) and inferences from the IR/optical observations (Ward et al 1987; Carleton et al. 1987). We do however detect a strong reflection component ($R \approx 2$) in the XMM-Newton data, a period when the X-ray flux of III Zw2 was at minimum (Fig. 3.6 and Fig. 3.7). The RGS spectrum is almost featureless except for a weak emission feature consistent with the forbidden O [VII] emission line. Such an emission line is expected from a photo-ionised plasma at relatively low ($T_e < 10^5$ K) temperature and density ($n_e < 10^{10}$ cm^{-3}) (Porquet & Dubai 2000). There is no evidence of edge-like or saw-tooth spectral features which are seen in some Seyferts and are associated with relativistic disk lines or absorption edges from a warm absorber in our line of sight (Branduardi-Raymont et al. 2001, Lee et al. 2001).

The line emission between 6–7 keV in AGN is generally thought to be Fe K_α from neutral or ionised material. The line could arise from an accretion disk via the process of "reflection" due to the X-ray irradiation of dense, relatively cold ($T \leq 10^6$ K) gas in the vicinity of the central black hole (George & Fabian 1991, Matt et al. 1991) or from other neutral material, like the molecular torus (Mrk 205, Reeves et al. 2001). A study of *ASCA* Seyfert I iron lines (Nandra et al. 1997) shows that Fe profiles show a broadening primarily to the red, a core energy close to 6.4 keV and relatively little flux blue-ward of 6.4 keV. The 6.44 keV line in the *XMM* spectra has a velocity width of FWHM = 140,000±36000 km s^{-1}, implying relativistic velocities.

The large velocity width rules out emission from a distant torus. If we assume that the observed line width is due to Doppler broadening in a relativistic accretion disk, it would require the line emission to originate very close to the black hole, where relativistic velocities are expected (Nandra et al. 1997).

However, the accretion disk model fit (for inclination $\leq 40°$) to the observed line emission yields a line at 7.63 keV (diskline) 8.6 keV (Laor) which is substantially higher than the line center energies of Fe K_α emission (6.4−6.97 keV). The equivalent width of the line measured from the incident+reflected spectra (EW $\sim$ 800 eV) is also larger than the theoretical prediction of an intrinsic Fe line EW of 100−200 eV (Fabian et al. 1989). Disk models incorporating relativistic effects have been able to increase iron line EW to about 300 eV for low disk inclinations (Dabrowski et al 2000). Ballantyne et al. (2001) showed that the largest EWs measured from the incident+reflected spectra are $\sim$ 800 eV when the gas is ionised. The ionised disk model if correct, may explain the observed EW in III Zw2 but not the high line center energy, which would require significant blue shifting of the Fe K_α emission. This suggests that the existing disk models are unable to fully explain the excess emission between 5.5-7.5 keV seen in the spectrum of III Zw2.

In general, unlike III Zw2, luminous radio loud quasars tend to have weaker Fe line emission (Reeves et al. 2000). However, it should be noted that although III Zw2 is very luminous and exhibits large radio flares, it is not a typical radio-loud quasar, but is instead classed as a radio-intermediate quasar, i.e., a radio-weak quasar but with relativistic jets pointed straight at the observer (Falcke et al. 1999). One possibility for the observed line profile is contributions of iron line emission from the base of the milliparsec jet system of III Zw2, perhaps in addition to the disk emission. Of the 24 type I AGN studied by Reynolds (1997), velocity widths corresponding to FWHM $>$ 100,000 km s^{-1} and EW $\sim$ 1.0 keV have been observed in only two X-ray luminous ($L_{2-10} > 10^{44}$ erg s^{-1}) galaxies, 3C 120 and 3C 382, both radio loud sources exhibiting superluminal motion. Contribution of unresolved, Doppler shifted Fe emission from the base of relativistic jets and/or ejecta in addition

to disk emission could be one possible explanation for the large velocity width, EW and the high line energy of the observed emission between 5.5−7.5 keV. Doppler shifted iron line emission from the approaching and the receding relativistic jets has been observed in the Galactic jet source SS 433 (Herman et al. 2001).

3.4.2 X-ray Variability

Long term X-ray variability is a common phenomenon in AGN (Grandi et al. 1992) but rapid variability is typically not detected in high luminosity AGN (Green et al. 1993, Lawrence & Papadakis 1993). III Zw2 exhibits large amplitude (10-fold) X-ray variability over time-scales of years. However, I do not detect significant variations in X-ray flux over short time-scales (few 1000 s) in any of the data.

In order for variations in flux to be observed, the variability time-scales must be larger than the source light crossing time. As such, rapid variations allow us to place upper limits on the mass of the central black hole. Based on reports of a 1000-1500 s flare in III Zw2 (Pounds 1986) Kaastra et al. 1988 have estimated a black hole mass of $\sim 10^7$ $M_\odot$ for the source. I do not detect any swift changes in X-ray fiux (which supports the findings of Tagliaferri et al. 1988 where it was suggested that the flare detected in III Zw2 may be associated with the nearby star HD 560) and hence do not require such a low mass black hole to explain the X-ray variability in III Zw2.

Luminous sources like III Zw2 are expected to have larger X-ray emitting regions than lower luminosity Seyferts, possibly because they have more massive central black holes (Green et al. 1993, Saxton et al. 1993). I consider the high X-ray luminosity and the lack of short term variability hints at the presence of a large mass black hole ($\geq 10^9 M_\odot$) at the center of III Zw2. The absence of a blackbody component at low X-ray energies is consistent with this picture, as the disk around such a massive black hole would be formed further away and hence would have a lower temperature. I use the following mass relationship from Wandel et al. (1999)

to obtain an estimate of the black hole mass in III Zw2.

$$M_8 \approx 0.4\sqrt{\frac{L_{46}}{Un_{10}}} \times \nu_3^2 \tag{3.1}$$

where M_8 is the black hole mass in units of $10^8 M_\odot$, L_{46} is the bolometric luminosity in units of 10^{46} erg s^{-1}, ν_3 is the Hβ FWHM in 10^3 km s^{-1}, n_{10} is the density in units of 10^{10} cm^{-3} and U is the ionisation parameter.

The bolometric luminosity is obtained from the measured X-ray luminosity ($L_{2-10} = 2\times10^{44}$ erg s^{-1}) by including a bolometric correction factor of 20 ($L_{X-ray} = 0.05\ L_{bol}$; Elvis et al. 1994). Using the observed Hβ FWHM of III Zw2 (5200 kms^{-1}, Wilkes 1986) and assuming $(Un_{10}) = 1$, I obtain a black hole mass of $\sim 10^9 M_\odot$. The result is consistent with the lack of rapid variability in the source and is comparable with the mass estimate obtained from O III line widths by Wandel et al. (1986).

3.4.3 Multi-wavelength emission

AGN emit radiation across a wide frequency range, from X-rays to radio. The X-rays are thought to arise from regions very close to the central black hole. Leading models based on the observed power-law X-ray spectra in AGN explain the X-ray emission in terms of a hot Comptonising corona which up-scatters softer disk photons to produce the hard X-ray continuum. The optical and UV radiation is considered to be thermal emission from an accretion disk, with the optical arising from outer parts of the disk. The infrared is generally emission from hot dust but in some cases has a non-thermal origin. The radio emission is synchrotron radiation from relativistic jets. Since the emission in the different wave bands arises from different emission regions and due to different radiation processes, their time-scales of variations could be very different and as such we would not expect them to be closely related.

Rapid X-ray variability is generally found to be unrelated to the optical variations in AGN. However, on time-scales of several weeks or more, correlated X-ray and the optical temporal variations have been recently detected in NGC 7469 (Nandra et

al. 2000) and NGC 4051 (Peterson et al. 2000). Related X-ray and K-band emission has been observed in the radio loud AGN 3C 273 (McHardy et al. 1999). Although correlated radio and optical emission on long time-scales has been reported in a few AGN (Clements et al. 1995), broad band co-ordinated activity from the X-rays to the radio is rare.

The multi-wavelength emission of III Zw2 shows coordinated behaviour from X-rays to radio. The absence of a big blue bump in the broad-band spectrum contrasts with typical AGN in which a substantial proportion of UV/X-rays are thought to be emitted from an optically thick accretion disk (cf. Kaastra & de Korte 1988). The large amplitude flare observed in all wavelengths around 1980 suggests that the emission from the X-rays to radio could have a common origin. The radio emission in radio-loud AGN is thought to be synchrotron radiation. Optical micro-variability was recently detected in III Zw2 where the source flux increased by 0.1 Mag in about 4 hours (Jang & Miller 1997), which suggests a compact emission region. Jang & Miller (1997) have found that most AGN that exhibit micro-variability are radio-loud and have argued that micro-variability is associated with the jets in these sources. If this model is correct it would imply that at least *some* of the optical emission in III Zw2 is of non-thermal origin.

The spectral energy distribution (SED) of III Zw2 from the radio to the optical/UV mimics a typical synchrotron spectrum: self-absorbed at low energies (radio/millimeter), power-law over a broad wavelength range and a cut-off at high energies. It is unlikely that the turnover in optical/UV is caused by absorption as we do not find evidence of intrinsic absorption in the X-rays and the source exhibits minimum reddening compared to the other hard X-ray selected objects of the Piccinoti et al. (1982) sample (Carleton et al. 1987). One can explain the observed SED, optical micro-variability and the related behaviour at different wavelengths if the broad band emission from 10^9 - 10^{14} Hz is due to synchrotron radiation from an expanding magnetized cloud of relativistic electrons. If this is the case the synchrotron emission would be self-absorbed in the radio-millimeter region and would

have a high energy cut-off at frequencies greater than 10^{14} Hz.

The X-rays are not consistent with a synchrotron spectrum which would produce the radio and optical emission and hence have to be a separate component. However, the X-ray emission is found to be significantly correlated with the optical, which suggests a close link between the two wave-bands. The X-rays have a power-law shape typical of Compton up-scattered emission. If a hot Comptonising corona close to the disk was responsible for all the observed X-ray emission it would be difficult to explain its correlation with the synchrotron optical emission.

A simple explanation for the observed coincidence of X-ray flares with those in the other wavelengths would be that *some* of the X-ray emission is due to Compton up-scattering by the high energy relativistic electrons that give rise to synchrotron radio and optical/IR radiation. Electron Lorentz factors of $\gamma_e \sim 400$ have been measured in the radio band in III Zw2 (Falcke et al. 1999) which are sufficient to up-scatter IR/optical photons to X-ray energies. The strong reflection that we measure requires that a substantial fraction of the X-rays produced by this process, must also be reflected in addition to the X-rays produced by Compton up-scattering in the corona. Since the jets in III Zw2 are quite small (sub parsec order), it is not unreasonable to expect this kind of reflection.

I have modeled the observed radio to optical spectrum (of July 1997) as synchrotron radiation from a plasma with a power-law energy distribution $n(\gamma)\mathrm{d}(\gamma) = \mathrm{n}_{\gamma_0}\gamma^{-s}\mathrm{d}\gamma$ (for electron Lorentz factors $\gamma_L < \gamma < \gamma_H$). The electron pitch angle distribution is assumed to be isotropic (Lobanov 1998).

$$F_\nu^S \propto \left(\frac{\nu}{\nu_m}\right)^{\alpha_t} \left\{1 - exp\left[-\left(\frac{\nu}{\nu_m}\right)^{-(\alpha_t+\alpha_o)}\right]\right\} \left\{exp\left(-\frac{\nu}{\nu_H}\right)\right\} \qquad (3.2)$$

where ν_m is the turnover frequency at which the source becomes opaque to synchrotron self-absorption (frequency at which the optical depth $\tau_s \approx 1$), α_t, α_o are the spectral indices of the optically thick and optically thin parts of the spectrum

(spectral index defined as $F_\nu^S \propto \nu^{-\alpha}$) and ν_H is the upper cutoff frequency in the synchrotron spectrum.

The X-rays are modeled as Compton up-scattered synchrotron radiation (Bloom and Marscher. 1996).

$$F_\nu^{IC} \propto N_0 R F_\nu^S ln\left(\frac{\nu_H}{\nu_m}\right) \tag{3.3}$$

$$R = \frac{\theta D}{2}(1+z)^{-2} \tag{3.4}$$

$$N_0 = n(\alpha) D_{Gpc}^{-1} \theta^{-(4\alpha+7)} \nu_m^{-(4\alpha+5)} F_m^{(2\alpha+3)} (1+z)^{2(\alpha+3)} \delta^{-2(\alpha+2)} \tag{3.5}$$

where, α is the spectral index for the optically thin radiation (defined as $F_\nu^S \propto \nu^{-\alpha}$), θ is the angular diameter measured in milliarcseconds, F_m is the flux at frequency ν_m in Jy, z is the red-shift of the source and n(α) is function tabulated by Marscher (1987).

The above formulae were incorporated into a numerical code, which was used to generate the synchrotron and Inverse Compton spectrum for III Zw2. I use a source size of 0.07 *mas* and $\alpha_{thin} = 0.7$ measured at 43 GHz during the 1997-1999 flare (Falcke et al. 1999, Brunthaler et al. 2000). I assume no relativistic beaming i.e. δ=1. Fig 3.10 shows a model fit to the 1997 July spectrum. The observed radio to optical emission is well described by a synchrotron spectrum with peak frequency of 37 GHz and a high energy cut-off at 3×10^{14} Hz. The best fit spectral index for the optically thick region of the synchrotron spectrum is $\alpha_{thick} = 1.3$ which is indicative of an inhomogeneous source (Bloom et al. 1999).

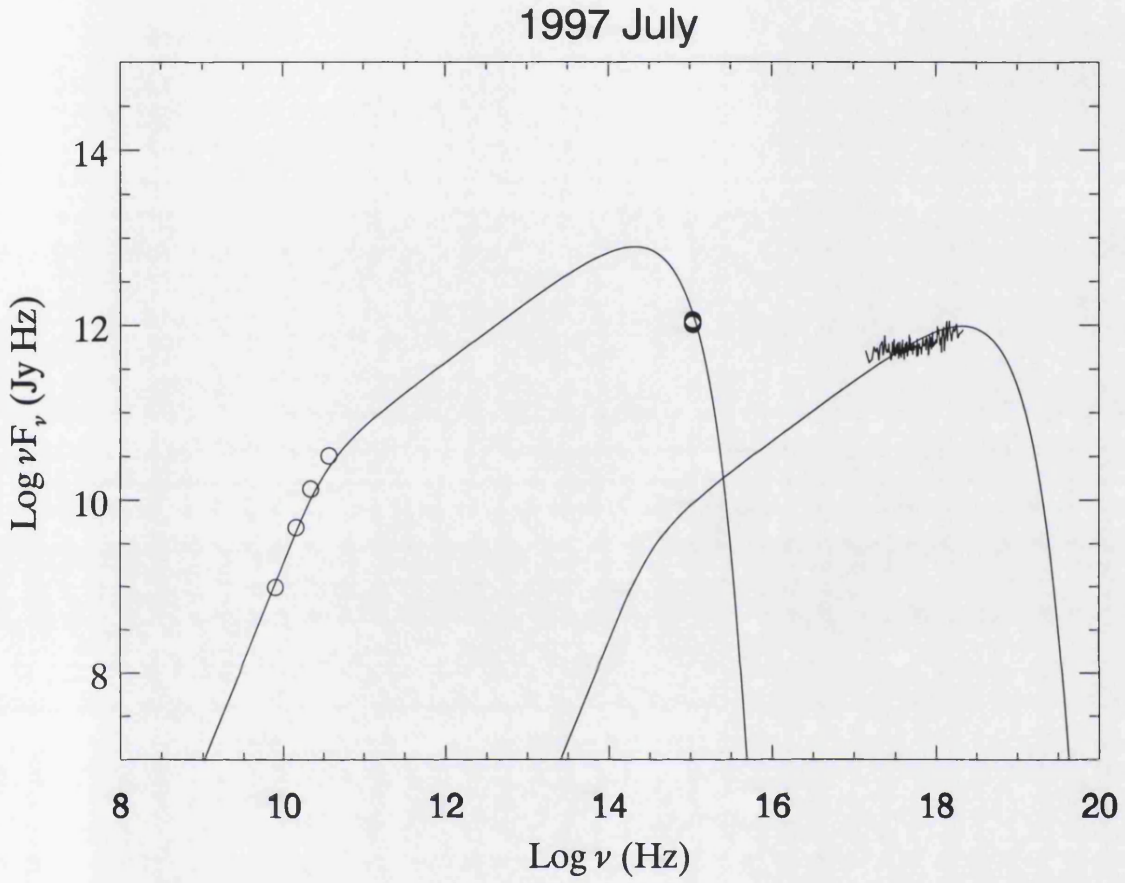

Figure 3.10: Radio to optical spectrum modeled as synchrotron radiation with peak frequency of 37 GHz, a high energy cut-off at 3×10^{14} Hz, α_{thin} = 0.7 and α_{thick} =1.3 (where $F_\nu^S \propto \nu^{-\alpha}$). The X-rays are modeled as Compton up-scattered synchrotron radiation for a source size of 0.07 *mas* and δ=1

3.5 Conclusion

I have studied the X-ray emission in III Zw2 over three decades and find that the basic shape of the X-ray spectrum is a power-law with photon index $\Gamma \approx 1.7$. I do not find an excess at soft X-ray energies and the absorption is consistent with the line of sight Galactic column density. The *XMM − Newton* and *ASCA* spectra show excess emission between 5.5−7.5 keV, which cannot be entirely explained in terms of fluorescence Fe K_α emission from a low inclination relativistic disk. A contribution from the relativistic jets and/or ejecta to the Fe K_α emission could explain the observed line profile in III Zw2.

I observe large amplitude (10-fold) flux variations in the 25 year X-ray light curve, however I do not detect significant rapid variations (few 10^3 s) in fiux, in the individual observations, which is consistent with a large mass black hole in this system. I infer a black hole mass of $\sim 10^9 M_\odot$ (from H_β FWHM) for III Zw2 which is much higher than some previous estimates.

Multi-wavelength light curves show related variations from the radio to the X-rays. I interpret the radio to optical emission as synchrotron radiation, self-absorbed in the radio/millimeter region, and the X-rays as consisting of a significant contribution from the Compton up-scattering of low-energy photons by the population of high-energy electrons that give rise to the synchrotron radiation.

Chapter 4

Evidence for an ionised accretion disk in MCG-2-58-22

4.1 Introduction

MCG-2-58-22 (Mrk 926, $z = 0.04732$) is a Seyfert 1 Galaxy located at a distance of 284 Mpc ($H_0 = 50$ km s^{-1} Mpc^{-1}, Huchra et al. 1993). It is a strong X-ray source ($L_{2-10} \sim$ few 10^{44} erg s^{-1}; Ghosh & Soundararajaperumal 1992) and has been studied many times in this wave-band over the last 20 years (Nandra et al. 1994, Grandi et al. 1992, Weaver et al. 1995). The power-law indices measured for the X-ray continuum spectrum, range from $\Gamma = 2.1 \pm 0.06$ in *ROSAT* (0.1−2.0 keV band; Piro et al. 1997) to $\Gamma \sim 1.5 \pm 0.03$ in *GINGA* (2-18 keV band; Nandra et al. 1994).

The presence of a hard, high energy spectrum has led to the speculation that there is a substantial reflection component (George et al. 1991, Lightman et al. 1988) in the X-ray emission of the source. However, based on ASCA data, Weaver et al. (1995) argue that the observations of MCG-2-58-22 are consistent with a 'bare' Seyfert nucleus; i.e. the source is not intrinsically absorbed and does not exhibit strong reflection. The lack of substantial reflection in MCG-2-58-22 is also inferred from the *GINGA* (Nandra et al. 1994) and *RXTE* observations of the source where

a weak reflection fraction of < 0.08 (Weaver 2000) is measured.

The *ASCA* data also showed evidence of a Fe K_α line with an EW of $\sim$ 340 eV which reduces to about $\sim$ 150 eV on addition of a reflection component (Weaver et al. 1995). Hence a good estimate of the reflection in MCG-2-58-22 is required for reliable measurements of the Fe K_α line. A simple extrapolation of the 2-10 keV spectrum leads to an excess of flux at lower energies (Piro et al. 1997). The spectrum at lower X-ray energies (0.1−2 keV) has been reported as having complex structures and is not a simple absorbed power-law (Choi et al. 2002). The soft band flux exhibits low level (10%−30%) variability on time-scales of 10^3 s to $\sim$ few days (Choi et al. 2002, Ghosh & Soundararajaperumal 1992), while the 2-10 keV flux is only known to vary on time-scales of months (Grandi et al. 1992, Weaver 2000, Choi et al. 2002).

In the optical MCG-2-58-22 exhibits very broad Balmer lines (H_β FWHM = 6800 km s^{-1}; Osterbrock et al. 1982). It is classed as a radio weak object, but it does show a compact (sub-parsec scale), high brightness, flat spectrum radio core with weak east-west extensions. Such flat spectrum cores have been detected in only a few Seyfert galaxies and are interpreted as self-absorbed synchrotron radio emission from the base of a relativistic jet (Mundell et al. 2000).

In this chapter I present results of simultaneous XMM-Newton and BeppoSAX observations. The high signal-to-noise XMM-Newton data allows me to measure the underlying continuum and the iron line parameters with much higher accuracy than was possible with previous missions. The broad energy range of the BeppoSAX data helps constrain the reflection component. In §4.2, I discuss the observations and data reduction techniques. In §4.3 I present X-ray and multi-wavelength light curves. §4.4 contains detailed spectral modeling over the 0.3-100 keV energy range. I consider whether reflection models incorporating Compton reflection and X-ray lines due to the re-processing of the primary photo-ionising continuum by the accretion disk can reproduce the observed spectrum of MCG-2-58-22. A discussion of the various models fitted to the data and the possible origins of the observed spectral

features is presented in §4.5.

4.2 Observations

4.2.1 X-ray emission

MCG-2-58-22 was observed simultaneously with $XMM-Newton$ and $BeppoSAX$, providing an opportunity to study its X-ray emission over a broad energy range.

The $XMM-Newton$ observation took place on 2000 December 1, from 17:52:51 UT to 21:07:57 UT. The 10 ks of MOS2 data and 7 ks of PN data were taken in the small window mode. Thin filters were used in both EPIC cameras. The RGS had a relatively longer exposure of 23 ks. MOS1 data were taken in timing mode and have not been included in this study. Images of MCG-2-58-22 were also taken with the optical/UV monitor (OM) of $XMM-Newton$. The images were taken through the UVW2, UVM2, UVW1, U, B and V filters which cover the full 1600Å–5500Å OM wavelength range.

The $BeppoSAX$ observation lasted from 2000 December 01 11:27 UT to December 5 12:31 UT. I present $BeppoSAX$ results obtained with the Low-Energy Concentrator Spectrometer (LECS; 0.1–10 keV; Parmar et al. 1997), the Medium-Energy Concentrator Spectrometer (MECS; 1.65–10 keV; Boella et al. 1997) and the Phoswich Detection System (PDS; 15–300 keV; Frontera et al. 1997). The net exposures in the LECS, MECS and PDS instruments are 22.9 ks, 66.8 ks and 40.8 ks, respectively.

Data reduction

The $XMM-Newton$ EPIC data were reduced using the XMM standard analysis system (SAS), version 5.3.3. Source spectra and light curves from the MOS and PN detectors were extracted using circles of radius 40" with pattern 0-12 (MOS2) and 50" with pattern 0 (PN) in XMMselect. The background spectra and light

Filter	Wavelength (Å)	Flux (erg cm^{-2} s^{-1} $Å^{-1}$)
UVW1	2400-3600	8.49×10^{-15}
UVM2	2000-2800	7.70×10^{-15}
UVW2	1800-2600	7.99×10^{-15}
U	3000-4000	7.23×10^{-15}
B	3800-5000	9.33×10^{-15}
V	5000-6000	6.47×10^{-15}

Table 4.1: Fluxes for the optical monitor filters. The data are corrected for Galactic extinction.

curves were extracted using circular apertures from a source free region on the same chip for PN and on a neighbouring chip for MOS2. RGS data were reduced using *XMM – Newton* SAS V5.2 and were further processed by M.Page according to the recipe described in Chapter 3. For MCG-2-58-22, the RGS spectrum was grouped by a factor of 3 to improve signal to noise.

The OM data were reduced using *XMM – Newton* SAS V5.2. The source and background count rates for each filter were obtained using circles of radius 10". The background subtracted count rates were corrected for dead time and coincidence losses (using the *XMM – Newton* users handbook) and converted to fluxes using the standard recipe[1] (see appendix B). The data were corrected for Galactic extinction using the reddening law of Allen (1976) and E(B-V) = 0.042 mag (Schlegel et al. 1998). For details see appendix B. The fluxes for the different OM filters are listed in Table 4.1.

The *BeppoSAX* data were reduced by A.Orr using the SAXDAS 2.0.0 data analysis package in the following manner. Good data were selected from intervals when the elevation angle above the Earth's limb was >4° and when the instrument configurations were nominal. The standard PDS collimator dwell time of 96 s for each on- and off-source position was used together with a rocking angle of 210'. LECS and

[1]http://xmm.vilspa.esa.es/external/xmm_sw_cal/sas_frame.shtml

MECS data were extracted using radii of 8' and 4', respectively. Background subtraction for the LECS and MECS were performed using the standard background files. The PDS background was estimated from the offset field according to the standard procedure.

4.2.2 Multi-wavelength emission

In order to study the emission in MCG-2-58-22 over a broader spectral range all available data on the source from UV to radio wavelengths were compiled from previous publications. Ultraviolet data are from the IUE archives. The optical UBVRI data from 1987 to 1990 are from Winkler et al. (1992), while the 1979, 1985 and 1993 data are from McAlary et al. (1983), Hamuy & Mazu (1987) and Kolilainen et al. (1993) respectively.

The infrared JHKLM data for 1978/1980, 1979, 1982 and 1988/89 have been obtained from Glass (1981), McAlary et al. (1983), Ward et al. (1987) and Kotilainen et al. (1993) respectively. The radio data are from Wilson et al (1982) and Bicay et al. (1994).

4.3 Light curves

4.3.1 X-ray

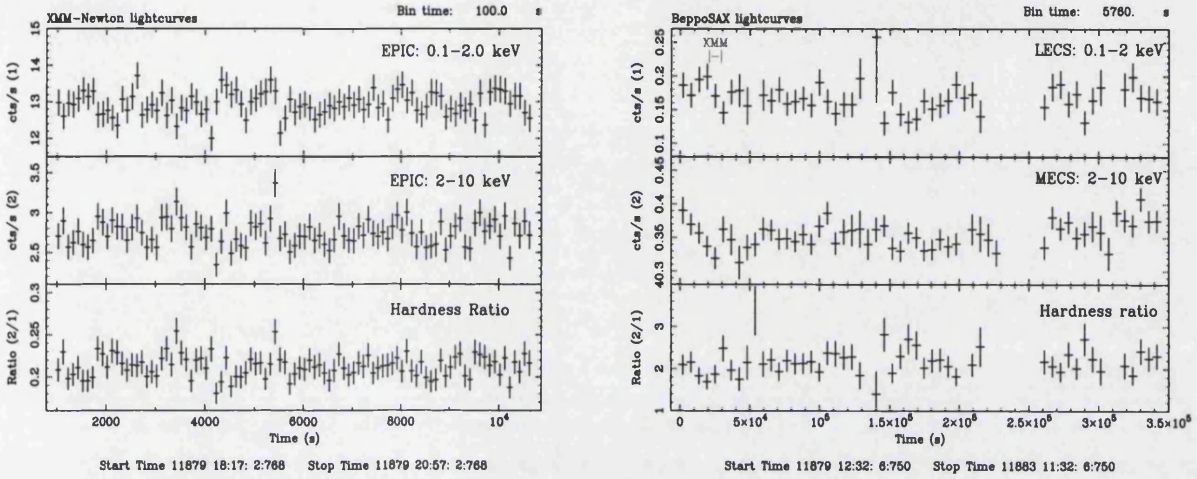

Figure 4.1: *Left* :Light curves and hardness ratio for the 10 ks $XMM-Newton$ exposure *Right* : Light curves and hardness ratio for the long *BeppoSAX* exposure. The time of the $XMM-Newton$ observation is marked by the small bracket in the upper right panel.

Fig 4.1 shows the $XMM-Newton$ and *BeppoSAX* light curves. The duration of the $XMM-Newton$ observation is a small fraction of the BeppoSAX exposure and is marked by the small bracket in the upper right panel in Fig 4.1. A time binning of 100 s is used for the $XMM-Newton$ data and the *BeppoSAX* data are binned to 5760 s (corresponding to the satellite orbital period of 96 minutes). I performed a χ^2 test to look for variability in both the XMM-Newton and *BeppoSAX* light curves. Results of this test for each time series are listed in Table 4.2. I do not detect significant X-ray variability over time-scales of a few 100 s to a few days in MCG-2-58-22.

Mission	Energy keV	Bintime sec	χ^2/dof	Prob of constancy
XMM-Newton	0.1−2.0	100	114/104	0.23
	2.0−10.0	100	125/104	0.08
BeppoSAX	0.1−2.0	5760	29/49	0.99
	2.0−10.0	5760	67/53	0.09

Table 4.2: Results of the statistical test to determine the constancy of the $XMM-Newton$ and $BeppoSAX$ light curves . There is no significant variation in X-ray flux of MCG-2-58-22 during either of the observations.

Although the X-ray flux in MCG-2-58-22 does not vary significantly over time-scales of $\leq$ few days, over longer time-scales (few years) the 2−10 keV emission exhibits 6-fold flux variations. Fig 4.2 shows the variations in X-ray flux of MCG-2-58-22 over a period of 25 years (also see Choi et al. 2002). The X-ray data presented is compiled from various publications as listed below:

$HEAO-I$ (Piccinotti et al 1982), *Einstein* 1979 (Turner et al. 1991), $EXOSAT$ 1984/85 (Ghosh et al. 1992), $GINGA$ 1989/90 (Nandra et al. 1994), $GINGA$ 1991, $EXOSAT$ 1983, $ROSAT$ 1990−1993, $ASCA$ 1997, $RXTE$ 1997−1999 (Choi et al. 2002), $ASCA$ 1993 (Weaver et al. 1995).

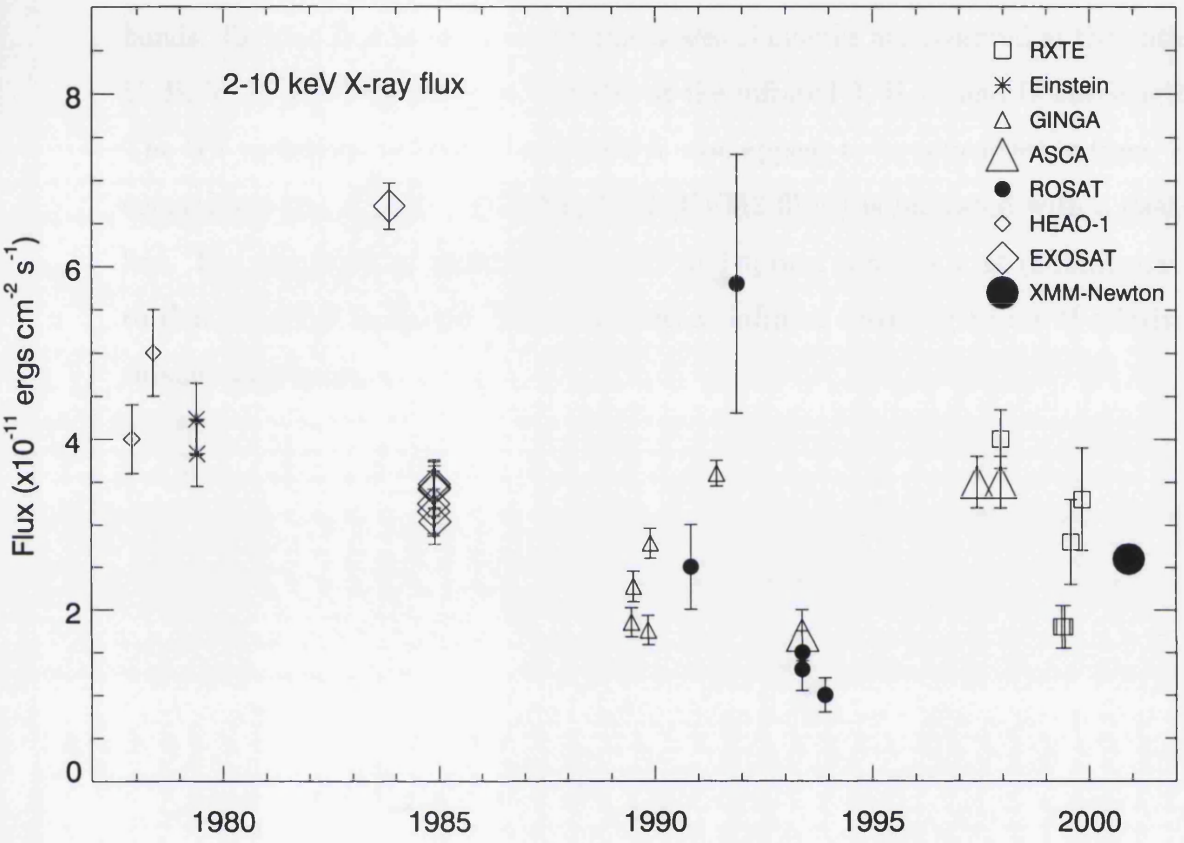

Figure 4.2: The X-ray emission in MCG-2-58-22 does not vary significantly over time-scales of $\leq$ few days but shows 6-fold flux variations over longer time-scales of years. The X-ray data presented here, with the exception of *XMM – Newton* have been complied from various publications (see text for details)

4.3.2 Multi-wavelength

Fig 4.3 shows the optical, infrared and UV emission in MCG-2-58-2 over several years. Note that the observational time-scales are not the same for the three wave-bands. Related flux variations over time-scales of months are observed at the optical U, B, V, R and I wavelengths and also at the infrared J, H, K and L wavelengths. The UV variations at 1308 Å and 2303 Å also appear to be coincident in time. For comparison the $XMM - OM$ flux level (UVM2 filter) is indicated with a dashed line. The amplitude of variation in the UV and optical bands is large (5-fold) similar to that observed in X-rays. The variations at infrared wavelengths are of relatively smaller amplitude.

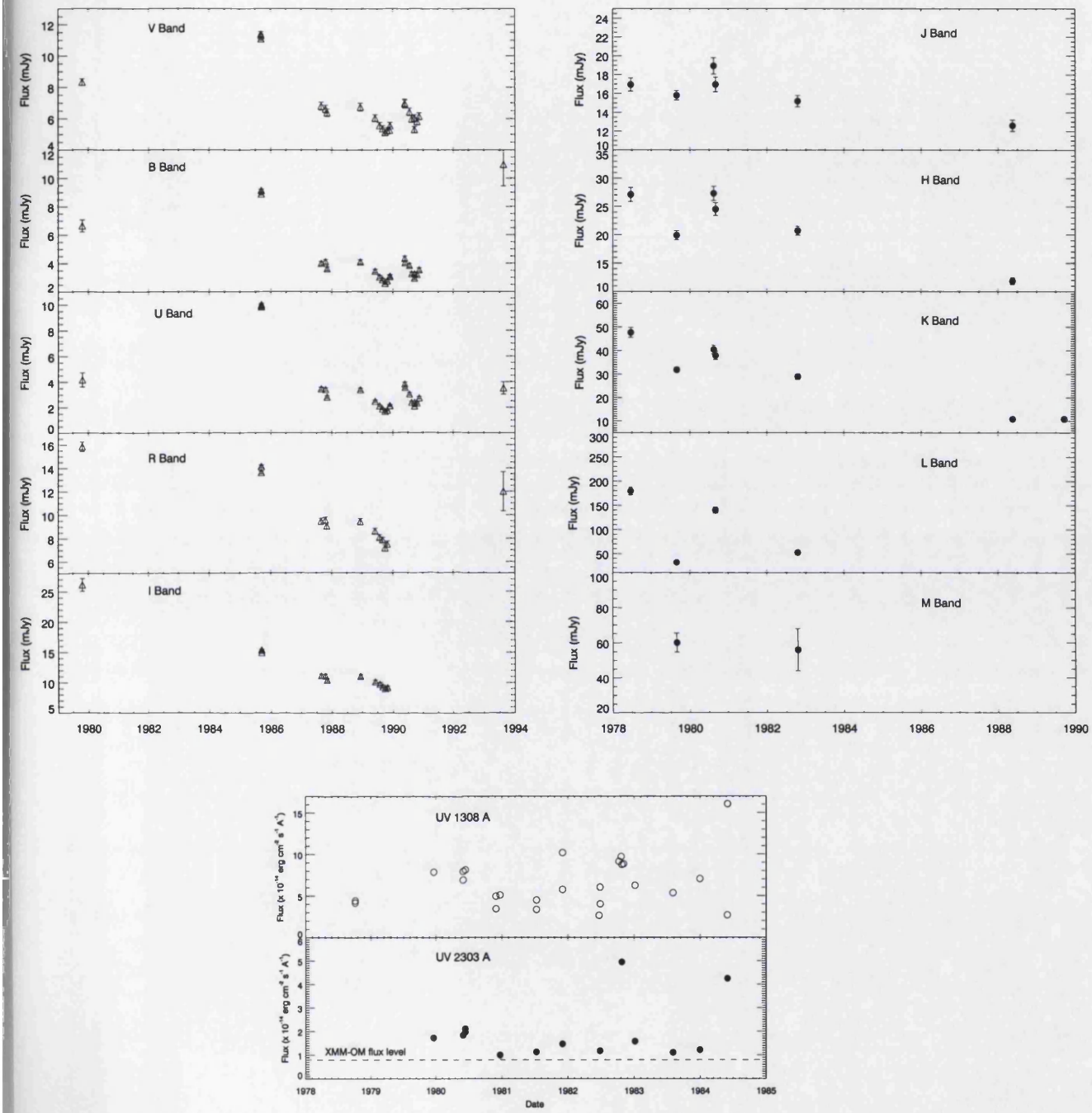

Figure 4.3: Light curves showing related variations at the optical, IR and UV wavelengths. Note that the observational time-scales are different for the three wave-bands.

4.4 X-ray spectra

Spectral fitting of X-ray data was performed using the XSPEC software package version 11.1. All emission line energies quoted in the text are in the rest frame of the source and errors are quoted at the 90% confidence ($\Delta\chi^2 = 2.7$ for one interesting parameter) unless specified otherwise. Spectral fitting results are summarized in Table 4.3 and the broad band spectrum is plotted in Fig 4.4.

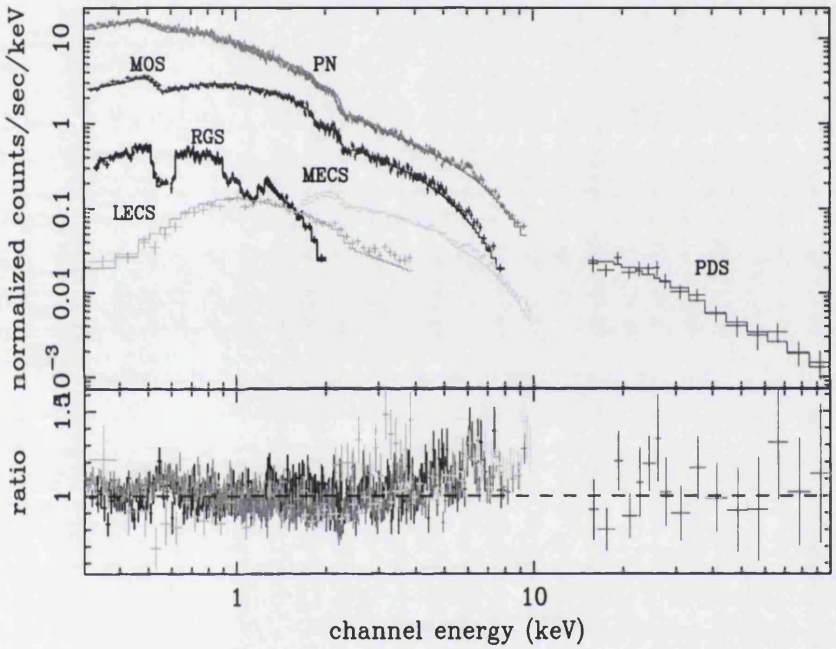

Figure 4.4: The 0.3−100 keV *XMM − Newton* and *BeppoSAX* spectra of MCG-2-58-22 (in the observers frame, $z = 0.04732$). The plot shows a power-law model fit to the data and the resultant fit residuals ($\Gamma = 1.86 \pm 0.01$, $\chi^2/dof = 2311/1713$). The Galactic column is fixed at $N_H = 3.6 \times 10^{20}$ cm^{-2}.

4.4.1 0.3−100.0 keV fits

The MOS and PN data were grouped to a minimum of 100 and 200 counts per bin respectively, and fitted over an energy range of 0.3−10.0 keV. The RGS data were

fitted over an energy range of 0.3−2.0 keV. The LECS and MECS spectra, covering the intervals 0.1−4 keV and 1.65−10 keV respectively, were grouped to a minimum of 20 counts per bin to allow use of the χ^2 statistic. The PDS data (15–100 keV) were rebinned using the standard logarithmic binning recommended by the PDS team for this instrument (Frontera et al. 1997).

Spectra from the RGS and EPIC detectors of $XMM-Newton$ and the LECS, MECS and PDS detectors of $BeppoSAX$ were fitted simultaneously during spectral analysis. As a preliminary check I fitted the total (0.3−100 keV) spectrum with a power-law and neutral absorption, both free to vary. This gives a photon index of $\Gamma = 1.78\pm0.01$ and $N_H = 1.83\pm0.16\times10^{20}$ cm^{-2} ($\chi^2/dof = 2018/1712$). The best fit neutral column density is less than the Galactic absorption measured in the direction of MCG-2-58-22 ($N_H = 3.6\times10^{20}$ cm^{-2}) and henceforth I fix the neutral absorption to the Galactic value for all spectral fitting. With the absorption column fixed to the Galactic value I obtain a photon index $\Gamma = 1.86\pm0.01$ with $\chi^2/dof = 2311/1713$, and this is the model shown in Fig 4.4.

A broad excess with respect to the power-law is visible between 5−7 keV and between 0.5−0.7 keV (Fig 4.4). Generally, broad line emission around 6 keV is thought to be Fe K_α due to X-ray irradiation of an accretion disk around a central black hole. Hence I checked if a 'Diskline' emission line model (Fabian et al. 1989) for a disk around a Schwarzschild (non-rotating) black hole could describe the observed excess between 5-7 keV. A power-law plus 'Diskline' model fit to the 0.3−100 keV spectrum yields a line at $E = 6.96^{+0.07}_{-0.12}$ keV ($i = 28°^{+3}_{-8}$, q = -4.66±0.15, EW = 575^{+100}_{-30} eV, $\Gamma = 1.89\pm0.01$) and is a significant improvement over a power-law model fit to the data ($\Delta\chi^2 = 270$ for 5 extra parameters, $\chi^2/dof = 2047/1708$).

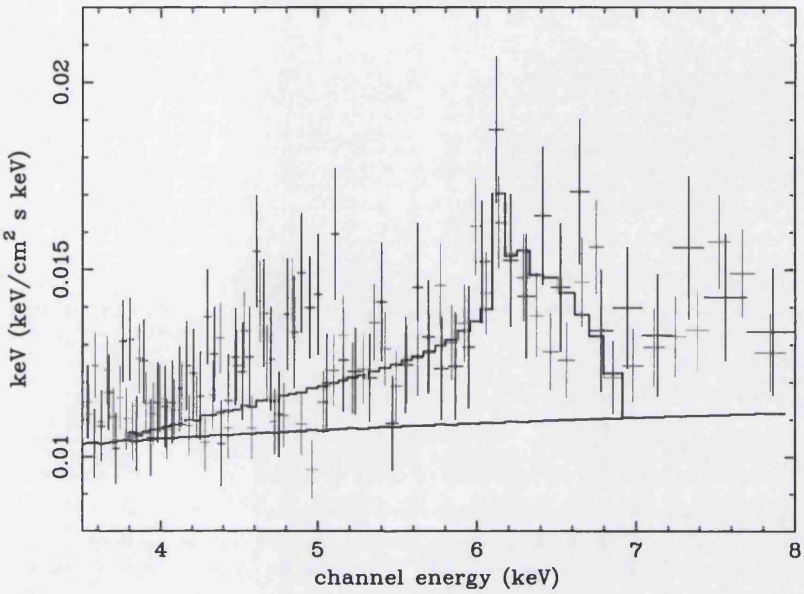

Figure 4.5: The plot shows the best fit model to the iron line profile (in the observers frame, z = 0.04732). The model includes a power-law, an ionised relativistic Fe K_α line (E = 6.83±0.26 emissivity $q = -2.99\pm0.67$ and inclination $i = 28°\pm10$) and a narrow Gaussian at 6.4 keV. The plot shows data from the MOS (dark points) and PN (light points). The dark solid line is the power-law model and the dark stepped curve on top of it is a model comprising a Laor emission line, a narrow Gaussian and power-law.

To investigate the presence of reflection in MCG-2-58-22 and its effect on the other spectral features present, I replaced the power-law component with a PEXRIV reflection model (Magdziarz et al. 1995) which comprises a power-law and Compton reflection ($i \leq 40°$) from ionised material (model=PEXRIV+diskline). The reflection fraction[2] obtained is high (R = $1.04^{+0.80}_{-0.12}$, Γ = 1.90±0.01) and the ionisation parameter $\xi = 72^{+10}_{-17}$ erg cm s^{-1} (where R = $\Omega/2\pi$ and $\xi = 4\pi F/n$). The iron line energy and EW are now reduced to $6.58^{+0.06}_{-0.19}$ keV and 250^{+70}_{-60} eV respectively (i =

[2]It is interesting to note, however, that if I fit the PEXRIV reflection model to just the hard band (2−100 keV) the reflection fraction obtained is lower (R = $0.38^{+0.51}_{-0.27}$, Γ = 1.65±0.14, $\xi < 600$ erg cm s^{-1}).

$33^{+3}_{-10}{}^{\circ}$, $q = -5.00^{+1.19}_{-1.23}$, $\Delta\chi^2 = 188$ for 3 extra degrees of freedom) with an overall fit statistic of $\chi^2/dof = 1859/1705$ (Table 4.3, model 3).

The resultant fit residuals still show a bump between 0.5−0.7 keV. Addition of a black body component at soft X-ray energies improves the fit ($> 3\sigma$) and yields a temperature of $kT = 135^{+9}_{-10}$ eV ($\Delta\chi^2 = 86$ for 2 extra parameter, $\chi^2/dof = 1773/1703$) but the bump between 0.5−0.7 keV still persists (Fig 4.7, panel 1, Table 4.3, model 4) . Replacing the black body component with a second power-law component (model=PEXRIV+PL+Diskline) results in a better fit to the data ($\Delta\chi^2 = 12$ for 0 extra parameter) but the 0.5−0.7 keV excess is still visible. The photon indices obtained are $\Gamma_{soft} = 2.07\pm0.01$ and $\Gamma_{hard} = 1.20\pm0.01$ with an overall fit statistic of $\chi^2/dof = 1761/1703$ (E = $6.86^{+0.04}_{-0.21}$ keV, R = $0.96^{+0.90}_{-0.03}$, Table 4.3, model 5).

Having failed to describe the excess emission at 0.4−0.9 keV using continuum components, I tried an emission line. If a narrow line is responsible for the bump, it will be very prominent in the RGS spectrum. As this is not observed, I consider a relativistically broadened O VIII line as observed in Mrk 766, MCG-6-30-15 and NGC 4051 (Branduardi-Raymont et al. 2000, Mason et al. 2003, Salvi et al. in preparation). The O VIII line energy was fixed to its red-shifted value ($z = 0.04732$) in the observer's frame and the outer disk radius was fixed at 1000 R_g. All other line parameters (emissivity index (q), inclination (i), inner radius (R_{in})) were tied for the O VIII and Fe Kα lines and fitted together. Addition of the O VIII line to the model makes a $> 4\sigma$ improvement to the fit ($\Delta\chi^2 = 42$ for 1 extra parameter, $\chi^2/dof = 1719/1702$) and the bump between 0.4−0.9 keV is no longer present in the residuals (Table 4.3, model 6). I obtain an O VIII equivalent width of 16^{+4}_{-5} eV. The iron line equivalent width and line energy is reduced to EW = 135^{+65}_{-45} eV and E = $6.84^{+0.12}_{-0.10}$ keV respectively, when fit simultaneously with the soft X-ray line.

Finally, I note that the addition of a narrow Gaussian ($\sigma = 0$) at 6.4 keV makes a further 3σ improvement to the fit ($\Delta\chi^2 = 13$ for 1 extra parameter, $\chi^2/dof = 1706/1701$). In this case, the narrow Fe K_α line has an EW of 39^{+16}_{-14} eV, while the

EW of the broad Fe K_α line is further reduced to 80^{+40}_{-53} eV (Table 4.3, model 7).

Reflection from an ionised disk

Having obtained a good fit using a model including ionised reflection and emission line profiles from an accretion disk around a black hole, I now consider whether the data can be fit by models with a self-consistent prescription for reflection and reprocessing of X-rays by an accretion disk. I fit the 0.3−100 keV spectrum of MCG-2-58-22 with the 'Constant Density ionised disc model (CD)' (Ross & Fabian, 1993, Ballantyne, Iwasawa & Fabian, 2001) and the XION 'hydrostatic balance (HB)' reflection model (Nayakshin et al. 2001) in XSPEC. The inclination angle for the reflection models was constrained between 0−40°. The main difference between the two models is that in the CD model the vertical density of the illuminated gas is assumed to be constant, independent of the value of the X-ray flux, while in the HB model the density of the gas is computed using the condition of hydrostatic balance.

A CD model fit to the 0.3−100 keV spectrum comprising a power-law and reflection component (χ^2/dof = 1860/1708, Table 4.3, model 8) yields a low reflection fraction (R = 0.40±0.03) with the power-law index Γ = 1.63±0.01 and ionisation parameter[3] $\xi < 11$ erg cm s^{-1} . The model does not reproduce the observed broad Fe K_α line profile nor the soft excess satisfactorily (Fig 4.7, panel 2) and I do not pursue it any further.

Using the HB model I fitted the 0.3−100 keV spectra with the magnetic flares and lamp post geometries. In the lamp post geometry the disk is assumed to be illuminated by a point-like X-ray source high above the black hole and the X-rays illuminate a large area of the inner disk. In the magnetic flare geometry the disk is assumed to be unevenly illuminated by X-ray sources very close to the disk (e.g. magnetic flares) such that the local X-ray flux is much greater than the disk flux

[3]The ionisation parameter of the CD model is defined differently from that of the PEXRIV model and as such the values of ξ will be 4.4 times smaller when compared directly with the values of ξ for the PEXRIV model (Orr et al. 2001)

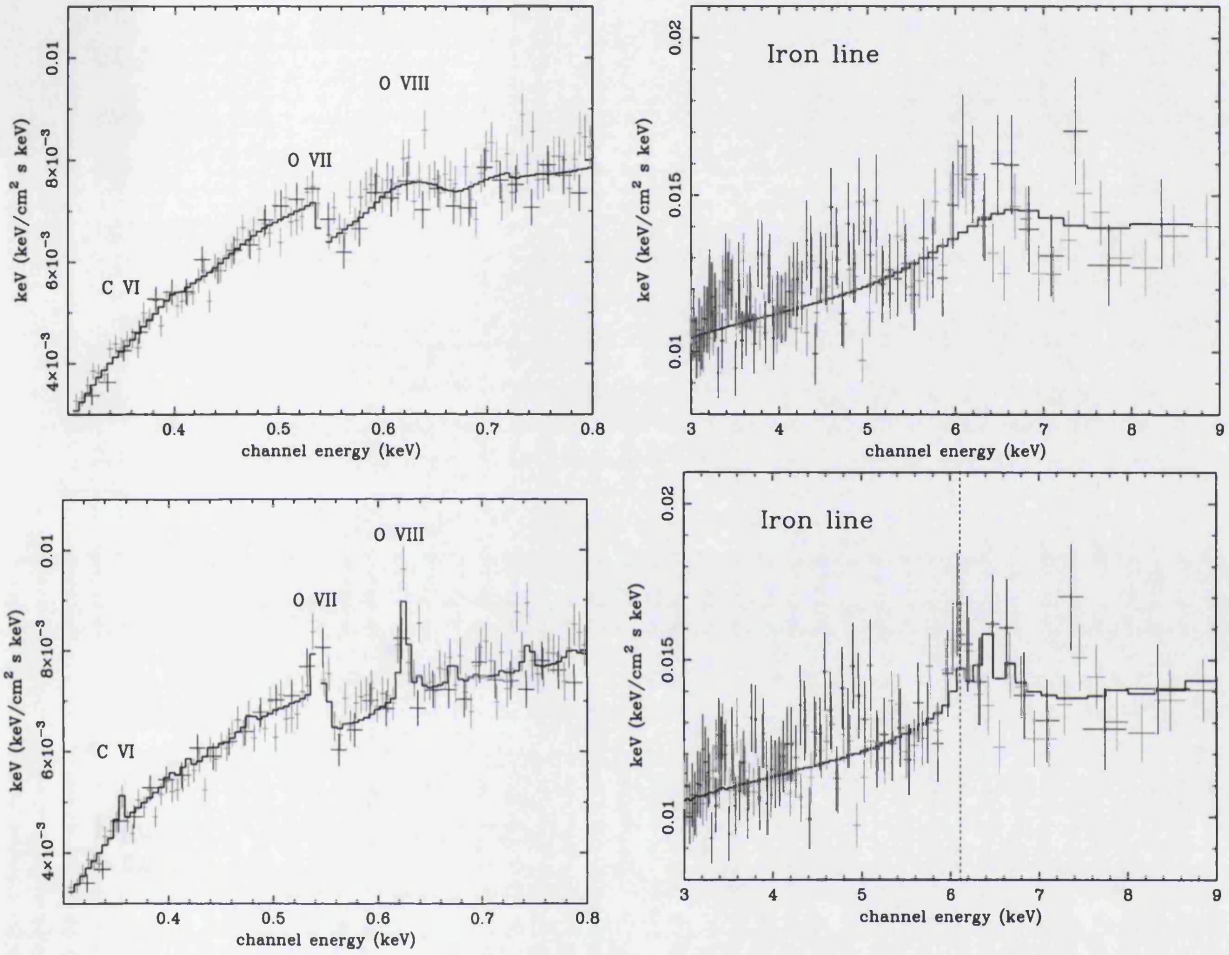

Figure 4.6: The hydrostatic balance reflection model (flare geometry) fit to the $XMM-Newton$ data (MOS and PN data are represented by the dark and light points respectively. Although the RGS data were included in the model fits they are noisy and have been excluded from the plots for visual clarity). The top panels show the relativistically smeared spectrum and the bottom panels show the unsmeared spectrum in the observers frame ($z = 0.04732$). The model reproduces the emission lump at low X-ray energies with a O VIII line. The model also produces O VII and C VI lines which become indistinguishable from the continuum when the spectrum is relativistically smeared. Most of the iron emission from the disk is at energies > 6.4 keV suggesting the presence of an ionised accretion disk in MCG-2-58-22. The position of the 6.4 keV line in the rest frame of the source is marked by a dashed line.

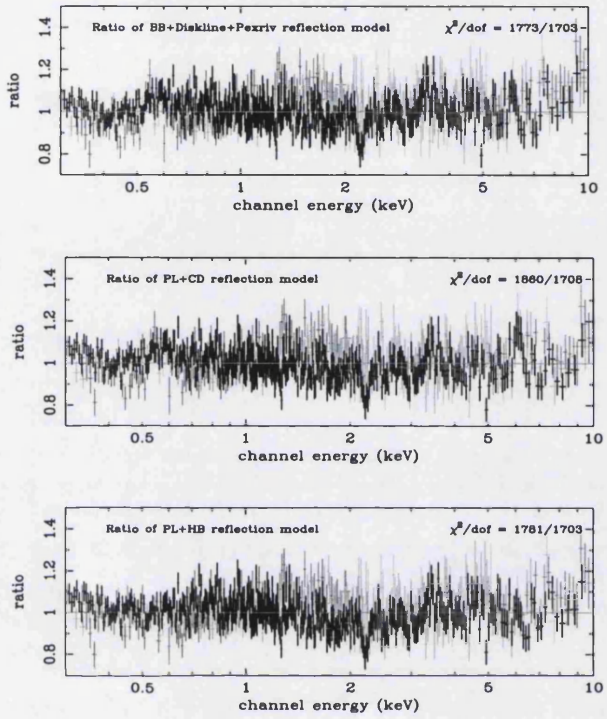

Figure 4.7: Ratio of $XMM/BeppoSAX$ data to different model fits (in the observers frame, z = 0.04732). The HB reflection model is statistically the best fit to the data

(see Nayakshin et al. 2000). I find that the flare geometry is a better fit to the X-ray data than the lamp post geometry ($\Delta\chi^2 = 22$ for 0 extra parameters). Also the lamp post geometry requires an X-ray flux 9 times larger than the disk flux to describe the data (Table 4.3, model 9). The X-ray flux is not larger than the UV flux in the XMM-Newton observations of the source (Fig 4.9) and so henceforth I use the flare geometry for all the HB reflection fits. A power-law plus HB reflection model fit to the 0.3−100 keV spectrum (Table 4.3: model 10, Fig 4.7: panel 3) yields a photon index of $\Gamma = 1.86\pm0.02$ ($\chi^2/dof = 1781/1703$).

I check whether the HB model has been able to account for all the soft X-ray continuum flux or whether an additional power-law component is required. A two power-law (Γ_{hard}= $1.31^{+0.06}_{-0.05}$, Γ_{soft}= $2.01^{+0.09}_{-0.06}$) plus HB reflection model (Table 4.3, model 11) is a significantly better fit to the data ($> 4\sigma$) than a single power-law plus a HB model , with a fit statistic of χ^2/dof = 1711/1701 ($\Delta\chi^2 = 70$ for 2 extra parameters). The model reproduces the soft X-ray spectrum, including the bump between 0.5−0.7 keV (Fig 4.6) as well as the Fe K_α emission line. The ratio of X-ray to disk flux $F_X/F_d = 3\pm1$, the model accretion rate (in Eddington units) $\dot{m}$ = $0.03^{+0.01}_{-0.005}$. Addition of a narrow ($\sigma = 0$) Gaussian fixed at 6.4 keV makes a small improvement to the fit ($>$ 95% confidence level, χ^2/dof = 1707/1700; Table 4.3, model 12).

No	Model	Γ	Energy$_{(Fe)}$ (keV)	emissivity (q)	EW (eV)	EW (Gau) (ev)	Refl fraction	ξ (erg cm s^{-1})	F_X/F_d	χ^2/dof
1	PL	1.86±0.01	-	-	-	-	-	-	-	2311/1713
2	PEXRAV +Diskline	1.90±0.01	$6.74^{+0.22}_{-0.44}$	$-5.00^{+1.00}_{-1.57}$	371^{+79}_{-55}	-	$1.00^{+0.95}_{-0.10}$	-	-	1921/1706
3	PEXRIV +Diskline	1.90±0.01	$6.58^{+0.06}_{-0.19}$	$-5.00^{+1.19}_{-1.23}$	250^{+70}_{-60}	-	$1.04^{+0.80}_{-0.12}$	72^{+10}_{-17}	-	1859/1705
4	PEXRIV+BB* +Diskline	1.87±0.01	$6.67^{+0.07}_{-0.12}$	$-6.67^{+0.89}_{-2.17}$	157^{+100}_{-30}	-	$0.98^{+1.01}_{-0.14}$	49^{+27}_{-19}	-	1773/1703
5	PEXRIV+PL +Diskline	$\Gamma_{soft}=2.07^{+0.01}_{-0.01}$ $\Gamma_{hard}=1.20^{+0.01}_{-0.01}$	$6.86^{+0.04}_{-0.21}$	$-5.00^{+0.47}_{-2.17}$	166^{+110}_{-50}	-	$0.96^{+0.90}_{-0.03}$	< 20	-	1761/1703
6	PEXRIV+PL +2[a] Disklines	$\Gamma_{soft}=2.01^{+0.01}_{-0.01}$ $\Gamma_{hard}=1.20^{+0.01}_{-0.01}$	$6.84^{+0.12}_{-0.10}$	$-3.10^{+0.53}_{-0.80}$	135^{+65}_{-45}	-	$1.00^{+0.17}_{-0.13}$	< 35	-	1719/1702
7	PEXRIV+PL +2[a] Disklines +Gaussian	$\Gamma_{soft}=2.00^{+0.01}_{-0.01}$ $\Gamma_{hard}=1.20^{+0.01}_{-0.01}$	$6.89^{+0.15}_{-0.18}$	$-3.03^{+0.49}_{-0.72}$	80^{+40}_{-53}	39^{+16}_{-14}	$1.00^{+0.22}_{-0.15}$	< 48	-	1706/1701
8	PL+Constant Density(CD)	1.63±0.01	-	-	-	-	0.40±0.03	< 11	-	1860/1708
9	PL+HB[l] (lampost)	1.86±0.01	-	-	-	-	-	-	9±2	1803/1703
10	PL+HB[f] (flare)	1.86±0.01	-	-	-	-	-	-	10±3	1781/1703
11	2PL+HB[f]	$\Gamma_{soft}=2.01^{+0.09}_{-0.06}$ $\Gamma_{hard}=1.31^{+0.06}_{-0.05}$	-	-	-	-	-	-	3±1	1711/1701
12	2PL+HB[f] +Gaussian	$\Gamma_{soft}=1.90^{+0.15}_{-0.11}$ $\Gamma_{hard}=1.30^{+0.06}_{-0.03}$	-	-	-	34^{+20}_{-16}	-	-	3±1	1707/1700

Notes:
* BB temperature $kT = 135^{+9}_{-10}$ eV
[a] O VIII and Fe K_α lines
[l] Lampost geometry
[f] Flare geometry
* The ionisation parameter of the CD model is defined differently from that of the PEXRIV model and as such the values of ξ will be 4.4 times smaller when compared directly with the values of ξ for the PEXRIV model (Orr et al. 2001).
The Galactic column is fixed at $N_H = 3.6\times10^{20}$ cm^{-2} for all spectral fits

Table 4.3: Results of the 0.3–100.0 keV spectral fits.

4.5 Discussion

4.5.1 The underlying continuum in MCG-2-58-22

I have used the combined data from $XMM-Newton$ and BeppoSAX to measure the X-ray spectrum of MCG-2-58-22 between 0.3 and 100 keV. The X-ray spectrum of MCG-2-58-22 is found to flatten with increasing energy. This is commonly seen in Seyfert 1 galaxies at E $\gtrsim$ 10 keV and is usually interpreted in the context of Compton reflection from the disk which results in a broad hump peaking at about 20−30 keV (Lightman & White 1988, George & Fabian 1991).

My spectral fits to the MCG-2-58-22 data imply a high reflection fraction (R $\approx$ 1) for the best fit models, and suggest that reflection from an ionised accretion disk makes a substantial contribution to the high energy X-ray spectrum. The reflection fraction that I measure using a single powerlaw plus cold disk reflection model is consistent with the (less well constrained) value derived by Weaver et al. (1995) who used a similar model to fit $ASCA$ data. Indeed the value I get for the reflection fraction is not sensitive to whether I use a PEXRAV (cold disk) model instead of a PEXRIV (ionised) disk model, consistent with the fact that the ionisation parameter derived from the PEXRIV fit is low. However, Weaver (2000) reports a very low value for the reflection fraction based on simultaneous fits to the $ASCA$ and $RXTE$ data, which is inconsistent with my data.

The constant density reflection model (PEXRIV and CD) fits to the data, yield a low ionisation parameter indicative of a relatively cold disk in MCG-2-58-22 which conflicts with the presence of a highly ionised Fe K_α line (6.8 keV). However, Nayakshin et al. (2001) have argued that the solutions of the CD models are unphysical (due to the unrealistic assumption of constant density) and that the CD models drastically under estimate the reflected spectrum especially if the disk is very ionised (also see Done et al. 2001) and must be treated with caution while interpreting data.

The reflection component cannot account for the observed flattening of the

power-law slope at E $\gtrsim$ 10 keV. The presence of a second hard power-law component ($\Gamma \approx 1.3$) extending up to 100 keV in addition to the $\Gamma \approx 2$ power-law and Compton reflection is indicated at $> 4\sigma$ significance (see Table 4.3). The two power-law components in the X-ray spectrum of MCG-2-58-22 intersect at around 8 keV and as such the 0.3−10 keV emission is dominated by the steeper power-law ($\Gamma \approx 2$) which is typically responsible for 75% of the total flux in that energy range. The hard power-law component is a major contributer to the observed X-ray emission only at energies > 12 keV.

The spectral index of the steeper power-law component measured using *XMM − Newton* ($\Gamma \approx 2$) is similar to that measured by *ROSAT* ($\Gamma \approx 2.1$) in the 0.1−2.0 keV range during four different observations spanning several years (1991 November 21, 1993 May 21-23, 1993 May 24-25 and 1993 December 1; Choi et al. 2002). It is interesting to note that although the spectral index was the same in the *XMM − Newton* and *ROSAT* observations, the 0.1−2.0 keV flux has varied by almost a factor of 4 (also see Choi et al. 2002). It appears that the $\Gamma \approx 2$ power-law emission in MCG-2-58-22, which dominates the *XMM − Newton* data up to 10 keV, is capable of large amplitude flux variations over time-scales of years without significantly changing its spectral shape.

The presence of 2 continuum components ($\Gamma < 1.6$ and $\Gamma \approx 2$) in the 0.1−10.0 keV emission of MCG-2-58-22 was also previously reported by Ghosh et al. (1992). They found evidence for low level variability ($\sim$ 30%) in the soft power-law flux and no change in the hard power-law flux over the period of few days. Low level variability ($\sim$ 10%) on time-scales of 10^3 s in the 0.1−2 keV emission of MCG-2-58-22 (ROSAT observation) has also been reported by Choi et al. 2002. The dominance of the steeper component up to 10 keV indicates that variations in flux previously measured in the 2−few 10's of keV energy range are most likely to be driven by changes in the $\Gamma \approx 2$ power-law emission and as such provide almost no reliable information on the hard ($\Gamma \approx 1.3$) power-law emission in MCG-2-58-22.

Compton up-scattering of low energy photons by hot electrons is still the widely

accepted explanation for power-law X-ray emission in AGN where the power-law photon index Γ depends on the optical depth and electron temperature.

$$\Gamma = 1 + \frac{ln\ \tau}{ln\ A} \simeq 1 + \frac{ln\ \tau}{ln\ [(\frac{16kT}{mc^2})^2]} \tag{4.1}$$

where A is the amplification of photon energy per scattering (Rybicki & Lightman 1979). One possible explanation for the observed two power-law components in the X-ray spectrum is that there exist at least two electron scattering regions of different temperatures and optical depths in the inner regions of MCG-2-58-22. My $XMM-Newton$ data favours the model in which the disk is illuminated by X-ray sources close to the disk surface. Such X-ray sources (conceptually identified with active regions in the corona, for example) may be likely candidates for one of the electron scattering regions in MCG-2-58-22, possibly the region responsible for the luminous $\Gamma \approx 2$ power-law emission which shows almost 6 fold flux variations over time-scales of years.

4.5.2 Emission lines

In addition to the underlying continuum the X-ray spectrum of MCG-2-58-22 shows two broad excesses around 0.6 keV and 6 keV, which can be satisfactorily modeled as O VIII and Fe K_α lines respectively from an accretion disk around a non-rotating black hole. Both emission features can also be reproduced by the hydrostatic balance reflection model in a self consistent manner along with the reflected continuum.

The detection of a relativistic O VIII emission line at low X-ray energies makes MCG-2-58-22 the newest member of a small group of Seyfert 1s (which include Mrk 766, MCG-6-30-15, NGC 5548 and NGC 4051; Mason et al. 2003, Branduardi-Raymont et al. 2001, Kaastra et al. 2000, chapter 4) which exhibit relativistic emission lines in their soft X-ray spectra. However, the sources in which these lines have

been previously detected are of lower luminosity ($L_{2-10} \lesssim 10^{43}$ erg s^{-1}) and this is the first detection of its kind in a high luminosity source. The line equivalent width (EW $\approx$ 16 eV) is lower than that observed in Mrk 766 (EW $\approx$ 140 eV; Sako et al. 2003, Branduardi-Raymont et al. 2001), MCG-6-30-15 (EW $\approx$ 160 eV; Sako et al. 2003, Branduardi-Raymont et al. 2001) and NGC 4051 (EW $\approx$ 70 eV; chapter 4), but comparable to that in NGC 5548 (EW $\approx$ 20 eV; Kaastra et al. 2000).

Although soft X-ray emission lines in Seyfert 1 galaxies were not detected prior to the launch of high resolution spectrographs such as those on $XMM-Newton$ and *Chandra*, their presence had been predicted by reflection models as a natural consequence of re-processing of the illuminating X-ray radiation by the disk. However, soft X-ray lines have as yet been detected in only a handful of sources and their absence in others is not understood. The results of model calculations of theoretical spectra from ionised accretion disks are sensitive to the assumed ionisation structure of the disk and as such differ substantially from one model to another (Sako et al. 2003, Ballantyne & Fabian 2001, Nayakshin et al. 2001). Reflection models by Ballantyne & Fabian (2001) predict substantial Fe L line emission which is not observed. The equivalent width predicted by Ballantyne & Fabian (2001) for the O VIII line (EW $\sim$ 10 eV) is consistent with that observed in MCG-2-58-22 and NGC 5548 but is much smaller than that observed in MRK 766, MCG-6-30-15 and NGC 4051 (70−160 eV). The Nayakshin et al. (2001) model successfully reproduces the equivalent widths of the O VIII lines in MCG-2-58-22 and NGC 4051. The model by Sako et al. (2002) predicts negligible Fe L line emission and O VIII line equivalent width of a few hundred eV as found in MCG-6-30-15 and Mrk 766.

Relativistically broadened iron lines have been detected (as yet) in only a small number of Seyfert 1 galaxies with $XMM-Newton$ and majority of the broad lines detected appear to be due to highly ionised iron (Gondoin et al. 2002, O'Brien & Reeves 2001, Mason et al. 2003). A disk line model fit to the excess around 6 keV in MCG-2-58-22 yields a line energy of 6.8±0.1 keV indicating emission from Fe XXV or greater. A similar result is obtained from the HB model fit to the X-ray data

which shows emission from heavily ionised iron (Fig 4.6). This suggests the presence of a highly ionised disk in MCG-2-58-22. The observed low EW of the broad iron line is also consistent with the HB model predictions for an ionised accretion disk (Nayakshin et al. 2001).

In addition to the broad Fe K_α line emission, there are also indications of a narrow line at 6.4 keV (FWHM $<$ 20,000 km s^{-1}) in MCG-2-58-22. Narrow Fe K_α lines are being detected in an increasing number Seyfert 1 galaxies (at least for $L_{2-10} < 10^{45}$ erg s^{-1}) with $XMM - Newton$ indicating an almost ubiquitous presence of relatively cold reflecting material at large distances from the central source (Reeves 2002, Pounds et al. 2002). A molecular torus (invoked by unified AGN theories) has been proposed as a likely candidate for the distant reflecting material in AGN by several authors in the past. The equivalent width of the narrow 6.4 keV line in MCG-2-58-22 is consistent with that expected from reflection of cold material (George & Fabian 1991). However, accurate measurements of the line width and flux variability are required to constrain the origin of the narrow line in MCG-2-58-22.

4.5.3 Multi-wavelength emission

The X-ray emission in MCG-2-58-22 does not vary significantly by a factor of 2 or more over short time-scales of few minutes which is typical of high luminosity sources. The absence of rapid variability is attributed to the presence of larger X-ray emitting regions possibly due to the presence of massive black holes at the centre of these sources (Green et al. 1993). I use the following mass relationship from Wandel et al. (1999) and the observed Hβ FWHM of 6800 km s^{-1} (Osterbrock et al. 1982) to estimate the black hole mass in MCG-2-58-22.

$$M_8 \approx 0.4\sqrt{\frac{L_{46}}{Un_{10}}} \times \nu_3^2 \tag{4.2}$$

where M_8 is the black hole mass in units of $10^8 M_\odot$, L_{46} is the bolometric luminosity in the units of 10^{46} erg s^{-1}, ν_3 is the Hβ FWHM in 10^3 km s^{-1}, n_{10} is the density in units of 10^{10} cm^{-3} and U is the ionisation parameter. A correction factor of 20 is applied to the the measured X-ray luminosity ($L_{2-10} = 3\times10^{44}$ erg s^{-1}) to obtain the bolometric luminosity ($L_{X-ray} = 0.05\ L_{bol}$; Elvis et al. 1994). Assuming (Un_{10}) = 1, I infer a black hole mass of $\approx 10^9\ M_\odot$ for MCG-2-58-22 which is consistent with the lack of rapid variability and is comparable to the mass estimate of Padovani & Rafanelli 1988.

An estimate of the black mass in MCG-2-58-22 can also be obtained from the accretion rate in Eddington units ($\dot{m} \approx 0.03$) obtained from HB reflection model fits using the equation;

$$M \approx \frac{L}{\dot{m}(1.3 \times 10^{38})} \tag{4.3}$$

where M is the mass in solar units, and L is the bolometric luminosity in erg s^{-1}. For a bolometric luminosity of 6×10^{45} erg s^{-1}, I infer a black hole mass of $\approx 10^9$

$M_{\odot}$ for MCG-2-58-22 which is consistent with the mass estimate obtained from the Hβ line.

On longer time-scales of years the 2−10 keV X-ray emission in MCG-2-58-22 exhibits large amplitude flux variations, a phenomenon commonly observed in AGN (Grandi et al. 1993). Spectral analysis results have shown that in the case of MCG-2-58-22 the steeper ($\Gamma \approx 2$) power-law component dominates emission in the 0.3−10 keV range. As such flux variations in the 2−10 keV energy range reflect the changes in the electron scattering region responsible for the $\Gamma \approx 2$ power-law emission and maybe be associated with the changes in mass accretion flow near the black hole (Uttley et al. 1999). At present there is very little information on the electron scattering region responsible for the $\Gamma \approx 1.3$ power-law emission in the source. More flux measurements at energies higher than 12 keV will be required to understand the behaviour and nature of the hard power-law component.

Large amplitude variations are observed at UV, optical and IR wavelengths (Fig 4.8) as well as in the X-rays. Although the data in these wave bands are not sufficiently sampled to determine whether there is a correlation between the multi-wavelength flux variations the gradual decrease in flux at X-ray and optical (and possibly IR) wavelengths between 1984−1990 hints at some possible connection between the wave-bands.

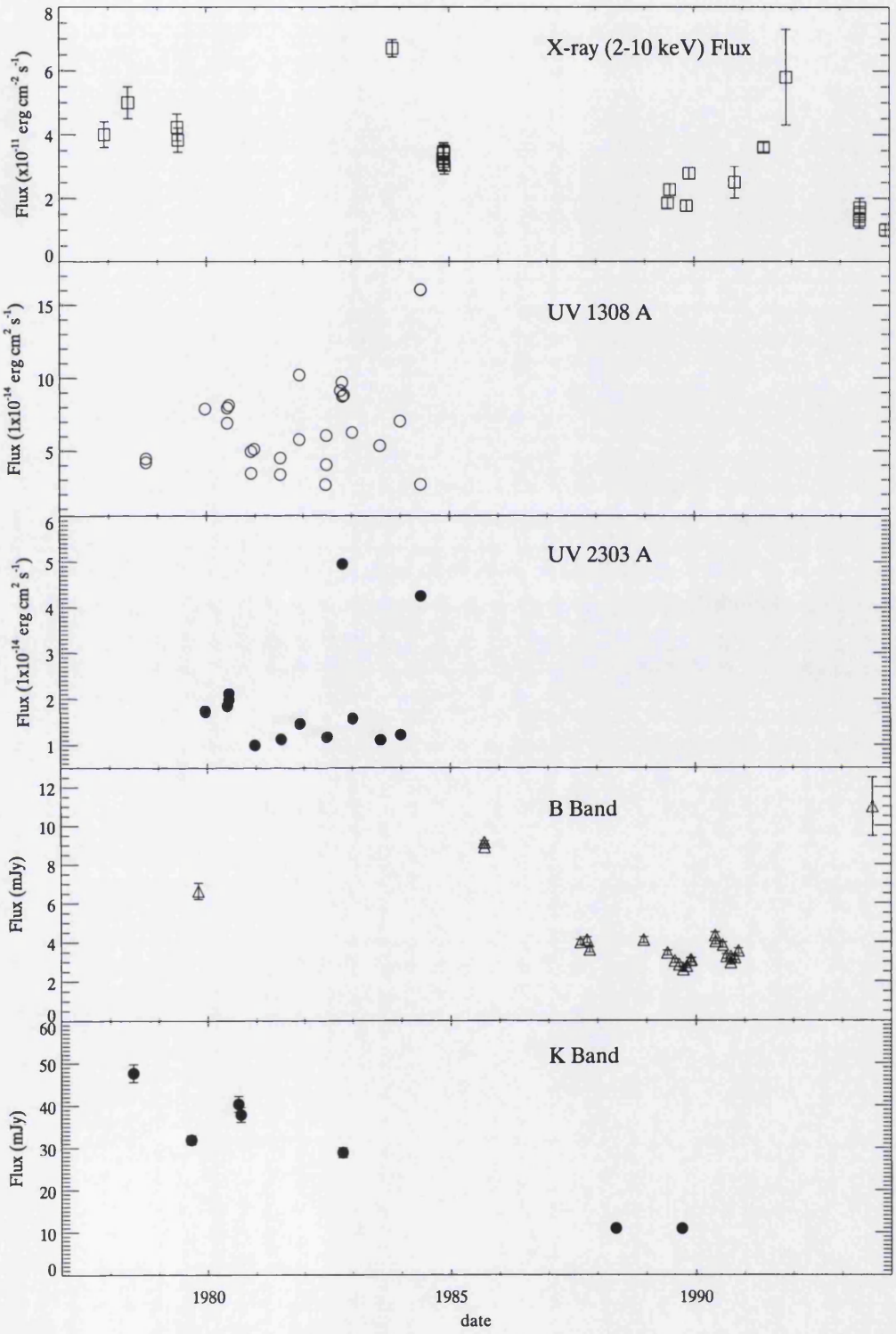

Figure 4.8: Light curves showing flux variations at the optical, IR and UV wavelengths. Although the wavelengths are poorly sampled the gradual decreases in flux at the X-ray and optical wavelengths between 1984−1990 hints at some connection (possibly time lagged) between the two wave-bands

Fig 4.9 shows the range of spectral energy distribution (SED) observed in MCG-2-58-22 with the mean radio quiet quasar SED plotted underneath for comparison (Elvis et al. 1994) . The dark optical–X-ray points represent the simultaneous $XMM-Newton$ and $BeppoSAX$ observations and the lighter open circles are the archival data.

The SED of MCG-2-58-22 is almost flat in the near infrared to optical region and appears to turnover in the UV showing a gradual decrease at frequencies blue-ward of $\sim 7\times10^{14}$ Hz. I do not find evidence for intrinsic absorption in the X-rays and it is unlikely that the observed decline in the UV region is due to absorption. As such the peak in the optical/UV emission must lie somewhere below 10^{15} Hz which suggests a disk temperature of < 10 eV (assuming that the optical/UV peak represents thermal emission from an accretion disk; Malkan 1983, Czerny & Elvis 1987). This is consistent with the black hole mass estimate of $\approx 10^9 M_\odot$ obtained for MCG-2-58-22.

The almost 4 decade drop in power output in the sub-millimeter band of MCG-2-58-22 is typical of radio quiet AGN. However, the hard X-ray luminosity and the optical-UV luminosity are similar, which contrasts with the mean radio-quiet quasar SED where the UV is a factor of ten more luminous. In the context of the patchy corona model (Haardt et al. 1997), the almost comparable UV and X-ray energy density in MCG-2-58-22 suggests that the fraction of the total gravitational energy dissipated in the corona is close to unity. If this is correct, the disk would be strongly irradiated by the coronal X-ray radiation. This picture is consistent with the inferred high ionisation state of the accretion disk in MCG-2-58-22.

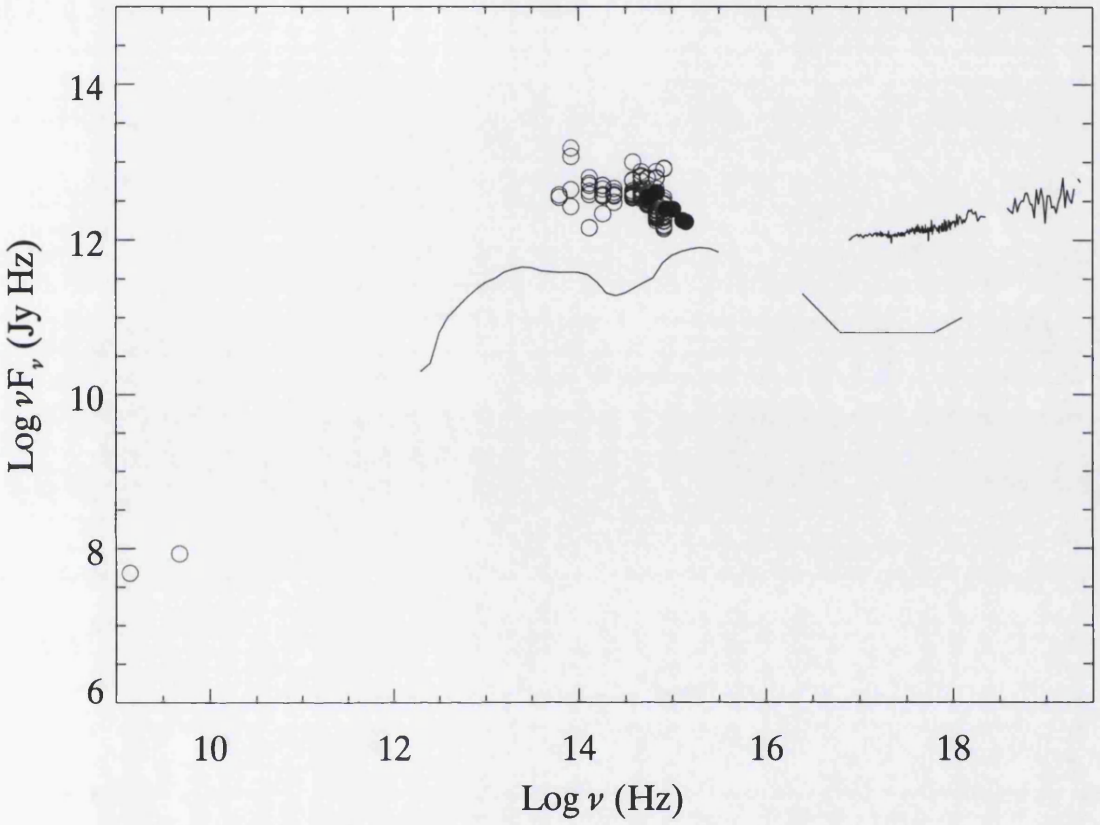

Figure 4.9: The radio to X-ray spectral energy distribution of MCG-2-58-22 includes data over 25 years. The dark optical−X-ray points represent the simultaneous $XMM-Newton$ and $BeppoSAX$ observations. The $XMM-Newton/BeppoSAX$ data have been corrected for Galactic reddening and absorption. The mean spectral energy distribution (scaled for plotting purposes) of a radio-quiet quasar (Elvis et al 1994) is plotted underneath for comparison.

4.6 Summary

The underlying continuum in the 0.3−100 keV spectrum of MCG-2-58-22 can be modelled by 2 power-law components and reflection from an ionised accretion disk. The reflection fraction inferred (R = 1) is much higher than some previous estimates. The spectrum below 8 keV is characterized by a power-law of photon index $\Gamma \approx 2$ and the higher energy spectrum by a harder power-law of $\Gamma \approx 1.3$. One possible explanation for the observed two power-law components is that there exist at least two electron scattering regions with different temperatures and optical depths in the inner regions of MCG-2-58-22.

I find evidence for the presence of a broad O VIII line in the X-ray spectra of MCG-2-58-22 and this is the highest luminosity Seyfert galaxy so far found to show such a feature. A broad Fe K_α line from highly ionised iron ($E \approx 6.8$ keV) is detected which is consistent with the presence of a heavily ionised accretion disk in MCG-2-58-22. There may also be a narrow Fe line component from cold material. Both the broad Fe K_α and O VIII emission lines can also be reproduced in a self consistent manner by a hydrostatic balance reflection model for an accretion disk around a non-rotating black hole.

I estimate a black hole mass of $\approx 10^9 M_\odot$ which is consistent with the lack of rapid variability in our data and is comparable with previous mass estimates of the source.

Chapter 5

Time resolved X-ray spectroscopy of NGC 4051

5.1 Introduction

NGC 4051 is a low luminosity ($L_{2-10} = 10^{40}-10^{41}$ erg s^{-1}; Uttley et al. 1999, Guainazzi et al. 1998, Collinge et al. 2001), narrow line Seyfert 1 Galaxy (NLS1). It is located at a distance of 14 Mpc ($H_0 = 50$ km s^{-1} Mpc^{-1}, $z = 0.0023$) and the mass of the central black hole is estimated to be $\sim 10^6$ $M_\odot$ (Peterson et al. 2000). It has been extensively studied over the last three decades, mainly due to its intriguing X-ray properties: large amplitude, extremely rapid and sometimes non-linear variability (Uttley et al. 1999, Green et al. 1999, Collinge et al. 2001), steep ($\Gamma \approx 2.3$) and variable soft X-ray spectra (Komossa et al. 1997) and re-occurring ultra-low flux states lasting up to 150 days, when the nuclear flux is a factor of 20−35 lower than its long term average value (Uttley et al. 2001, Uttley et al. 1999, Guainazzi et al. 1998). During these low states the source exhibits an unusual spectrum: anomalously soft ($\Gamma \approx 3$) at low X-ray energies and hard ($\Gamma \approx 1$) at energies > 2 keV (Guainazzi et al. 1998).

The rapidly varying X-ray emission in NGC 4051 is correlated with the EUV

emission with almost no significant time lags between the two bands (Uttley et al. 1999). On time-scales of several hours the UV emission (2900 Å) may be correlated with the modulations in X-ray flux (underlying the rapid variations) with a lag of ~ 0.14 days (Mason et al. 2002). The optical and X-ray emission is not correlated on timescales less than $\sim$ a day (Done et al. 1990). Although the rapid variability observed in the X-ray band is not detected in the optical, the time averaged X-ray and optical continuum emission is found to be correlated on time-scales of several days (Peterson et al. 2000). Near IR outbursts have also been detected in NGC 4051 (Salvati et al. 1993) but their connection (if any) with the X-ray emission is yet unclear.

NGC 4051 is optically bright (V $\approx$ 12.9– 13.5; Veron-Cetty & Veron 1985, de Vaucouleurs et al. 1991) and its spectral energy distribution has a power-law shape ($\alpha = 1.28$) from near IR to optical (Done et al. 1990, Malkan & Filippenko 1983). The galaxy also shows evidence of conical outflows and a subarcsecond triple radio source consistent with collimated ejection on a < 40 pc scale (Christopoulou et al. 1997).

In this chapter I study the spectral and temporal behaviour of the 0.3–10.0 keV X-ray emission in NGC 4051. I examine how the different spectral components (both the continuum and the lines) vary over time, by extracting spectra for every 10 ks of the observation. I also investigate if reflection from an accretion disk could reproduce the emission features seen in excess of the underlying continuum in NGC 4051. The chapter is arranged as follows. The observations and data reduction are described in §5.2. Spectral analysis of the integrated (103 ks) and time resolved spectra is discussed in §5.3. In §5.4 I discuss my findings and finally present my conclusions in §5.5.

5.2 Observations

5.2.1 XMM-Newton

NGC 4051 was observed with $XMM-Newton$ for 103 ks from UT 11:52:05 2001 May 16 to UT 20:22:31 on 2001 May 17. MOS2 and PN data were taken in the small window mode. Medium filters were used in both EPIC cameras. MOS1 data were taken in timing mode and have not been included in this study. Images of NGC 4051 were also taken with the optical monitor (OM) of $XMM-Newton$ using the UVW2, UVM2 and UVW1 filters which cover the 1800Å −3600Å wavelength range (Fig 5.1).

The $XMM-Newton$ EPIC data were reduced using the XMM standard analysis system (SAS), version 5.2. Source spectra and light curves were extracted using a circle of radius 42" with pattern 0-12 for the MOS2 detector and using a circle of radius 43" with pattern 0 for the PN detector in XMMselect. The background spectra and light curves were extracted using circular apertures from a source free region on the same chip. RGS data were reduced using $XMM-Newton$ SAS V5.2. The final combined RGS1 and RGS2 spectrum was obtained using the recipe (M. Page) described in chapter 3. The RGS spectrum was grouped by a factor of 3 to improve signal to noise.

The OM data were reduced using $XMM-Newton$ SAS V5.2. OM images taken with the UVW2 (1800−2600Å), UVM2 (2000−2800Å) and UVW1 (2400−3600Å) filters are shown in Fig 5.1.

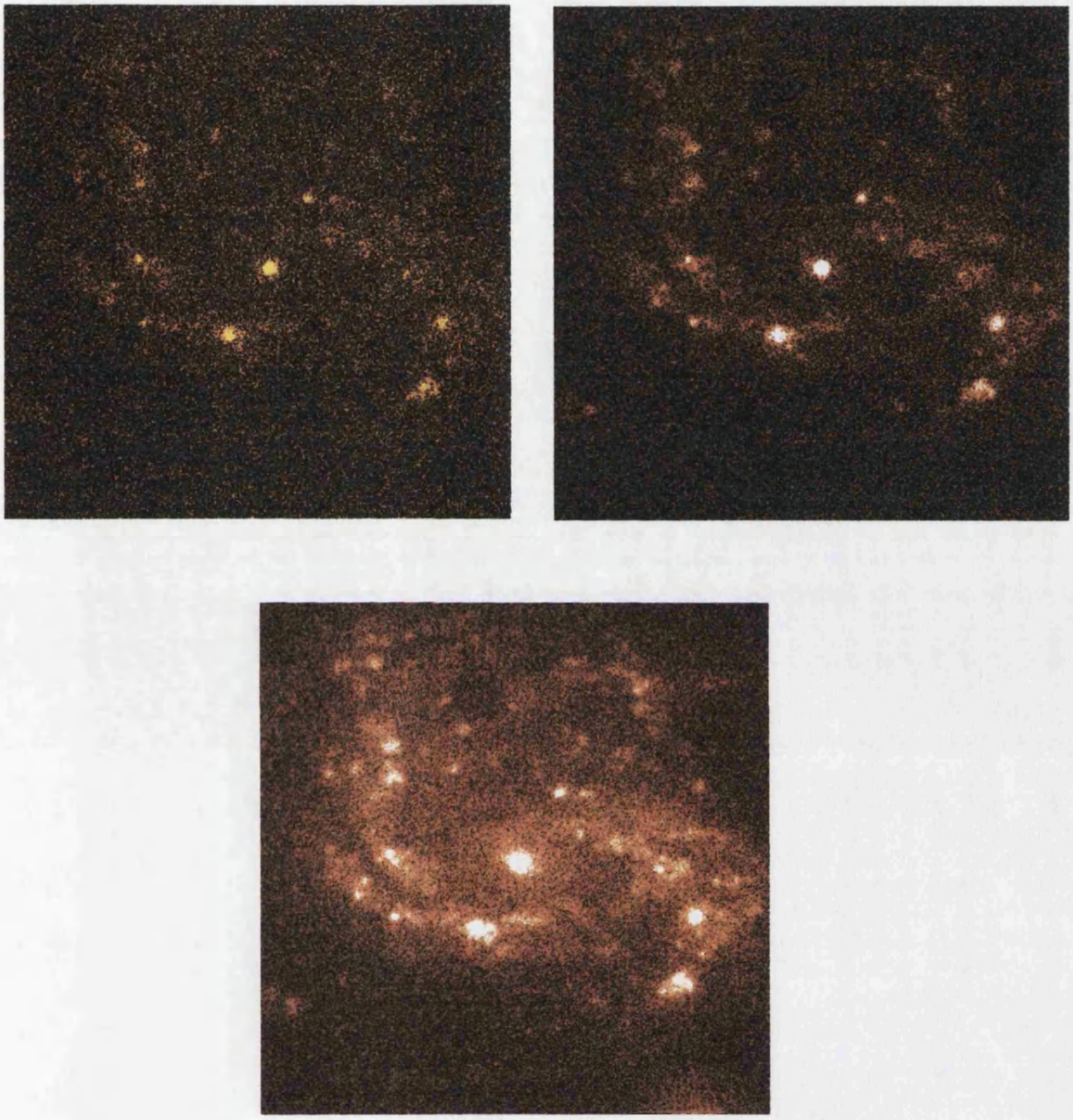

Figure 5.1: OM images of the NGC 4051 galaxy taken with the UVW2 (1800–2600Å , *top left*), UVM2 (2000–2800Å , *top right*) and UVW1 (2400–3600Å , *bottom*) filters. The central source and the spiral arms of the galaxy are clearly visible in all three filters. The nuclear source is brighter in the UV than the spiral arms

Filter	Wavelength (Å)	Flux (erg cm^{-2} s^{-1} $Å^{-1}$)
UVW1	2400-3600	2.58×10^{-14}
UVM2	2000-2800	2.42×10^{-14}
UVW2	1800-2600	2.31×10^{-14}

Table 5.1: Fluxes for the optical monitor UV filters. The data are corrected for Galactic extinction

A circle of radius 10" was used to extract the source and background count rates for each filter. Deadtime and coincidence losses were applied to the background subtracted count rates using the *XMM − Newton* users hand book. Count rates were converted to fluxes using the standard recipe[1] and corrected for Galactic extinction using the reddening law of Allen (1976) and E(B-V) = 0.08 (Edelson & Malkan 1986). For details see appendix B. The fluxes for the different UV filters are listed in Table 5.1.

5.2.2 Archival data

To study the overall energy output of NGC 4051 from the radio to X-rays, multi-wavelength data on the source were compiled from previous publications listed below:

The optical to IR data are from: Anderson 1970 (3×10^{14} Hz-10^{15} Hz), Takamiya et al 1995 (B, V), Done et al 1990 (U, B, I, J, H, K), Rieke et al 1972 (3.5μm, 5μm, 10μm), Moshir 1990 (IRAS data, 12μm, 25μm, 60μm, 100μm), Rodriguez et al. 1996 (ISO data, 16μm, 25μm, 60μm, 120μm, 135μm, 180μm, 200μm)

The radio data are taken from Gregory et al 1990 (4.85 GHz), Huchtmeier et al 1989 (1.42 GHz) and Ulvestad et al 1984 (1.46 GHz, 4.88 GHz).

[1] http://xmm.vilspa.esa.es/external/xmm_sw_cal/sas_frame.shtml

5.3 X-ray spectra

Spectral fitting of X-ray data was done using the XSPEC software package version 11.1. All emission line energies quoted in the text are in the observer frame (z = 0.0023, de Vaucouleurs et al. 1991) and errors are quoted at 90% confidence level ($\Delta\chi^2 = 2.7$ for one interesting parameter) unless specified otherwise.

5.3.1 The integrated spectrum

The integrated MOS and PN spectra over the entire 103 ks exposure were grouped to a minimum of 80 and 150 counts per bin respectively and fitted over an energy range of 0.3−10.0 keV while the RGS spectrum was fitted over an energy range of 0.3−2.0 keV. Spectra from the RGS and EPIC detectors of $XMM-Newton$ were fitted simultaneously during spectral analysis.

To begin with I fitted the 0.3−10.0 keV spectrum with a power-law and neutral absorption, both free to vary. This gives a photon index of $\Gamma = 2.37^{+0.06}_{-0.02}$ and $N_H < 1{\times}10^{20}$ cm^{-2} . The best fit neutral column density is less than the Galactic absorption measured in the direction of NGC 4051 ($N_H = 1.32{\times}10^{20}$ cm^{-2}) and henceforth I fix the neutral absorption to the Galactic value for all spectral fitting.

A power-law plus fixed Galactic absorption model fit to the data yields a photon index of $\Gamma = 2.513^{+0.003}_{-0.002}$ (χ^2/dof = 44713/2456, Fig 5.2). The resultant fit residuals are steep at E > 2.0 keV and show broad emission features around 0.6 keV and 6 keV along with an edge-like feature around 7.0 keV and a narrow neutral Fe K_α line at 6.4 keV, both potential signatures of reflection from neutral material. A prominent narrow [O VII] line is also observed at 0.56 keV (Fig 5.2). Based on the low state observations of NGC 4051 several authors have argued that the X-ray emission in NGC 4051 may include substantial contribution from distant neutral material, possibly a molecular torus (Uttley et al 1999, Guainazzi et al. 1998). The high resolution and signal to noise $XMM-Newton$ data allows us test this claim by measuring the energies of the alleged reflection features with much higher accuracy

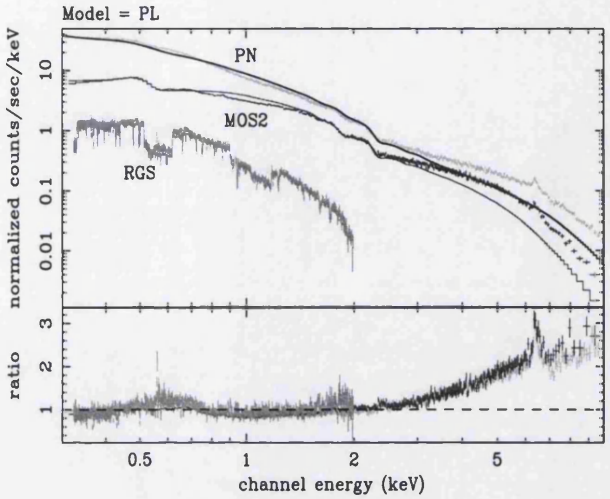

Figure 5.2: A simultaneous power-law fit to the RGS and EPIC spectra ($\Gamma = 2.513^{+0.003}_{-0.002}$). The neutral column density is fixed to the Galactic value of $N_H = 1.32 \times 10^{20}$ cm^{-2}.

than was previously possible. I find that the central energy of the narrow Fe K_α line is consistent with emission from neutral iron. However, the energy of the edge-like feature is $E_{edge} = 6.89^{+0.12}_{-0.14}$ keV, where the errors are 4σ, which is inconsistent with that of a neutral iron edge. The Fe K_α line and edge energies were obtained by fitting the 5−8 keV spectrum with a powerlaw plus a narrow Gaussian (6.4 keV) plus an edge model (χ^2/dof = 263/302). The upper limit on the optical depth for an edge at 7.1 keV is $\tau < 0.17$ which is consistent with that expected from reflection of neutral material (i.e. accretion disk) (George & Fabian 1991).

I check if a power-law plus reflection from an ionised accretion disk (using the PEXRIV model, which comprises of a power-law plus Compton reflection from ionised material) could describe the data better than a single power-law model. The inclination angle in the PEXRIV model used in this analysis has been constrained between 40°-60°. Ionised reflection is unable to reproduce the spectrum between 2−10 keV on its own. A large reflection fraction (R = 85±5) is required to match the observed spectral steepness (at E > 2.0 keV) and the resultant fit is extremely

poor.

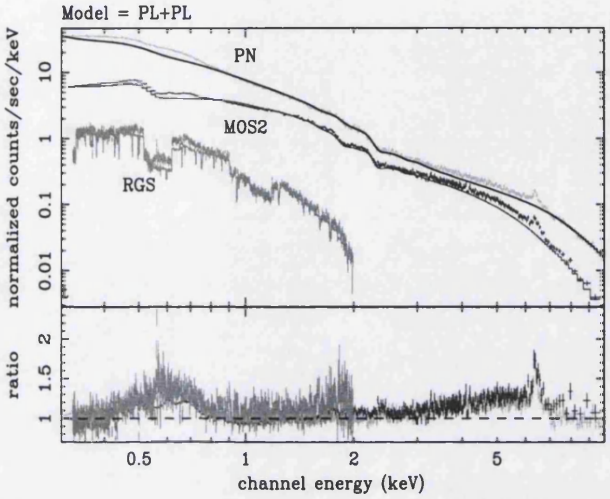

Figure 5.3: A simultaneous two power-law fit to the RGS, MOS2 and PN spectra (Γ_{soft}= $2.6^{+0.003}_{-0.002}$, Γ_{hard} = 1.07±0.01). The neutral column density is fixed to the Galactic value of N_H = 1.32×10^{20} cm^{-2}. The residuals show broad emission features around 0.6 keV and 6 keV along with narrow features at 0.56 keV and 6.4 keV.

A two power-law plus ionised reflection (R = $\Omega/2\pi$) model (model = PEXRIV+PL) is a better fit to the underlying 0.3−10.0 keV continuum. The model is able to account for the spectral steepening at E > 2 keV and only the broad and the narrow emission features are visible in the fit residuals (Fig 5.3). I note that the goodness of fit of a power-law plus blackbody model (Γ = 1.95±0.03, kT = 0.1±0.05) to the 0.3−10.0 keV data is comparable to that of the two power-law plus reflection model, however, the shape of the high resolution RGS spectrum is unlike that of a blackbody (Fig 5.4) . Additionally, the observed X-ray variability on time-scales down to 200 s in NGC 4051 makes a direct link between the soft X-ray emission and the intrinsic (optically thick) emission from the disk highly unlikely (see §5.4.2 for details) and we do not pursue this model any further.

Since the observed dip-like feature at 7 keV is not consistent with an iron absorption edge I consider the possibility that it may be the blue cut-off of a relativistically

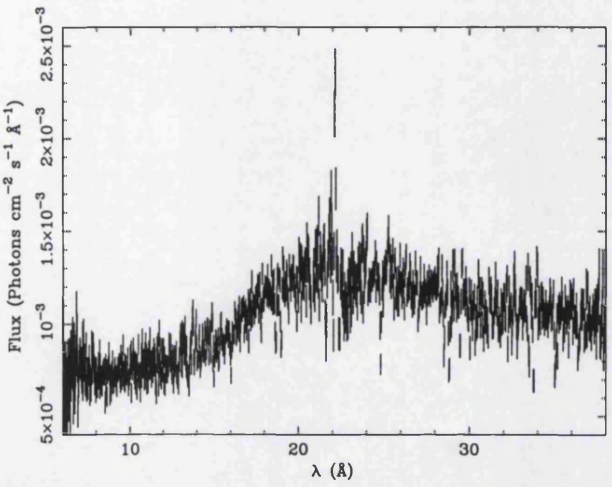

Figure 5.4: RGS spectrum of NGC 4051 showing the broad emission feature between 10−30 Å and a narrow [O VII] emission line.

broadened iron emission line and model the observed excess between 4−7 keV with an Fe K_α emission line profile from around a rotating black hole (which is found to be a significantly better fit ($\Delta\chi^2 = 52$ for 0 extra parameters) compared to a line profile from around a non-rotating black hole).

The broad emission feature seen in the EPIC spectra at soft X-ray energies is also unambiguously detected in the high resolution RGS spectrum (Fig 5.4). In fact this is the most prominent feature in the RGS spectrum and spans a wavelength range of 12Å−31Å. Broad emission features at low X-ray energies were first detected in the X-ray spectra of two narrow line Seyfert 1 galaxies, MRK 766 and MCG-6-30-15 and have been interpreted as relativistically broadened emission lines from the disk (Branduardi-Raymont et al. 2000) or as complex absorption (Lee et al. 2001). Although the controversy over the interpretation is still ongoing, recent studies show that over a broader spectral range the relativistic line model does provide a significantly better fit to the RGS data compared to the dusty warm absorber model (Sako et al. 2002, Mason et al. 2002). As such I model the soft X-ray feature

in NGC 4051 with a relativistic O VIII emission line from the surface of a photo-ionised disk.

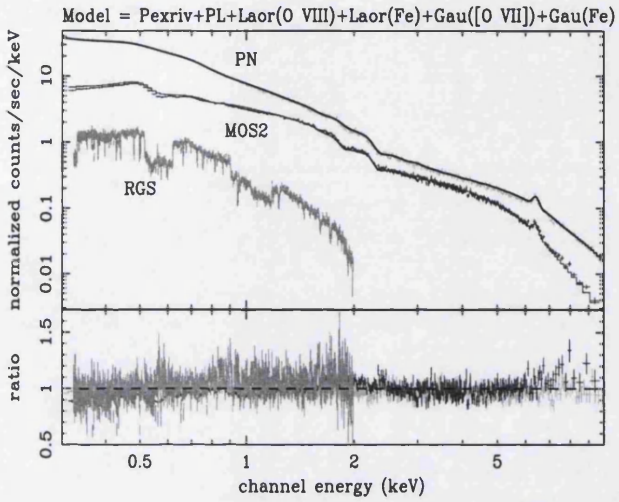

Figure 5.5: The PEXRIV(PL plus ionised reflection) + PL + 2Laor (O VIII, Fe) + 2gau (O VII, Fe) model fit to the integrated RGS and EPIC spectra. The neutral column density is fixed to the Galactic value of $N_H = 1.32 \times 10^{20}$ cm^{-2}. Although the fit residuals are reasonably distributed about the mean the fit statistics are unacceptable ($\chi^2/dof = 6757/2438$). See Table.5.2 for details.

The best fit model to the 0.3−10.0 keV spectrum of NGC 4051 consists of PEXRIV (which includes a power-law and a reflection component), a second power-law, a [O VII] narrow Gaussian, a O VIII Laor line, a Fe K_α Laor line and a Fe K_α narrow Gaussian line. The line energies of the narrow [O VII] and Fe K_α Gaussian emission lines and the broad O VIII Laor emission line are fixed to their redshifted values in the observers frame. The outer radius for both the O VIII and Fe K_α Laor emission lines is fixed at 400 R_g during spectral fitting. The resultant fit residuals do not show any obvious trend or bumps and are reasonably distributed about the mean (Fig 5.5). However, the overall fit statistics are high with χ^2/dof = 6757/2438. The fit parameters of the model fit to the 0.3−10.0 keV spectra are listed in Table 5.2 (note the similarity in the model line parameters of the O VIII and Fe K_α lines). Interestingly, the hard photon index measured during the *XMM − Newton*

observation (Γ = 1.05±0.01) is similar to that measured in the 10−18 keV ($\Gamma = 1.08^{+0.44}_{-0.38}$) energy range with *GINGA* (Nandra & Pounds 1994) and also to that in the 2−10 keV energy range ($\Gamma = 0.78^{+0.37}_{-0.13}$) with *BeppoSAX*, during the long low state of NGC 4051 when the variable X-ray source was seen to switch off for several weeks (Guainazzi et al. 1998).

Parameter	Best fit value		
Photon index (Γ_{hard})	$1.05^{+0.01}_{-0.01}$		
Photon index (Γ_{soft})	$2.61^{+0.004}_{-0.007}$		
	Fe K_α	Fe K_α	O VIII
	Laor	Gau	Laor
Line Energy (keV)	$6.46^{+0.62}_{-0.11}$	$6.41^{+0.04}_{-0.04}$	0.6522^f
Index (q)/σ (keV)	$7.67^{+1.38}_{-0.42}$	$0.12^{+0.04}_{-0.08}$	$6.22^{+0.17}_{-0.11}$
Inner radius (R_{in})	$1.24^{+0.1}_{-0}$ R_g	-	$1.56^{+0.09}_{-0.27}$ R_g
Outer radius (R_{out})	400^f R_g	-	400^f R_g
Inclination (i)	$53°^{+6}_{-5}$	-	$57°^{+12}_{-2}$
EW (eV)	810^{+65}_{-128}	130^{+45}_{-27}	70^{+6}_{-5}
Flux*	2.14×10^{-12}	2.24×10^{-13}	2.82×10^{-12}
χ^2/dof	6757/2438		

* erg cm^{-2} s^{-1}

^{f} fixed

Table 5.2: Best fit model parameters for the 0.3−10.0 keV integrated spectrum over the 103 ks exposure of NGC 4051 (see Fig 5.5).

One possible reason for the observed complexity in the 0.3−10.0 keV spectra and the high reduced χ^2 value could be that the various features observed in the 0.3−10.0 keV spectrum are not static over the 103 ks period, but are variable.

In such a case the time averaged spectrum would be a combination of several different spectra superimposed on each other. If there are significant changes in the X-ray spectrum over time they would be reflected in the ratio of flux in different energy bands. Fig 5.6 shows the hardness ratio curve for the 0.1−2 keV and 2−10 keV X-ray emission in NGC 4051. Complex variations in the ratio of the hard and soft photons are observed including a significantly harder spectrum when the flux in both the bands is dramatically reduced. The changing hardness ratio shows that significant spectral variability takes place over the 103 ks observation in NGC 4051. The spectral variability could be responsible for the unacceptable reduced χ^2 values obtained for the best fit model to the integrated 0.3−10 keV spectrum.

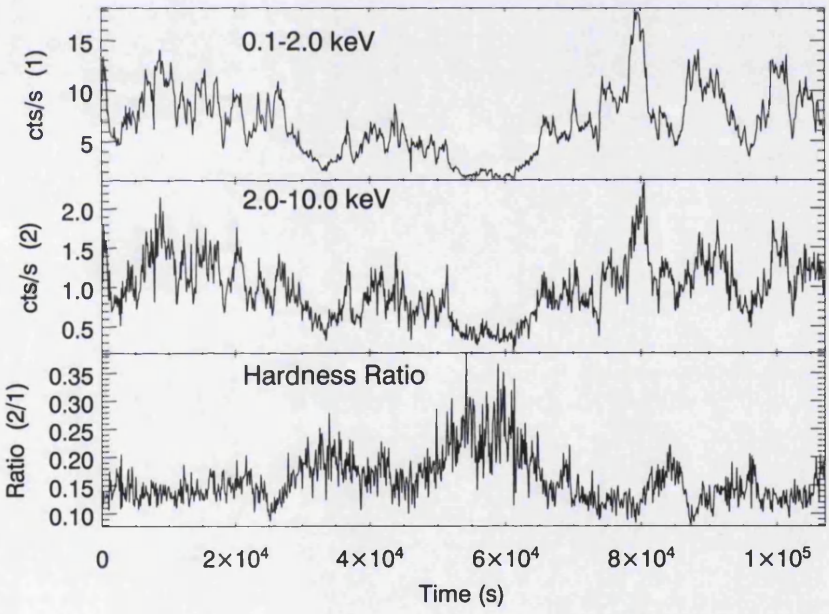

Figure 5.6: The hardness ratio plot for NGC 4051. Complex variations in the ratio of the hard and soft photons are observed including a significantly harder spectrum when the flux in both the bands is dramatically reduced.

5.3.2 Time resolved spectroscopy

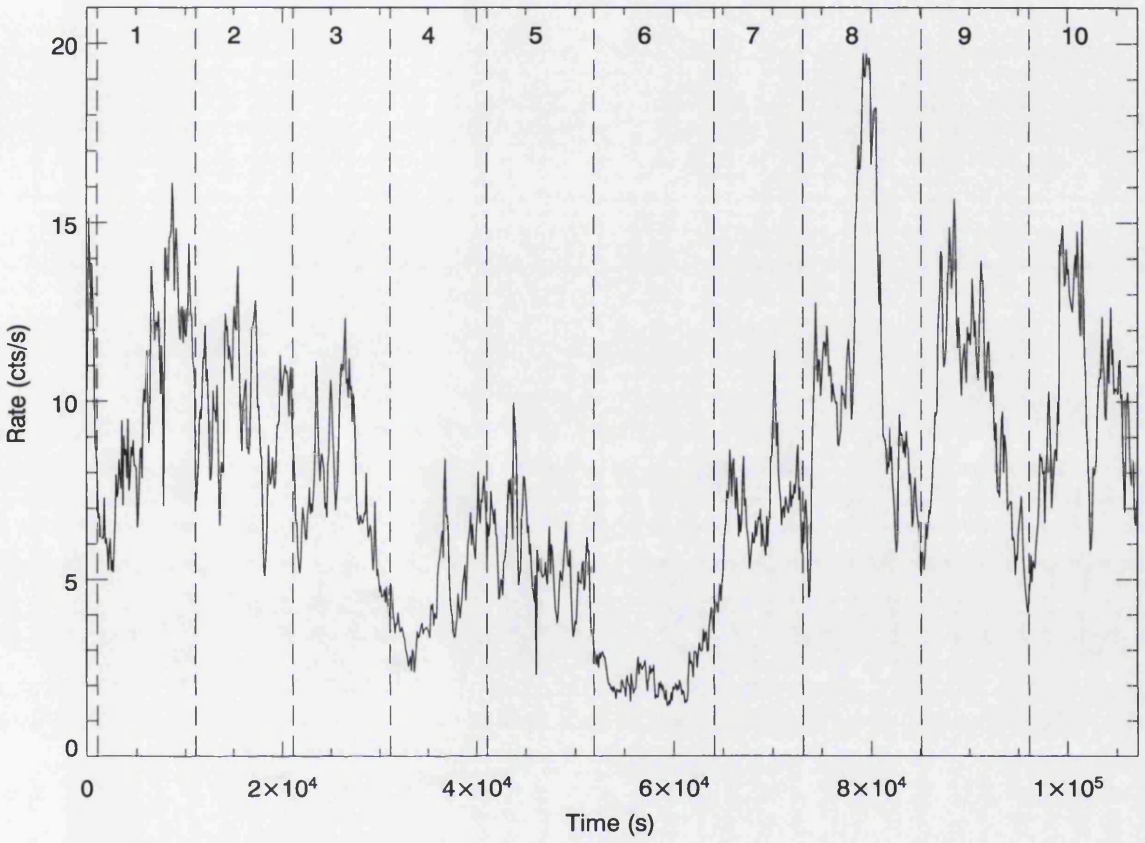

Figure 5.7: The 103 ks light curve (0.1−10.0 keV) of NGC 4051. The dashed lines show the different time intervals during which spectra were extracted for the spectral variability analysis

To study the spectral variability of NGC 4051 I divided the 103 ks observation into 10 approximately 10 ks intervals (see Fig. 5.7). The time intervals were selected in such a way that the minimum flux epochs and the individual flaring events could be isolated as far as possible. This allows the study of spectral properties as the count-rate of the source varies. The spectra extracted from each of the 10 time intervals will be referred to as time resolved spectra from now on. The ratio of the time resolved EPIC spectra to a single power-law ($\Gamma = 2.5 \pm 0.05$) model fit to the minimum flux epoch (interval 6) spectrum is shown in Fig 5.8.

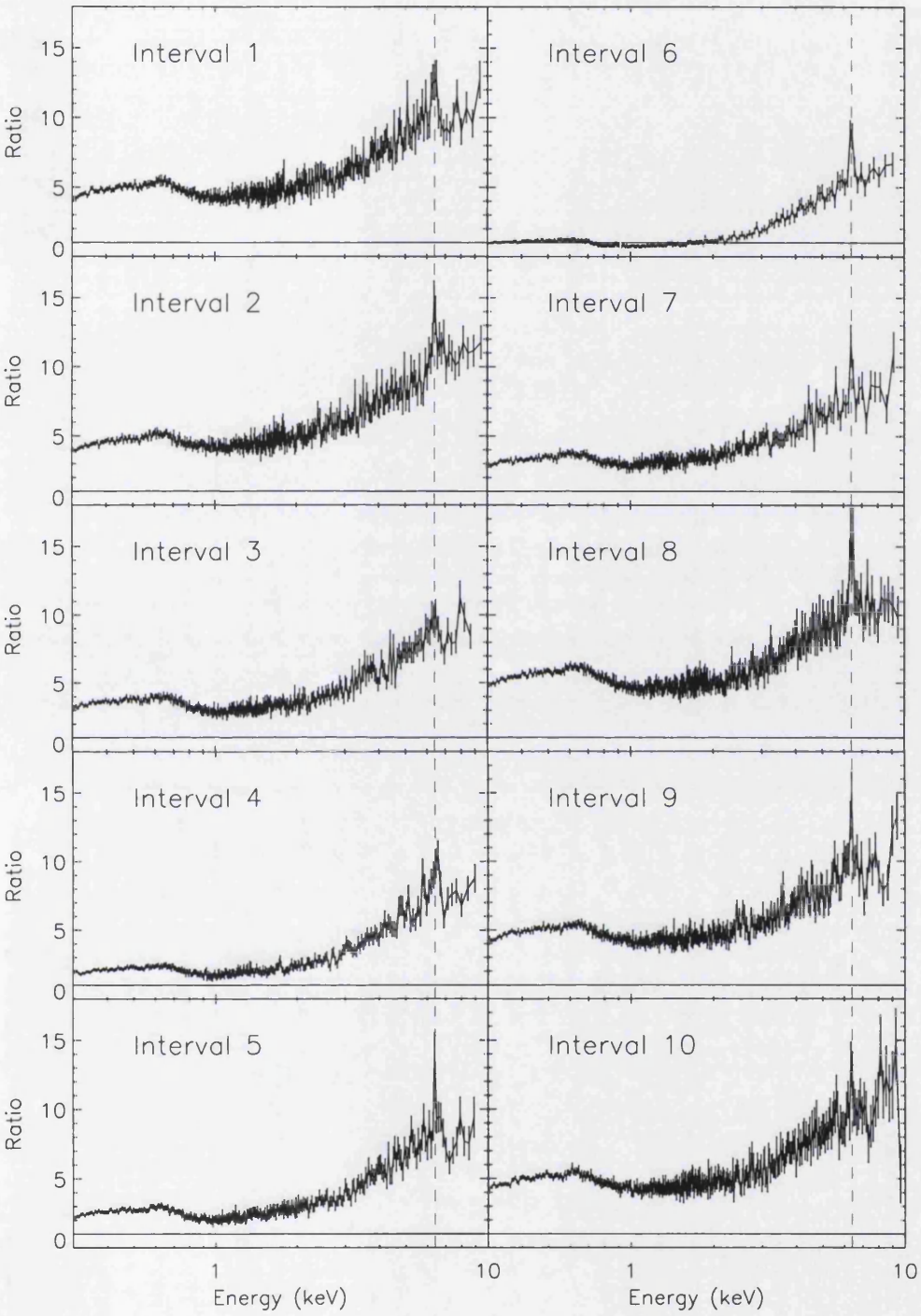

Figure 5.8: The plot shows the ratio of the time resolved EPIC spectra to a single power-law (Γ = 2.5) model fit to the minimum flux epoch (interval 6) spectrum. The position of the 6.4 keV line is indicated by the dashed line.

In order to understand how the spectral components varied over time and also with respect to each other I fit the EPIC and RGS time resolved spectra simultaneously over the entire 0.3−10.0 keV range with the same best fit model discussed earlier (model = PEXRIV + PL + Laor (O VIII) + Laor (Fe) + Gau ([O VII]) + Gau (Fe)).

			Fe K_α				O VIII*			
Time bins	Γ_{hard}	Γ_{soft}	E (keV)	Index (q)	R_{in} (R_g)	Incl	Index (q)	R_{in} (R_g)	Incl	χ^2/dof
cut 1	$0.98^{+0.06}_{-0.01}$	$2.54^{+0.01}_{-0.01}$	$6.50^{+0.17}_{-0.18}$	$8.08^{+0.92}_{-0.68}$	$1.235^{+0.06}_{-0.0}$	53^{+4}_{-9}	$6.00^{+0.2}_{-0.2}$	$1.60^{+0.05}_{-0.07}$	55^{+1}_{-1}	1579/1088
cut 2	$1.05^{+0.01}_{-0.01}$	$2.52^{+0.01}_{-0.01}$	$6.62^{+0.38}_{-0.22}$	$8.51^{+1.49}_{-1.21}$	$1.24^{+0.05}_{-0.0}$	53^{+5}_{-8}	$5.86^{+0.24}_{-0.26}$	$1.67^{+0.07}_{-0.05}$	53^{+2}_{-1}	1410/1093
cut 3	$1.00^{+0.01}_{-0.01}$	$2.50^{+0.01}_{-0.01}$	$6.31^{+0.19}_{-0.21}$	$7.10^{+1.40}_{-1.00}$	$1.28^{+0.04}_{-0.0}$	54^{+7}_{-8}	$6.61^{+0.19}_{-0.21}$	$1.51^{+0.05}_{-0.03}$	59^{+2}_{-3}	1284/1025
cut 4	$1.00^{+0.03}_{-0.02}$	$2.50^{+0.01}_{-0.01}$	$6.55^{+0.35}_{-0.25}$	$7.74^{+1.96}_{-1.64}$	$1.34^{+0.03}_{-0.08}$	54^{+8}_{-6}	$6.92^{+0.28}_{-0.22}$	$1.52^{+0.09}_{-0.06}$	59^{+1}_{-4}	999/1052
cut 5	$1.00^{+0.01}_{-0.01}$	$2.61^{+0.01}_{-0.01}$	$6.46^{+0.26}_{-0.44}$	$8.10^{+1.80}_{-1.90}$	$1.24^{+0.06}_{-0.0}$	52^{+4}_{-14}	$6.52^{+0.08}_{-0.22}$	$1.47^{+0.07}_{-0.04}$	55^{+2}_{-1}	1295/1112
cut 6	$1.05^{+0.01}_{-0.01}$	$3.07^{+0.01}_{-0.01}$	$6.49^{+0.21}_{-0.17}$	$6.34^{+1.16}_{-0.54}$	$1.24^{+0.03}_{-0.0}$	49^{+5}_{-9}	$4.95^{+0.25}_{-0.25}$	$1.68^{+0.09}_{-0.06}$	48^{+5}_{-1}	844/943
cut 7	$1.11^{+0.01}_{-0.02}$	$2.56^{+0.01}_{-0.01}$	$6.42^{+0.21}_{-0.37}$	$9.53^{+0.47}_{-1.53}$	$1.24^{+0.02}_{-0.0}$	55^{+4}_{-6}	$6.45^{+0.25}_{-0.25}$	$1.55^{+0.05}_{-0.05}$	57^{+1}_{-2}	1181/1101
cut 8	$1.05^{+0.01}_{-0.01}$	$2.60^{+0.01}_{-0.01}$	$6.60^{+0.36}_{-0.72}$	$7.68^{+2.32}_{-1.18}$	$1.24^{+0.06}_{-0.0}$	58^{+8}_{-12}	$6.27^{+0.33}_{-0.17}$	$1.56^{+0.04}_{-0.07}$	59^{+1}_{-2}	1745/1154
cut 9	$1.02^{+0.04}_{-0.04}$	$2.57^{+0.01}_{-0.01}$	$6.84^{+0.16}_{-0.14}$	$8.58^{+0.92}_{-0.78}$	$1.24^{+0.06}_{-0.0}$	57^{+3}_{-1}	$6.99^{+0.21}_{-0.29}$	$1.53^{+0.03}_{-0.06}$	59^{+1}_{-1}	1706/1106
cut 10	$1.05^{+0.02}_{-0.04}$	$2.57^{+0.01}_{-0.01}$	$6.40^{+0.20}_{-0.4}$	$7.40^{+0.60}_{-1.3}$	$1.37^{+0.03}_{-0.08}$	57^{+4}_{-10}	$6.66^{+0.24}_{-0.16}$	$1.53^{+0.03}_{-0.07}$	58^{+1}_{-1}	1543/1123

Notes: * Energy fixed the rest frame value

Table 5.3: The parameters of the model fit (PL, Pexriv (PL+reflection), 2 Laors and 2 narrow Gaussian (Fe, [O VII])) to the 0.3−10.0 keV spectra of NGC 4051 during different time intervals (see Fig 5.7). The [O VII] and Fe Gaussian line energy is fixed to its redshifted value in the observers frame. The [O VII] narrow line width is fixed to 0 keV. The Galactic column is fixed at $N_H = 1.32 \times 10^{20}$ cm^{-2} for all spectral fits.

The relativistic O VIII and Fe K_α lines and the narrow [O VII] and Fe K_α lines are detected at a significance of $> 3\sigma$ level in all ten spectra. Model fitting to the 0.3−10.0 keV spectrum (Table 5.3) reveals large amplitude related variations *only* in the soft powerlaw flux and the O VIII line flux (Fig 5.9). Despite large variations in the soft powerlaw flux, the soft photon index is relatively stable within a narrow range ($\Gamma_{soft} = 2.5-2.6$), except for the anomalous steepening ($\Gamma_{soft} = 3.0^{+0.01}_{-0.01}$) observed during the minimum flux epoch (interval 6, Fig 5.9).

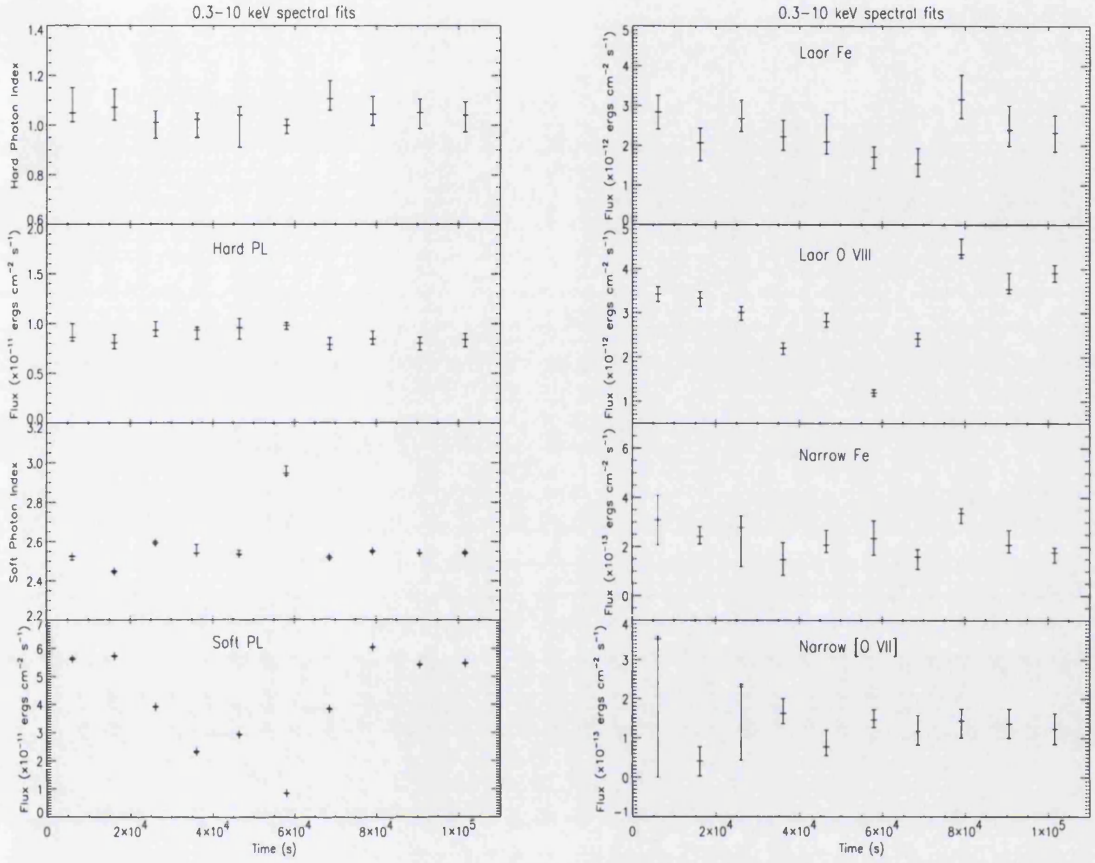

Figure 5.9: Time resolved spectral analysis results of the 0.3–10.0 keV range. *Left* : The hard powerlaw flux and photon index do not show any significant variations. The soft powerlaw component shows large variations in flux. The photon index varies over a narrow range (2.5–2.6) for most of the observation but a steepening of the index is observed during the minimum flux. *Right* : The relativistic Fe K_α line flux does not vary significantly except maybe during the end of the observation. The relativistic O VIII line flux varies significantly and is correlated with the soft powerlaw flux. The flux in the narrow Fe K_α and the [O VII] lines does not show any significant flux variations.

Despite the large amplitude flux variations in the soft X-ray components (powerlaw and O VIII emission line) the hard powerlaw flux and photon index do not display any significant flux variations and are almost unvarying over the entire 103 ks observation. The flux in the relativistic and narrow Fe K_α lines, is also found to be unvarying except for a possible small increase in flux (simultaneous with a

large increase in soft powerlaw flux) in the relativistic Fe K_α line towards the end of the observation (interval 8). The flux and EW of the narrow [O VII] is steady with time. This is consistent with the line originating in a low density gas, a large distance away from the variable central source (see Fig 5.9).

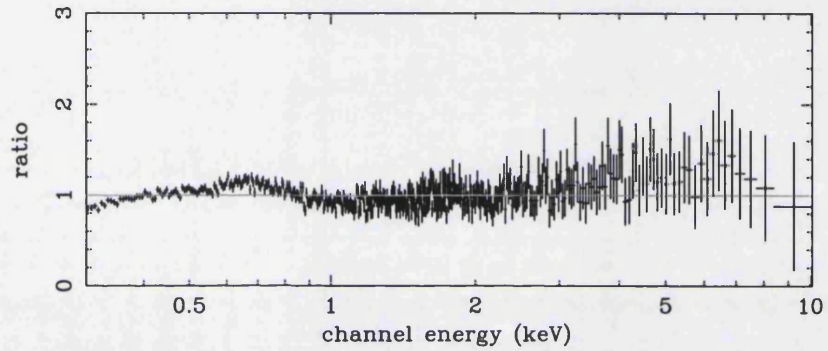

Figure 5.10: The ratio of a powerlaw model fit ($\Gamma = 2.5\pm0.05$) to the spectrum obtained by subtracting the low flux spectrum (interval 6) from the highest flux spectrum (interval 8). The fit residuals show no features at E > 2 keV (Compare with Fig 5.2) and only a broad excess is visible around 0.6 keV.

To check if the spectral components at E > 2 keV are indeed constant as indicated by the model fits I subtracted the low flux spectrum (interval 6) from the highest flux spectrum (interval 8). A single powerlaw fit to the subtracted spectrum yields a photon index of $\Gamma = 2.5\pm0.05$, consistent with the soft powerlaw index. The ratio of data to model is shown in Fig 5.10. The fit residuals show no features at E > 2 keV (compare with Fig 5.2) and only a broad excess is visible around 0.6 keV. The subtraction of the low flux spectrum from the high flux spectrum seems to have left behind just the soft powerlaw and the O VIII line indicating that there is no change in the hard spectral components (powerlaw, broad and narrow Fe lines) as the source brightens, which is consistent with spectral fitting results.

Spectral modeling over the hard and soft bands

Due to the limited energy range of previous detectors, AGN spectra have largely been studied in different energy bands, the so-called hard (E > 2 keV) and soft (E < 2 keV) bands. To investigate if (and how) the choice of energy range affects the spectral analysis results I also model the time resolved spectra in the soft and hard bands.

The 0.3−2 keV spectra of NGC 4051 are modeled using a powerlaw plus a Laor (O VIII) emission line. Results of the soft band spectral analysis reveal related large amplitude variations in the soft powerlaw flux and the O VIII line flux which is in agreement with the temporal behaviour of the soft powerlaw and O VIII line flux inferred from the 0.3−10 keV spectral analysis (see Fig. 5.11). However, the soft band analysis also shows variations in the soft photon index as the soft powerlaw brightens and fades which is contrary to the results of the 0.3−10 keV spectral analysis where the soft photon index is not seen to respond in a related manner to the soft powerlaw flux. The resultant fit parameters for the soft band are listed in Table. 5.4. The reduced χ^2 values are high (especially for the higher flux spectra) mainly due to the low level spectral complexity (i.e. narrow features, especially in the RGS spectrum) which have not been modeled.

The 2−10 keV spectra of NGC 4051 are modeled using a powerlaw plus ionised reflection (PEXRIV), a Fe Laor line and a Fe Gaussian line (Table 5.5). Results of the 2−10 keV spectral analysis show high amplitude related variations in the hard powerlaw flux and photon index (similar to the variations in the soft powerlaw flux observed in the 0.3−2 keV energy range), a behaviour totally different to that inferred from the results of the 0.3−10 keV spectral analysis where the hard photon index and flux are seen to be almost unvarying. The photon indices measured in the hard band are now softer and vary between $\Gamma = 1.7-2.0$ (a range typically observed in Seyfert 1 galaxies (Nandra & Pounds 1994), except during the low state (interval 6) where a hard index of $\Gamma \approx 1$ is measured (see Fig 5.11). The behaviour of the

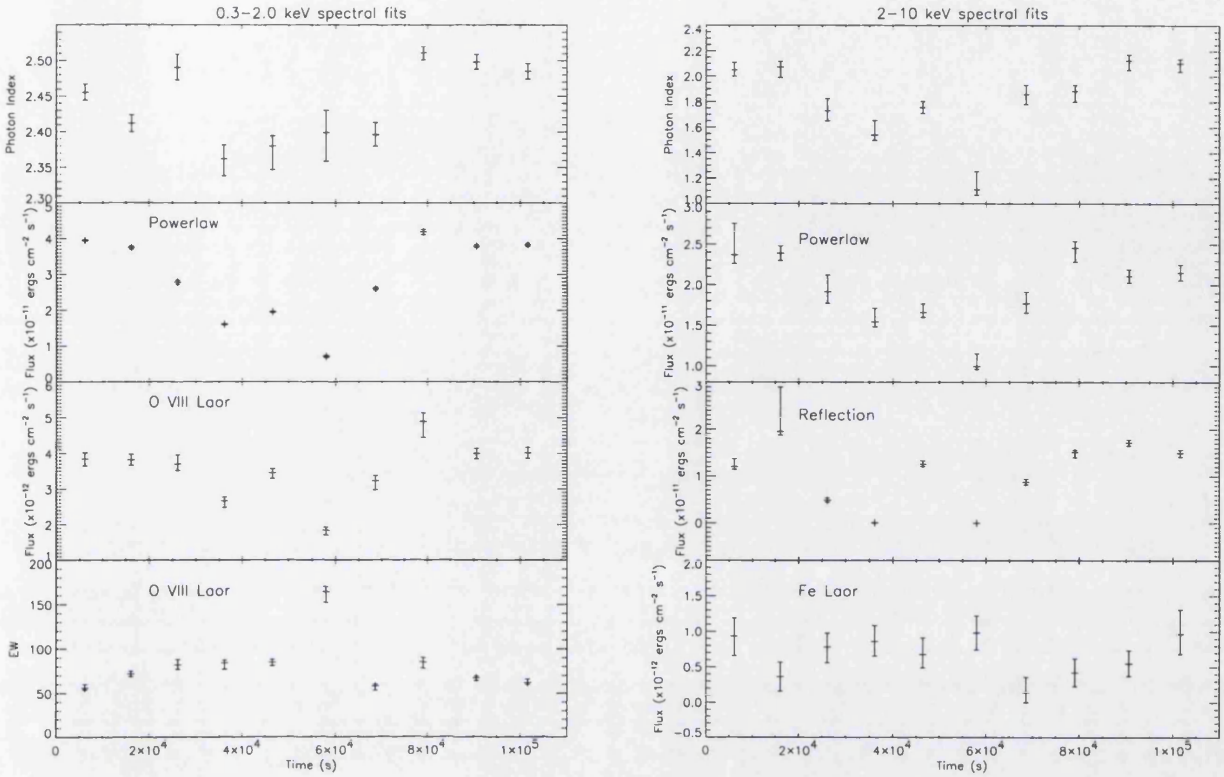

Figure 5.11: *Left* : Time resolved spectral analysis results for the 0.3−2.0 keV range. Related variations are observed between the soft PL flux, the photon index and the O VIII Laor line flux. *Right* : Time resolved spectral analysis results over the 2.0−10.0 keV range. Related variations are observed between the PL flux, the photon index and the reflection flux. The iron line flux is relatively unvarying.

Fe K_α emission lines (both broad and narrow) over time is however, not affected by the choice of energy range.

The temporal behaviour of the hard power-law flux and the soft and hard photon indices inferred from spectral analysis of the individual energy bands (0.3−2 keV , 2−10 keV) differs widely from that inferred from the wider 0.3−10.0 keV band analysis. The reason for this observed inconsistency is discussed in §5.4.1. The resultant fit parameters for the hard band are listed in Table 5.5.

Time bins	Γ	Energy (keV)	emissivity (q)	EW (O VIII) (eV)	χ^2/dof
Cut 1	$2.45^{+0.01}_{-0.06}$	0.65^f	5.86±0.52	56^{+4}_{-2}	1483/894
Cut 2	$2.41^{+0.01}_{-0.01}$	0.65^f	7.65±0.81	73^{+2}_{-4}	1193/884
Cut 3	$2.49^{+0.01}_{-0.02}$	0.65^f	7.07±0.69	82^{+6}_{-5}	1230/854
Cut 4	$2.36^{+0.02}_{-0.02}$	0.65^f	6.56±0.60	84^{+3}_{-7}	1230/854
Cut 5	$2.38^{+0.01}_{-0.03}$	0.65^f	6.46±0.54	86^{+2}_{-5}	1218/876
Cut 6	$2.40^{+0.03}_{-0.04}$	0.65^f	6.83±0.87	165^{+5}_{-13}	852/787
Cut 7	$2.40^{+0.01}_{-0.02}$	0.65^f	6.97±0.79	58^{+2}_{-6}	1005/882
Cut 8	$2.51^{+0.01}_{-0.01}$	0.65^f	8.64±0.49	86^{+4}_{-8}	1452/904
Cut 9	$2.50^{+0.01}_{-0.01}$	0.65^f	9.06±0.60	67^{+2}_{-3}	1434/888
Cut 10	$2.48^{+0.02}_{-0.01}$	0.65^f	8.42±0.64	63^{+3}_{-3}	1434/888

Notes : ^{f} Fixed

Table 5.4: The parameters of the model fit (PL+Laor) to the 0.3−2.0 keV spectra of NGC 4051 during different time intervals (see Fig 5.7). The O VIII Laor line energy is fixed to its redshifted value in the observers frame. The Galactic column is fixed at $N_H = 1.32 \times 10^{20}$ cm^{-2} for all spectral fits. The reduced χ^2 values are high (especially for the higher flux spectra) mainly due to the low level spectral complexity (i.e. narrow features especially in the RGS spectrum) which have not been modeled.

Time bins	Γ	Refl fraction	Energy (keV)	emissivity (q)	EW (Fe_{Laor}) (eV)	Energy (keV)	EW (Fe_{gau}) (eV)	χ^2/dof
Cut 1	$2.08^{+0.05}_{-0.06}$	$0.79^{+0.84}_{-0.63}$	$6.38^{+0.72}_{-1.18}$	$3.75^{+0.91}_{-0.58}$	352^{+96}_{-104}	6.4^f	76^{+60}_{-13}	175/192
Cut 2	$2.07^{+0.04}_{-0.08}$	$1.00^{+1.00}_{-0.73}$	$6.44^{+0.88}_{-1.11}$	$9.99^{+0.01}_{-7.33}$	162^{+91}_{-92}	6.4^f	71^{+35}_{-31}	196/198
Cut 3	$1.73^{+0.10}_{-0.08}$	$0.56^{+1.24}_{-0.56}$	$6.49^{+0.71}_{-0.59}$	$3.37^{+1.24}_{-0.44}$	393^{+98}_{-111}	6.4^f	60^{+26}_{-38}	155/158
Cut 4	$1.54^{+0.11}_{-0.04}$	$0.004^{+0.08}_{-0.004}$	$6.46^{+0.48}_{-0.39}$	$3.20^{+0.95}_{-0.37}$	561^{+141}_{-133}	6.4^f	48^{+33}_{-33}	187/187
Cut 5	$1.75^{+0.05}_{-0.05}$	$1.00^{+0.96}_{-0.57}$	$6.88^{+0.94}_{-1.02}$	$4.84^{+5.16}_{-1.49}$	290^{+99}_{-80}	6.4^f	95^{+62}_{-33}	229/231
Cut 6	$1.11^{+0.14}_{-0.04}$	$0^{+2.00}_{-0}$	$6.69^{+1.09}_{-0.71}$	$4.09^{+1.78}_{-0.40}$	830^{+200}_{-198}	6.4^f	137^{+40}_{-39}	152/143
Cut 7	$1.86^{+0.07}_{-0.08}$	$0.69^{+1.18}_{-0}$	6.00^u	4.09^u	85^{+130}_{-82}	6.4^f	82^{+40}_{-42}	218/207
Cut 8	$1.88^{+0.05}_{-0.08}$	$0.92^{+0.83}_{-0.92}$	$6.65^{+0.35}_{-0.77}$	$2.65^{+1.85}_{-1.48}$	177^{+81}_{-82}	6.4^f	62^{+25}_{-27}	211/244
Cut 9	$2.12^{+0.05}_{-0.07}$	$1.00^{+1.00}_{-0.71}$	$6.29^{+0.19}_{-0.29}$	$2.73^{+3.69}_{-1.24}$	248^{+84}_{-80}	6.4^f	71^{+32}_{-33}	234/206
Cut 10	$2.10^{+0.04}_{-0.06}$	$1.00^{+1.00}_{-0.44}$	$6.58^{+1.08}_{-0.75}$	$3.65^{+0.85}_{-0.65}$	441^{+145}_{-131}	6.4^f	44^{+34}_{-32}	220/220

Notes : ^{u} Unconstrained
^{f} Fixed

Table 5.5: The parameters of the best fit model (PEXRIV+Laor+gau) to the 2.0−10.0 keV spectra of NGC 4051 during different time intervals (see Fig 5.7). The line energy of the narrow Gaussian is fixed to 6.4 keV. The outer radius of the Laor line is fixed to 400 *Rg*. The Galactic column is fixed at $N_H = 1.32 \times 10^{20}$ cm^{-2} for all spectral fits.

					HB		Fe (Gau)	[OVII] (Gau)	
Time bins	Γ_{hard}	Γ_{soft}	F_s/F_d	Rate[a] $\times 10^{-4}$	R_{in} R_g	R_{out} R_g	EW (eV)	EW (eV)	χ^2/dof
cut 1	$1.15^{+0.10}_{-0.07}$	$2.50^{+0.01}_{-0.01}$	$0.80^{+0.09}_{-0.05}$	$7.3^{+2.5}_{-1.2}$	$2.77^{+0.20}_{-0.30}$	307^{+36}_{-53}	67^{+34}_{-20}	3^{+8}_{-2}	1725/1089
cut 2	$1.14^{+0.07}_{-0.09}$	$2.43^{+0.01}_{-0.01}$	$0.32^{+0.02}_{-0.07}$	$6.1^{+2.9}_{-4.8}$	$2.5^{+0.20}_{-0.10}$	11^{+3}_{-2}	69^{+30}_{-27}	1^{+1}_{-1}	1488/1094
cut 3	$1.03^{+0.05}_{-0.06}$	$2.59^{+0.01}_{-0.01}$	$0.50^{+0.02}_{-0.05}$	$3.3^{+7.5}_{-7.4}$	$2.74^{+0.10}_{-0.30}$	85^{+60}_{-22}	59^{+44}_{-33}	4^{+1}_{-3}	1579/1020
cut 4	$1.00^{+0.03}_{-0.07}$	$2.54^{+0.04}_{-0.01}$	$0.38^{+0.02}_{-0.03}$	$6.6^{+2.6}_{-1.2}$	$2.9^{+0.20}_{-0.40}$	21^{+2}_{-1}	70^{+38}_{-44}	8^{+1}_{-1}	1301/1048
cut 5	$1.00^{+0.03}_{-0.13}$	$2.53^{+0.02}_{-0.01}$	$0.37^{+0.03}_{-0.03}$	$4.0^{+0.8}_{-0.5}$	$3.00^{+0.10}_{-0.02}$	$9^{+1}_{-0.2}$	68^{+49}_{-20}	3^{+2}_{-1}	1658/1113
cut 6	$1.00^{+0.02}_{-0.03}$	$2.94^{+0.03}_{-0.02}$	$0.77^{+0.03}_{-0.04}$	$4.1^{+3.3}_{-1.3}$	$2.70^{+0.20}_{-0.30}$	76^{+230}_{-33}	144^{+47}_{-43}	15^{+2}_{-2}	1126/943
cut 7	$1.05^{+0.07}_{-0.05}$	$2.51^{+0.01}_{-0.01}$	$0.52^{+0.03}_{-0.17}$	$5.7^{+7.0}_{-4.4}$	$2.52^{+0.30}_{-0.20}$	28^{+14}_{-2}	54^{+44}_{-10}	6^{+1}_{-1}	1315/1102
cut 8	$1.01^{+0.08}_{-0.04}$	$2.54^{+0.01}_{-0.01}$	$0.63^{+0.01}_{-0.05}$	$8.3^{+1.0}_{-1.0}$	$2.33^{+0.40}_{-0.01}$	301^{+103}_{-42}	98^{+35}_{-41}	3^{+1}_{-1}	1841/1128
cut 9	$1.03^{+0.05}_{-0.06}$	$2.54^{+0.01}_{-0.01}$	$0.53^{+0.03}_{-0.06}$	$1.1^{+12.9}_{-12.9}$	$2.83^{+0.30}_{-0.08}$	144^{+114}_{-34}	68^{+38}_{-11}	3^{+1}_{-1}	1827/1101
cut 10	$1.01^{+0.05}_{-0.07}$	$2.54^{+0.01}_{-0.01}$	$0.50^{+0.08}_{-0.08}$	$8.8^{+8.8}_{-8.2}$	$3.00^{+0.10}_{-0.30}$	92^{+12}_{-27}	46^{+33}_{-5}	3^{+1}_{-1}	1652/1123

Notes: [a] Accretion rate in Eddington units

Table 5.6: The parameters of the model fit (2 PL, reflection and 2 narrow Gaussian (Fe, [O VII])) to the 0.3−10.0 keV spectra of NGC 4051 during different time intervals (see Fig.5.7). The [O VII] and Fe Gaussian line energy is fixed to its redshifted value in the observers frame. The [O VII] narrow line width is fixed to 0 keV. The Galactic column is fixed at $N_H = 1.32 \times 10^{20}$ cm^{-2} for all spectral fits.

Is reflection from an ionised disk the answer?

In my spectral analysis so far, I have modelled the observed excess between 0.5−0.8 keV and between 5−7 keV each with a 'Laor' emission line model. Although this is statistically the best fit model to the data, it is a phenomenological one. The model reproduces a line profile from around a rotating black hole but provides no answers to the the physical processes that could produce such emission lines. Since the most likely origin of relativistic lines in X-ray spectra is the surface of an accretion disk, I check if a hydrostatic balance (HB) reflection model (Nayakshin et al. 2001) incorporating both Compton reflection and re-processing by the disk in a self consistent manner could reproduce the observed data. I fitted each time resolved spectrum over the 0.3−10.0 keV range with a model consisting of two power-laws,

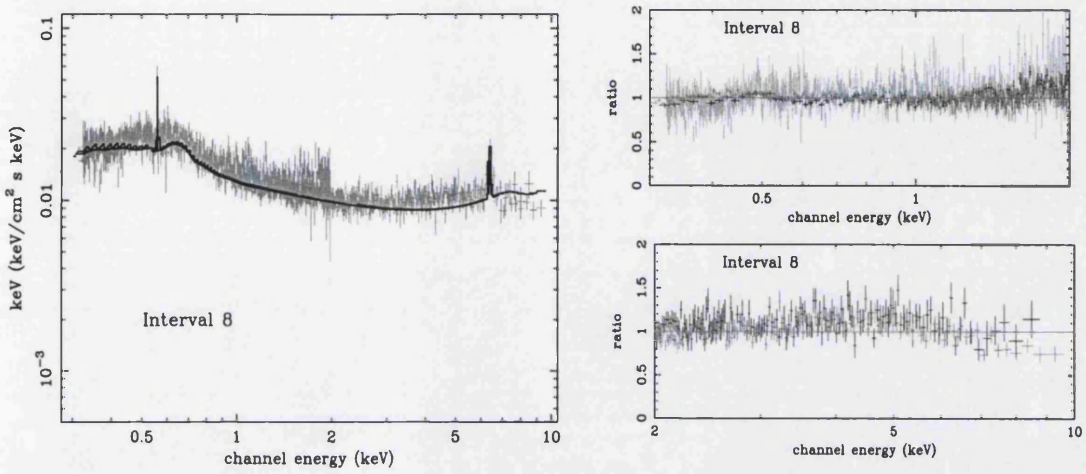

Figure 5.12: *Left* : Unfolded spectrum showing the 2 PL, 2 Gaussian ([O VII], Fe K_α) plus hydrostatic balance reflection model fit model fit to the spectrum from highest flux epoch (interval 8). The reflection model reproduces the low and high energy excess with a broad O VIII line and an neutral Fe K_α line respectively. However, the resultant fit residuals show a subtle curvature between 0.45−0.55 keV (*top right* panel) and 3−5 keV (*bottom right* panel) which could be the red tail of the Fe K_α line profile, that the reflection model has not been able to account for (as it includes relativistic smearing for a spectrum around a non-rotating black hole and not for a rotating black hole).

a fixed Galactic neutral absorption, two narrow Gaussian (Fe, [O VII]) and the HB reflection model. The inclination angle in the HB model is constrained between 40°-60°. I find that the magnetic flare geometry of the model (in which the X-ray sources lie close to the disk surface and illuminate the disk surface unevenly) is a better fit to the data ($\Delta\chi^2 = 681$ for 0 extra parameter) compared to the lamppost geometry (in which a point-like X-ray source from above illuminates a large area of the disk) which produces soft X-ray features that are too weak to describe the data satisfactorily (see Nayakshin et al. 2000).

The power-law indices of the best fit model in the soft range are found to be steep ($\Gamma = 2.5-2.6$), while those in the hard band are flat ($\Gamma \approx 1$). As found previously, the soft power-law flux is highly variable while the hard power-law flux is almost unvarying. The reflection (HB) model reproduces the high energy excess with a broad neutral Fe K_α line and the excess at low X-ray energies with a broad O VIII line. However, the resultant fit residuals show a subtle curvature between 3–5 keV and 0.45–0.55 keV which could be the red tail of the Fe K_α line profile and the O VIII line respectively, that the reflection model has not been able to account for (as it includes relativistic smearing for a spectrum around a non-rotating black hole and not for a rotating black hole). In addition to the O VIII line the model also produces a O VII line (maybe in an attempt to account for the red wing of the H-like oxygen line) and a C VI line which become almost indistinguishable from the continuum when the relativistic smearing is applied. The best fit model parameters for the 0.3–10.0 keV band are listed in Table. 5.6. It should be noted that the model used has a different continuum (i.e. a single powerlaw) to that fitted. A double powerlaw continuum will change the temperature profile and as such the ionisation balance of the upper layers of the disk and may mean one cannot simultaneously fit the O VIII and Fe lines together.

5.4 Discussion

5.4.1 Choice of energy range and its effect on spectral modelling results

The limited bandwidth and/or energy resolution of previous detectors made it very difficult to model or study the behaviour of both soft and hard X-ray components in AGN simultaneously. Hence X-ray data were generally studied in separate energy bands with the implicit assumption that the soft component, if present, did not contribute significantly to energies beyond 1−2 keV and the emission upwards of 2 keV is representative of the primary power-law X-ray emission in AGN. Spectral analysis results over a wider energy range using *BBRXT* and simultaneous *ROSAT* and *GINGA* observations in the early nineties suggested that the soft component (modeled as a black body) did not generally contaminate data above 2 keV (Turner et al. 1993, Pounds et al. 1994, Mushotzky 1993) and appeared to support the above assumption.

If a black body is a correct interpretation of the steep emission below 2 keV in AGN and if the X-ray emission at E > 2 keV does not contain any significant contribution from the low energy component (E < 2) then the spectral parameters derived for the hard power-law component in this energy range should not be significantly affected by the inclusion of lower energy data. However, the results of this study have shown otherwise. Spectral analysis over 0.3−10.0 keV range shows the hard power-law component to be steady in flux and photon index over the period of the observation. This result is not affected by the choice of model components used to model the emission features in the 0.3−10.0 keV spectrum and is the same for the model in which the observed excess is represented as O VIII and Fe K_α Laor lines and for the model where the relativistic O VIII and Fe K_α lines are self consistently reproduced along with the reflected continuum by the HB model (see §5.3.2).

Intriguingly, the hard power-law component displays large variations in flux and

photon index similar to the soft power-law component when spectra are modeled in the 2−10 keV range. The minimum flux epoch (interval 6) is the only interval where the measured hard photon index and flux are consistent with the 0.3−10.0 keV results. To understand the reason for these inconsistencies we take a closer look at the model fits to the 0.3−10 keV spectra (Fig 5.13).

During the minimum flux epoch (interval 6) the intersection of the soft and hard power-laws is close to 1 keV. The soft component is very dim and steep and does not contribute significantly to the emission above 2 keV. The hard power-law is exclusively visible in the 2−10 keV band and dominates the X-ray emission in that energy range (Fig 5.13, panel 1). As the normalisation of the soft power-law increases (resulting in the brightening of the source) it contributes more and more to energies blue-ward of 2 keV (slowly dominating emission in that region) and the point of intersection of the two power-laws moves to higher and higher energies (Fig 5.13, panels 2 and 3). At the highest flux epoch the point of intersection of the two power-laws is close to 6 keV and the flux in the 2−10 keV range is largely dominated by the steep power-law emission (Fig 5.13, panel 4).

It is clear from Fig 5.13 that except during the low state (interval 6) the spectral parameters derived for the power-law component in the 2.0−10.0 keV energy range are a composite of the soft and hard power-law components present in the spectrum. As the source gets brighter the contribution of the soft component to the 2−10 keV band increases resulting in softer photon indices being measured. This gives rise to effects such as the photon index−flux correlation and saturation of photon index at higher luminosity which are possibly artifacts of modeling the spectrum in the 2−10 keV range with a single power-law and do not reflect the behaviour of the intrinsic hard power-law component (Fig 5.14).

The softening of the 2−10 keV power-law with increasing source brightness is commonly observed in AGN (Yaqoob et al. 1993, Grandi et al. 1992, Kunieda et al. 1992, Fiore et al. 1992 (ApJ 347), Nandra et al. 1991,1990, Maraschi et al. 1991, Matsuoka et al. 1990). The saturation of photon index at higher luminosity has also

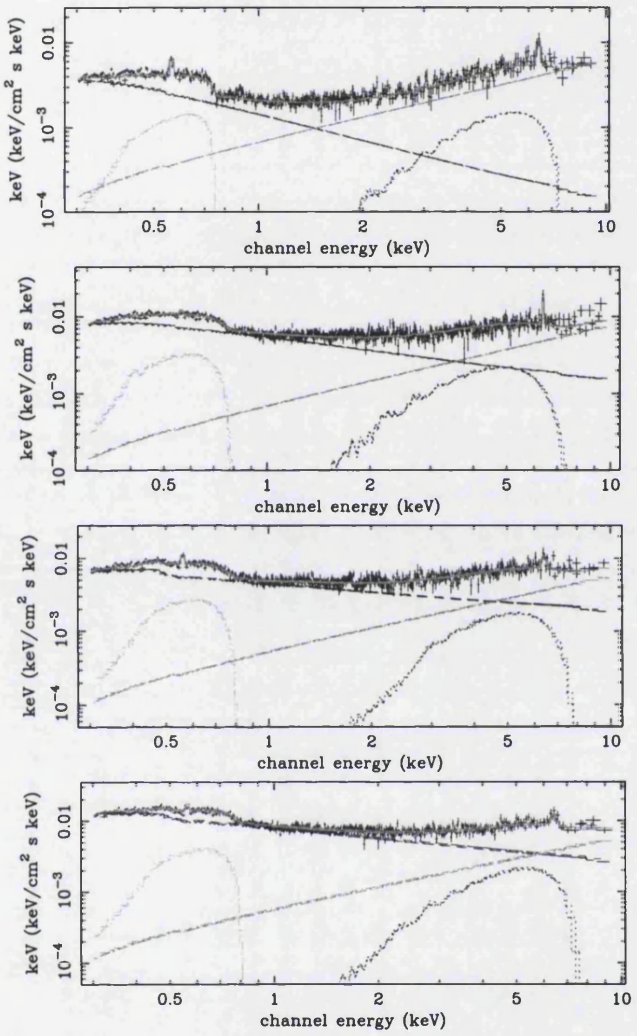

Figure 5.13: Model fits to the 0.3−10.0 keV spectrum of NGC 4051 in the order of increasing source brightness (from top to bottom). The top and bottom panels show model fits to the lowest and highest flux spectrum respectively. Best fit model to the lowest flux spectrum shows that the soft power-law does not contribute significantly to energies > 2 keV and the 2−10 keV emission is dominated by the hard power-law. It is seen that as the source luminosity increases the intersection of the soft and hard power-laws moves to higher and higher energies and the contribution of the soft power-law to energies > 2 keV steadily increases (middle panels). Model fit to the highest flux spectra show that the emission in the 0.3−10 keV range is totally dominated by the soft power-law.

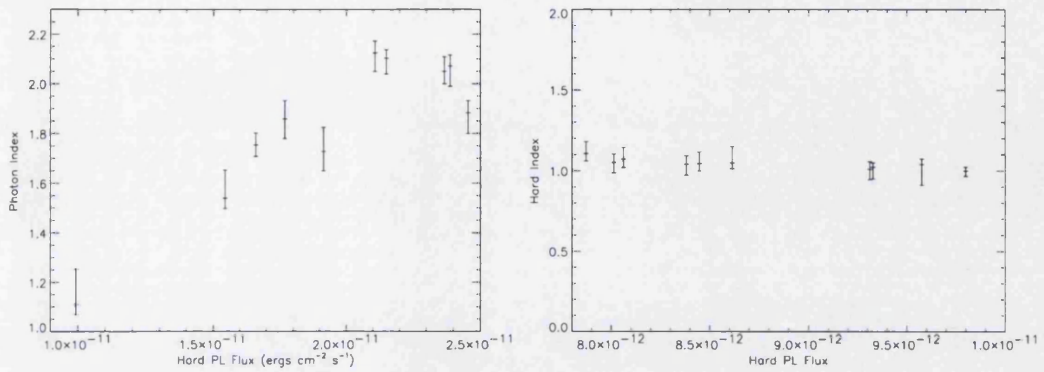

Figure 5.14: The left panel shows the photon index-flux behaviour when the underlying continuum in the 2−10 keV range is modeled with a single power-law and the right panel shows the photon index-flux behaviour when the underlying continuum in the wider 0.3−10 keV range is modeled with 2 power-laws

been observed in at least one other NLSG, MCG-6-10-15 (a source very similar to NGC 4051; Shih et al 2002). Observations such as these are generally considered to be indicative of a change in the intrinsic power-law emission and are usually interpreted in terms of physical changes in the X-ray producing environment. In the light of the findings of this study we should investigate whether the photon index−flux correlations observed in other AGN are also a result of changes in the relative intensities of two power-laws present in the 2−few 10s of keV spectral range (as seen in NGC 4051). Since the soft power-law may be driving changes in the 2−10 keV band, previous measurements of AGN variability in the 2−10 keV band are likely to describe the temporal behaviour of the soft power-law component and as such provide almost no information about the hard power-law component (if present).

5.4.2 Origin of the soft and hard power-law components

The long exposure, wide energy range (spanning both the soft and hard bands) and higher sensitivity of $XMM - Newton$ detectors has allowed the detection and simultaneous measurement of the soft and hard spectral components in NGC 4051 with a higher degree of precision than was possible with previous detectors. I require two power-law components to model the 0.3–10.0 keV spectrum of NGC 4051: a variable steep ($\Gamma \approx 2.5$–2.6) and luminous component, typically contributing almost 75 % of the flux in the 0.3–10 keV energy range, superimposed on a flat almost unvarying component of $\Gamma \approx 1$.

A steep excess at soft X-ray energies is observed in several narrow line Seyfert galaxies and has been interpreted as the high energy tail of the disk black body spectrum by several authors in the past (Arnaud et al. 1985, Pounds et al. 1986, Czerny & Elvis 1987). However, observational evidence of AGN spectral energy distributions (SED) in recent years, argues against the soft excess being thermal emission from a standard accretion disk (Shakura & Sunyaev 1973) representing the release of gravitational energy as a result of viscosity in the disk (Barvainis 1993, Mushotzky et al. 1993, Nayakshin et al. 1997, Kawaguchi et al. 2001).

Additionally, the strongest evidence against a direct link between the emission below 2 keV in NGC 4051 and the intrinsic (optically thick, viscous) disk emission is the detection of X-ray variability on time-scales as small as 200 s (Singh 1999, Lawrence et al. 1987). The variability time-scale is much smaller than the Keplerian time-scale of the disk (for $M_{BH} = 10^6\ M_\odot$) and it is highly unlikely that the rotational dynamics of the disk are directly responsible for the observed rapid variability.

The idea that rapidly variable X-ray emission observed in Seyfert galaxies may be produced in X-ray sources close to the disk surface has gained popularity in recent years. Leading models for X-ray emission identify these X-ray sources with regions of enhanced magnetic fields or 'patches' where magnetic reconnection activity takes place producing energetic electrons (and protons), which then up-scatter soft

photons mainly from the disk to give rise to observed X-ray emission. (Haardt et al. 1994, Nayakshin 1998). Magnetic corona models comprising of correlated magnetic flares above accretion disks have been able to reproduce the X-ray spectral and temporal variability observed in AGN on very short time-scales and also the observed AGN power density spectra (see Merloni & Fabian 2002).

My $XMM - Newton$ data favours the variants of these models in which the disk is illuminated by X-ray sources close to it. The observed rapid and sometimes non-linear X-ray variability in NGC 4051 also points towards turbulent processes like magnetic flares as its likely origin (Green et al. 1999). Thus it is possible that the dynamic steep component in NGC 4051 may be associated with localized flaring activity in the active regions of the corona. If this is correct the energetic electrons up-scattering soft photons to X-ray energies are also expected to lose energy (as γ decreases) due to inverse Compton radiation losses over time, and give rise to correlated (possibly time delayed) emission at lower frequencies (de Vries et al. 1992). This could be one possible explanation for the observed, almost simultaneous (rapidly varying) X-ray and EUV emission in NGC 4051 (Uttley et al. 1999).

The detection of two power-laws in the X-ray spectrum of NGC 4051 suggests the presence of two different electron scattering regions of different optical depths and temperatures. The luminosity and dynamic nature of the steep component associates it with the nuclear regions and I suggest that the electron scattering region responsible for its origin could be the active regions of the corona. However, the location of the scattering region responsible for the hard component is not clearly understood.

A flat component ($\Gamma \approx 1$) similar to that observed with $XMM - Newton$ has also been detected with $BeppoSAX$ in NGC 4051 during its long low state. Uttley et al (1999) and Guainazzi et al.(1998) interpreted this low state hard component as pure reflection from distant cold material, possibly the molecular torus. In order to produce a substantial reflected continuum the distant cold reflector would have to be Compton thick and as such we should observe an absorption edge at 7.1 keV along

with the 6.4 keV Fe K_α line (George & Fabian 1991). Although an edge-like feature is observed near 7 keV, its energy is inconsistent with that of a neutral iron edge ($E_{edge} = 6.89^{+0.12}_{-0.14}$ keV, where the errors are 4σ). This casts doubts on the model in which the hard power-law arises as a result of reflection from a molecular torus. However, the sensitivity of $XMM-Newton$ is not high enough to disentangle the complexities (emission and absorption features) in the iron K-band and it is possible that the presence of iron absorption lines (Fe XXV or higher and/or Fe K_β) may contribute to the low energy of the edge-like feature.

Support in favour of a non-torus origin for the hard power-law emission is also found in Fig 2 of Guainazzi et al. (1998) which shows that although the 2–10 keV flux does not vary much over the years (despite factor of 5 variations in 0.1–2 keV flux), the factor of 10 drop in the 0.1–2 keV flux during the low state is also accompanied by a factor of 10 drop in the 2–10 keV flux which makes a distant torus origin of the hard X-ray emission in NGC 4051 very unlikely.

Although the hard photon index measured during the low luminosity (low state) *BeppoSAX* observations and the higher luminosity $XMM-Newton$ observation is similar ($\Gamma \approx 1$) the hard power-law flux measured during the *BeppoSAX* observation is a factor of 10 lower (Guainazzi et al. 1998). Interestingly, the broad iron line flux measured during the *BeppoSAX* observation is also almost a factor of 10 lower (Guainazzi et al. 1998) than that measured during the $XMM-Newton$ observation. It appears that although the Fe K_α line flux does not respond to the observed rapid changes in X-ray flux it may be coupled to the long term variations in the hard power-law flux. The observed lack of variability in the hard power-law and iron line flux over the 103 ks observation, the simultaneous factor of 10 decrease in flux observed during the long low state (Guainazzi et al. 1998) and the persistence of both components during the low states when the luminous, variable, steep component has almost disappeared suggests a connection between the two. I consider the possibility that the bulk of the broad line flux may be due to the re-processing of the hard component by the disk. In such a scenario the hard component must see a significant

solid angle of the disk in order to account for the large Fe K_α line equivalent width (EW $\approx$ 800 eV) measured by XMM-Newton. I suggest that the hard X-ray power-law may also originate in the inner regions of NGC 4051 in close proximity to the accretion disk.

5.4.3 Emission lines

Fe K_α profile

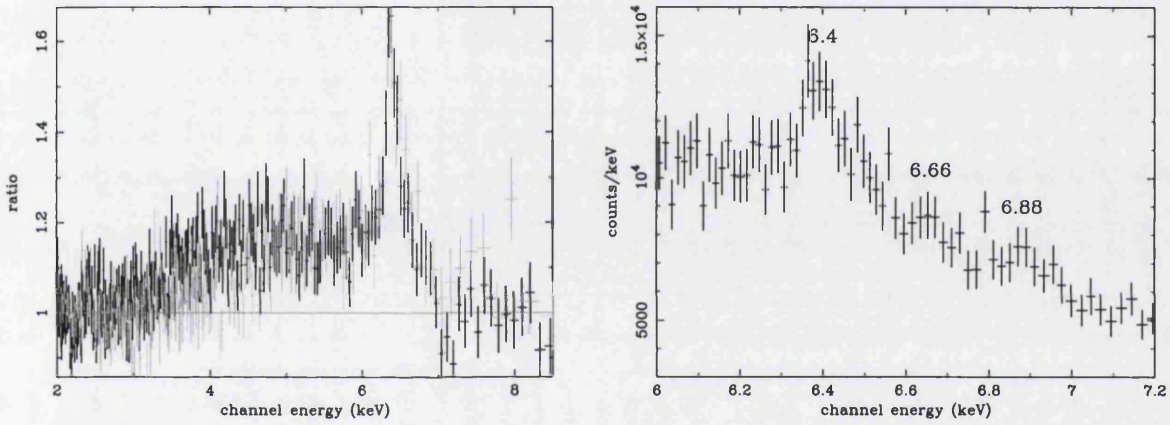

Figure 5.15: *Left* : The broad Fe K_α line profile in NGC 4051. The plot shows the MOS (dark) and PN (light) data. *Right* : A close-up of the Fe K_α line profile in the 6−7 keV region. A strong narrow line is observed at neutral iron energy. There are small enhancements at 6.7 keV and 6.9 keV which may be a hint of weaker high ionisation lines.

The observed iron line profile consists of a broad component extending down to almost 3 keV and narrow lines at 6.4 keV and possibly at 6.66 keV and 6.88 keV (Fig 5.15). The narrow 6.4 keV line is weaker ($F_{6.40} = 2.24\times10^{-13}$ ergs cm^{-2} s^{-1}, EW $= 70^{+6}_{-6}$ eV) than the broad iron line component ($F_{Laor} = 2.14\times10^{-12}$ ergs cm^{-2} s^{-1}, EW $= 800^{+65}_{-128}$ eV).

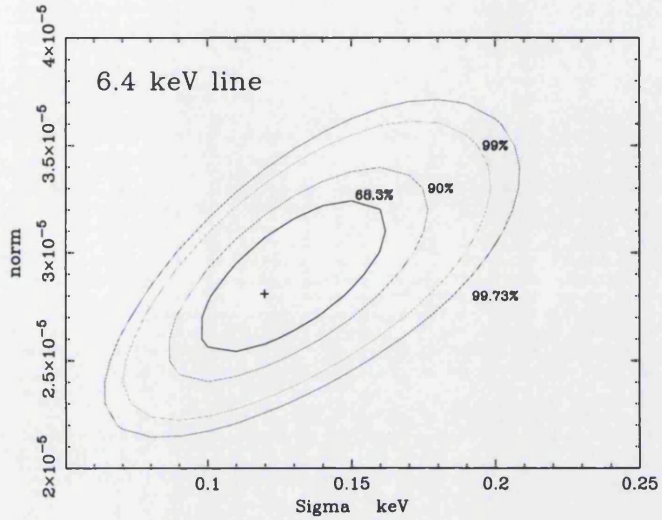

Figure 5.16: Contour plot for the narrow line at 6.4 keV. The line is marginally resolved by the EPIC

The 6.4 keV line in NGC 4051 is marginally resolved by the EPIC (Fig 5.16) and has a velocity width FWHM = 13220^{+4408}_{-7708} km s^{-1} (σ= 0.12 keV). A narrow line at 6.4 keV is now a common feature in the X-ray spectra of Seyfert galaxies ($L_{2-10} < 10^{45}$ erg s^{-1}) observed with $XMM - Newton$ and is generally interpreted in the context of reflection from cold distant material, possibly a molecular torus. Reflection from dense cold material is expected to produce both a flourescence line at 6.4 keV and an absorption edge at 7.1 keV (George & Fabian 1991). The absence of a neutral iron edge in the $XMM - Newton$ spectrum of NGC 4051 makes it unlikely that the narrow line at 6.4 keV arises in an optically thick target like a torus. Also the measured velocity width of the neutral Fe K_α line is larger than that of the H_β (FWHM = 1110±190 km s^{-1}) and the He II λ4686 lines (FWHM = 5430±510 km s^{-1}) which are thought to originate in regions much closer to the black hole.

A strong line at 6.4 keV unaccompanied by a substantial iron absorption edge is expected from reflection of a Compton thin target like the broad line clouds (Shields

et al. 1995) and as such the possibility of the 6.4 keV line in NGC 4051 originating closer to the black hole (e.g. within the BLR) cannot be rule out. Evidence for a BLR (or closer) origin of the 6.4 keV line has also been found in NGC 3783, NGC 5548 and MCG-6-30-15 where the narrow line has been resolved by the *Chandra* HETG (Yaqoob et al. 2001, Kaspi et al. 2002,Lee et al. 2002), indicating velocity widths much larger than those expected from a distant torus. Interestingly the FWHM ($\sim$ 11,000 km s^{-1}) and the equivalent width (EW $\sim$ 110 eV) of the resolved narrow line in MCG-6-30-15, a narrow line Seyfert 1 galaxy, is very similar to that measured in NGC 4051 (Lee et al. 2002).

The broad Fe K$_\alpha$ line detected in NGC 4051 is not a common feature in *XMM–Newton* spectra of Seyfert 1 galaxies and has been convincingly detected in only a few sources for which relatively long exposures are available. The presence of a broad iron line in a significant amount of sources is currently under dispute mainly because the broad excess around iron line energies can be also be accounted for by reflection and absorption of the primary X-ray emission (Pounds & Reeves 2002, Page et al. submitted). The key to correct interpretation of the broad residuals as either red line wing or reflected continuum lies in the ability to correctly discriminate between the blue cut-off of the broad iron line and an absorption edge. In the case of NGC 4051 the measured energy of the Fe K$_\alpha$ blue cut off is too low to be confused with that of an iron absorption edge and the reflection origin of the broad excess in this source is not supported by the XMM-Newton data.

The Fe K$_\alpha$ line in NGC 4051 displays an extreme red extension, down to almost 3 keV which has been detected in only three other sources (to the best of my knowledge) MCG-6-30-15, Mrk 766 and NGC 3516 with XMM-Newton (Fabian et al. 2002, Mason et al. 2002, Turner et al. 2002). If the breadth of the line is interpreted as broadening due to gravitational and Doppler effects, it is consistent with the presence of a rotating black hole at the center of these sources. The presence of a broad 6.4 keV line indicates that the line emitting material is not highly ionised which is consistent with the relatively low ionisation parameter of $\xi < 200$ measured

for the disk in NGC 4051 (Matt et al. 1993).

Soft X-ray line

Apparent relativistic soft X-ray emission lines have so far been detected in five sources: NGC 4051, Mrk 766, MCG-6-30-15, MCG-2-58-22 and NGC 5548 (this study, Branduardi-Raymont et al. 2001, Mason et al. 2003, chapter 4, Kaastra et al. 2000). However, the lines detected in MCG-2-58-22 and NGC 5548 are much weaker and not as visually prominent as the ones in the lower luminosity sources NGC 4051, Mrk 766 and MCG-6-30-15 ($L_{2-10} < 10^{43}$ erg s^{-1})

The soft X-ray spectrum of NGC 4051 displays only an O VIII line whose emission profile is distinctly different from the saw-tooth shaped O VIII, N VII and C VI lines observed in Mrk 766 and MCG-6-30-15. The O VIII line equivalent width (EW $\approx$ 70 keV) in NGC 4051 is lower than that observed in Mrk 766 and MCG-6-30-15 (EW $\approx$ 140$-$160 eV; Branduardi-Raymont et al. 2000, Sako et al. 2001) but is higher than that in MCG-2-58-22 and NGC 5548 (EW $\approx$ 16$-$20 eV; chapter 4, Kaastra et al. 2000) The derived emissivity index of $q \sim 6$ indicates that the most of the line emission in NGC 4051 is originating in the innermost parts of the disk but over a region much smaller than that in the other four more luminous sources for whom the derived emissivity index $q \sim 3-4$ (Branduardi-Raymont et al. 2000, Kaastra et al. 2000, chapter 4).

The O VIII line flux in NGC 4051 is also highly variable and positively correlated with the soft power-law flux. The line EW is relatively stable over the period of the observation (which is consistent with the line flux and continuum flux correlation) except for a sharp increase during the minimum flux epoch (interval 6), indicating a sudden rise in the line flux or a decrease in the power-law continuum flux. An examination of line and power-law flux during minimum (interval 6) shows that the O VIII line flux is lower by about 50% and the continuum flux is lower by almost 70% compared to that in interval 5, which suggests some kind of a time delayed response of the line flux with respect to the continuum.

Emission lines from medium-Z elements have been predicted by reflection models as a consequence of re-processing of the primary radiation by the disk. The close coupling observed between the illuminating soft power-law flux and the O VIII line flux in NGC 4051 provides evidence in favour of close proximity of the illuminating power-law and line producing region. However, it is not understood why these lines are present in some sources and absent in others. Sako et al. 2001 have suggested that the the absence of lines in certain sources could be due to the formation of a very hot skin ($T \approx 10^8$ K) on top of the disk as a result of strong X-ray irradiation (i.e. $F_x >> F_d$) from above. The H-like C, N, and O abundances in the hot ionised layer are expected to be very low resulting in small photo-electric opacities and consequently little or no line emission.

5.4.4 Physical interpretation of results

The ionisation state of the surface of the disk is governed by the intensity of the illuminating X-ray radiation. Currently there exist two popular models for X-ray illumination of accretion disks in AGN: a point-like source above the disk evenly illuminating a large surface area of the disk and X-ray sources close to the disk surface (i.e. active regions) illuminating relatively smaller areas in their vicinity. My X-ray data favour the model in which the X-ray sources lie close to the disk surface. In such a scenario the disk will be unevenly illuminated and the areas of the disk in close proximity to the X-ray sources will be strongly irradiated and be more ionised than the regions further away. The presence of relativistic neutral Fe K_α and H-like oxygen lines in the X-ray spectrum of NGC 4051 and the different temporal behaviour observed for the two could be explained in terms of the O VIII and Fe K_α line emission arising from completely different regions of the disk (one more ionised than the other). However, relativistic line model fits to the emission profiles suggests that both lines arise from similar regions of the inner disk (see table 5.2). This can be understood if the variable X-ray sources produce photons

(or electrons) with energies high enough to almost fully strip oxygen atoms but not high enough to produce iron line emission. Such a scenario is supported by the spectral analysis results which show that the variable soft power-law component in NGC 4051 does not typically contribute much to energies beyond 6 keV. As such the Fe $K_\alpha$line emission could be produced by a harder continuum source shining down onto the same regions in which the O VIII line originates.

The HB reflection model fits to the data suggest that the system is accreting at a low rate of of $\dot{m} = 6^{+3.00}_{-0.05} \times 10^{-4}$ (in Eddington units). In fact the model is unable to satisfactorily reproduce the soft excess for $\dot{m} > 0.001$. This is contrary to popular belief that NLS1s are low mass, high accretion rate systems. However, the model accretion rate agrees well with the optical luminosity ($L_{vis} = 0.001 L_{EDD}$; Peterson & Wandel 2000) of NGC 4051. An estimate of the central black hole mass can be obtained from model accretion rate $\dot{m}$ (in Eddington units) using the equation,

$$M \approx \frac{L}{\dot{m}(1.3 \times 10^{38})} \tag{5.1}$$

where M is the mass in solar units, and L is the bolometric luminosity in erg s^{-1}. A correction factor is applied to the measured X-ray luminosity ($L_{2-10} = 3 \times 10^{41}$ erg s^{-1}) to obtain the bolometric luminosity ($L_{X-ray} = 0.05 L_{bol}$; Elvis et al. 1994). I infer a black hole mass of $\approx 10^7$ $M_\odot$ for NGC 4051 which is higher than the previous mass estimate obtained from the Hβ line width (10^6 $M_\odot$; Peterson et al. 2000) but is consistent with the mass estimate obtained from accretion disk and corona models by Mathur et al. 2001. The local X-ray to disk flux ratio obtained is also low ($F_X/F_d < 1$), i.e. the disk is weakly illuminated. Similar evidence for a weakly illuminated disk has also been observed in MCG-6-30-15 a very similar NLSG (Ballantyne & Fabian 2002). This is in agreement with the arguments made by Sako et al. 2001 whereby disk flux larger than the illuminating X-ray flux creates conditions favourable for the emergence of soft X-ray lines.

A low accretion rate and low X-ray to disk flux ratio conflicts with current theoretical arguments which suggests that the fraction of the gravitational energy dissipated in the corona (f) increases as $\dot{m}$ (accretion rate in Eddington units) decreases (as the disk gets more gas pressure dominated). Hence we should (theoretically) expect a greater fraction (f) of energy to be dissipated in magnetic fields in low $\dot{m}$ systems (Merloni et al. 2002) resulting in F_X/F_d ratio > 1, i.e. a strongly illuminated disk (see Nayakshin 1998).

5.4.5 The low flux states of NGC 4051

Anomalous steepening of the power-law index

Despite large variations in flux, the soft power-law index in NGC 4051 is relatively stable within a narrow range ($\Gamma_{soft} = 2.5-2.6$) except during the minimum flux epoch (interval 6) when an anomalous steepening of the soft photon index to $\Gamma_{soft} = 3$ ($\Gamma_{hard} \approx 1.0$) is observed.

NGC 4051 exhibits not only brief low flux periods ($\sim$ few 10 ks) but also long low states lasting several weeks. Both the short and long low flux periods are characterised by an extremely low nuclear (both soft and hard band, 0.1−10 keV) flux which is $\sim$ factor of 10−20 lower than that observed during its 'normal state', and an apparent absence of large amplitude rapid variability (Uttley et al. 2001, Collinge et al. 2001, Uttley et al. 1999; Guainazzi et al. 1998). Interestingly, the spectral nature of the source during the long low states is almost *identical* ($\Gamma_{soft} = 3$, $\Gamma_{hard} \approx 1.0$) to that observed during the relatively brief 10 ks low flux epoch of the $XMM-Newton$ observation (Guainazzi et al. 1998, Uttley et al. 2001).

One possible explanation for the observed steepening is that it is a result of an intrinsic change in the soft photon index signifying a physical change in the X-ray emitting environment. However, it is also possible that the observed steepening is a result of another lower luminosity component coming into view at the soft X-ray energies when the soft power-law flux drops dramatically. The soft (0.1−2.0 keV)

band flux measured during the 10 ks low state of the $XMM - Newton$ observation ($0.93\pm0.03\times10^{-11}$ erg cm^{-2} s^{-1}) is similar to that measured by *BeppoSAX* ($0.4-1.0\times10^{-11}$ erg cm^{-2} s^{-1}) during one of the longest observed low states of NGC 4051 (1998) when the source of variable X-ray emission switched off for several months. Hence it is possible that dimming of the primary continuum allows a glimpse of the relatively weaker soft X-ray emission from the nuclear regions of NGC 4051, probably associated with the observed outflow of gas from the nucleus of this galaxy (Christopoulou et al. 1996).

A comparison of the hard band flux during the brief and long low states of NGC 4051 shows, that although the 2–10 keV flux measured during the $\sim$ 10 ks low flux periods observed during the $XMM - Newton$ and $CHANDRA$ observations (Collinge et al. 2001) is similar ($F_{2-10} \approx 1\times10^{-11}$ erg cm^{-2} s^{-1}), that measured during the long *BeppoSAX* low state is a factor of 10 lower ($F_{2-10} \approx 1\times10^{-12}$ erg cm^{-2} s^{-1}; Guainazzi et al. 1998). Since the 0.1–2 keV flux measured during the brief and long low states is similar, it indicates that the 0.1–10 keV spectrum of NGC 4051 is much harder during the brief low flux periods compared to the long low states.

This study has shown that the brief low flux epoch (interval 6) observed during the $XMM - Newton$ observation is caused by a factor of 6–7 drop in the soft power-law flux, with no change in the hard ($\Gamma \approx 1$) power-law flux (which is almost constant throughout the 103 ks exposure). However, a factor of 10 drop in both the soft (0.1–2 keV) and hard (2–10 keV) band flux is reported for the long *BeppoSAX* low state (Guainazzi et al. 1998). It appears that the dimming of only the rapidly variable (soft) X-ray source causes the the brief low flux periods, while the dimming of both the hard ($\Gamma \approx 1$) and the rapidly variable soft X-ray sources results in the long low states (several weeks), suggesting that it may actually be the hard X-ray source whose fading and brightening may be driving the long low and the 'normal' states respectively, in NGC 4051. Clearly, a proper understanding of the origin and nature of the hard X-ray emission in NGC 4051 would provide a valuable insight

into the complex emission mechanism in the source.

What causes the observed low states

Uttley et al. (1999) and Guainazzi et al. (1998) have interpreted the low flux state of NGC 4051 in 1998 May as the switching off of the nuclear source. However, the presence of a strong relativistic Fe K_α line (see Fig 5.15) observed during the *XMM – Newton* minimum flux epoch (interval 6) is inconsistent with the absence of any illuminating X-ray source in the nuclear regions when the rapid variability and flux have been dramatically reduced.

Peterson et al. (2000) have observed that the broad 'normally' variable (along with the X-rays, optical continuum and H_β line), He II λ4686 line is absent or weak during the low states of NGC 4051, while the optical continuum and the H_β emission line continue to be present and variable. They have used this information to argue that the low state of NGC 4051 is a result of the inner region of the accretion disk entering an advection dominated accretion flow (ADAF) state in which the radiative efficiency of the disk is greatly diminished (Narayan et al. 1998; Narayan et al. 1994). However, the presence of a relativistic Fe K_α line during the brief low state of *XMM – Newton* cannot be reconciled with the ADAF scenario.

I have suggested that the X-ray emission in NGC 4051 can be explained by the presence of two different electron scattering regions near the central black hole: X-ray sources close to the disk (identified with active regions in the corona) giving rise to the variable soft power-law component, ionising regions of the disk in their vicinity and creating conditions favourable for emission of H-like oxygen line and a second scattering region also in the vicinity of the disk that produces the non-varying hard power-law and the broad Fe K_α emission line. The appeal of the two electron scattering region model is that, it provides a very simple explanation for the low state (both long and brief) observations of NGC 4051. The flux in the soft power-law during the *XMM – Newton* observation is a factor of 6–7 times greater than that in the relatively non-varying hard component (see Fig. 5.9). If the variable

soft power-law does originate in X-ray sources close to the disk (i.e. AR's), the disappearance of these X-ray sources would lead to the disappearance of the rapid variability, an almost factor of 10 reduction in continuum flux and a large drop in the O VIII line flux. The accretion disk, the second scattering region and hence the hard power-law component illuminating the disk would still be present and as such we would still observe a strong relativistic iron line in the spectrum especially if the the bulk of the iron line flux was being generated by the X-ray illumination of the disk by the hard power-law component.

5.4.6 Multiwavelength emission

Fig 5.17 shows the spectral energy distribution (SED) of NGC 4051 from radio to X-rays. The dark data points represent the simultaneous $XMM - Newton$ observations while the lighter open circles represent the non-simultaneous archival data. The SED shows an almost 5 decade drop in power output in the sub-millimeter band which is typical of radio quiet AGN. The far to mid−infrared spectrum peaks at around 100μm and 20μm which has been interpreted in terms of emission from cold and relatively warm dust respectively (Rodriguez et al. 1996). The emission from warm dust is generally associated with the nuclear regions while the cold component is thought to be emission by dust heated in the cooler star forming regions (Telesco et al. 1989, Rodriguez et al. 1996). The dominance of the cold dust component over the warm component implies that the relative strength of the infrared emission from cooler star forming regions is higher than that from the nuclear regions of NGC 4051 (also see Rodriguez et al. 1996). The near IR to optical spectrum is almost flat with no evidence for an excess in the 3μm−5μm region which is generally observed in Seyfert galaxies (and is thought to be associated with emission from hot dust near the nucleus). The absence of the 3μm−5μm excess and the relative weakness of the warm dust component suggests that NGC 4051 may not contain significant

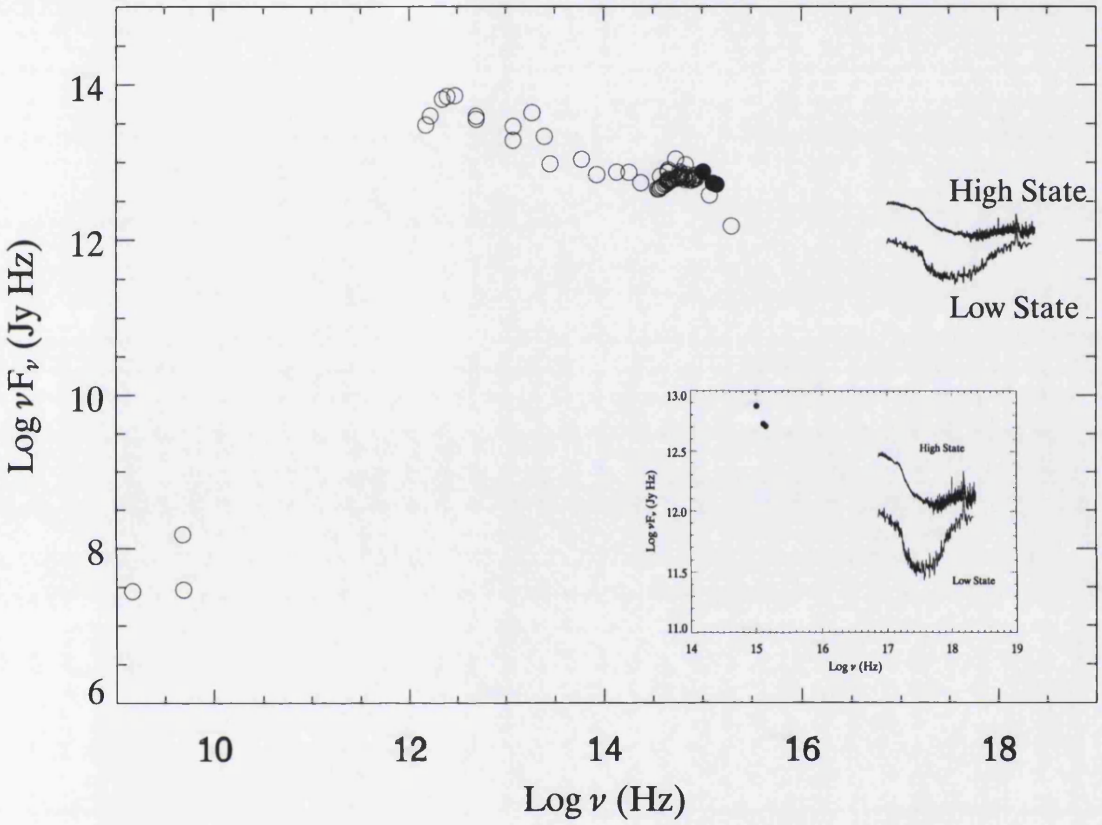

Figure 5.17: Spectral energy distribution of NGC 4051. The dark data are the simultaneous $XMM-Newton$ observations and the lighter open circles are the non-simultaneous archival data (see text for details). The $XMM-Newton$ and archival data are corrected for Galactic extinction. There is no significant evidence for a UV black body component and the X-ray (in high state) to UV energy density is comparable. The inset panel shows the simultaneous $XMM-Newton$ observations.

amounts of dust near the nucleus (Salavati et al. 1993) which points towards a non-thermal origin of the infrared emission in the source. The UV excess (the rise in the optical–ultraviolet continuum above the infrared) commonly observed in Seyfert 1 galaxies (Edelson & Malkan 1986) is absent in the SED of NGC 4051. The UV excess is usually interpreted in terms of thermal emission from an accretion disk (Czerny & Elvis 1987) which if true would suggest that either the intrinsic disk flux (UV) in NGC 4051 is very low compared to most AGN or that the disk emission peaks at higher energies (in the unobservable EUV region) which would be more in agreement with the black hole mass estimate ($\sim 10^{6-7}$ $M_{\odot}$) of the source.

The SED shows a very gradual decline from the optical/UV to soft X-ray region. The near IR to optical SED has a power-law slope of $\Gamma \approx 2.3-2.4$ (Done et al. 1990, Edelson & Malkan 1986) which is close to the value measured in the soft X-ray region ($\Gamma \approx 2.5\pm0.1$). Thus it is possible that the soft X-ray power-law in NGC 4051 extends down to the optical/IR region as has been suggested for some objects by Carleton et al. (1987). At frequencies greater than 10^{18} Hz the SED turns over and rises towards higher X-ray energies. This upturn at hard X-ray energies is characteristic of radio-loud and high luminosity Seyfert 1 galaxies and is not typically observed in low luminosity radio quiet AGN (Elvis et al. 1994). This hard X-ray emission cannot be an extension of the slightly decreasing near-IR to soft X-ray emission and must be a new component emerging in the X-rays in NGC 4051.

Overall, the near-IR to optical energy density in NGC 4051 is comparable. The simultaneous, rapidly variable emission observed at EUV and X-ray wavelengths (Uttley et al. 1999) in NGC 4051 suggests that the emission has a common region of origin. Recent simultaneous X-ray and UV observations of the source (with *XMM – Newton*) have also shown that the emission at 2900Å is correlated with the underlying variations in X-ray flux with a lag of about 12 ks (Mason et al 2002). The time lag of a few hours between the X-ray and UV emission and that of several days between the time averaged X-ray and optical emission (Peterson et al. 2000) is indicative of re-processing of X-rays in a spatially different (and probably much

larger) region possibly the outer regions of the accretion disk. The correlation of the X-rays with the EUV, UV and optical emission suggests that the X-ray emission is driving variability at lower frequencies.

5.5 Summary

The *XMM − Newton* spectra do not show evidence of substantial neutral reflection from a distant molecular torus in the X-ray emission of NGC 4051. I find that the underlying X-ray continuum in NGC 4051 can be described by reflection from a mildly ionised disk and two power-law components. The hard power-law component ($\Gamma \approx 1$) is relatively unvarying in both flux and photon index. Superimposed is the soft power-law component which exhibits factor of 6−7 variation in flux with the photon index relatively stable within a narrow range ($\Gamma = 2.5-2.6$) and is responsible for a large fraction (typically 75%) of the observed X-ray flux and almost all the observed rapid variability. Additionally the spectrum also displays narrow and broad emission features from oxygen and iron. The narrow Fe K_α and [O VII] lines and the relativistic Fe K_α line do not display any significant flux variations and are almost unvarying over the 103 ks observation. However, the relativistic O VIII line flux shows large amplitude variations which are correlated with the soft power-law flux.

The hydrostatic balance reflection model (Nayakshin et al. 2001) is moderately successful in reproducing the broad O VIII and Fe K_α emission lines, in a self consistent manner along with the reflected continuum. The reflection model fits to the data suggest the presence of a weakly illuminated disk ($F_X/F_d < 1$) and a low accretion rate ($\dot{m} \lesssim 0.001$) in NGC 4051. The black hole mass inferred from the model accretion rate is $\approx 10^7$ $M_\odot$.

The soft power-law component contributes significantly at energies > 2 keV and dominates emission in the 0.3−10 keV range. The contribution of the soft power-law component to the 2.0−10.0 keV band is variable and increases as the source brightens. The change in the relative intensities of two power-laws present in the

2−10 of keV spectral range gives rise to effects such as the photon index−flux correlation and saturation of photon index at higher luminosity which are probably artifacts of modeling the spectrum in this energy band with a single power-law.

The X-ray emission in NGC 4051 and its low states can be accounted for by the presence of two different electron scattering regions in the inner regions of the disk. One of the scattering regions can be identified with X-ray sources close to the disk (i.e. the active regions) giving rise to the soft variable power-law and ionising regions of the disk surface in their vicinity, thereby creating conditions favourable for emission of the O VIII line. The origin of the second scattering region (which produces the hard power-law component) is unclear. However, the almost unvarying nature (over 103 ks) of both the hard power-law flux and the relativistic Fe K_α line, a similar decrease (factor of 10) in their flux over time-scales of years and their continued presence during the low states when the variable components have disappeared (or drastically reduced) hints at a close connection between the two. I suggest that the second scattering region also lies in the vicinity of the accretion disk and that the bulk of the broad iron line emission may be due to the re-processing of the hard power-law component.

Chapter 6

Discussion

6.1 Observational summary

In this thesis I have studied 3 observationally very different AGN: a low luminosity ($L_{2-10} \sim 10^{40-41}$ erg s^{-1}) narrow line Seyfert 1 Galaxy NGC 4051, a bright ($L_{2-10} \sim 10^{44}$ erg s^{-1}) radio quiet Seyfert 1 Galaxy MCG-2-58-22 and a luminous ($L_{2-10} \sim 10^{45}$ erg s^{-1}) radio-intermediate (i.e. radio weak but with relativistic jets pointed straight at the observer) quasar III Zw2. The observational results of these three AGN are summarised below.

1. The 0.3−10.0 keV continuum in NGC 4051 can be described by two power-law components : a luminous variable power-law ($\Gamma \approx 2.5$) superimposed on to a relatively unvarying harder power-law of $\Gamma \approx 1$. The 0.3−100.0 keV continuum in MCG-2-58-22 is also characterised by two power-laws: a luminous component of $\Gamma \approx 2.0$ superimposed on to a flatter component of $\Gamma \approx 1.3$. The 0.3−10.0 keV continuum in III Zw2 can be described by a single power-law of $\Gamma \approx 1.7$.

2. A relativistic, Fe K_α emission line from neutral or slightly ionised iron (< Fe XVI) and a narrow line at 6.4 keV is detected in NGC 4051. The X-ray spectrum of MCG-2-58-22 also displays broad Fe K_α emission but from highly

ionised iron ($\geq$ Fe XXV), together with a narrow line at 6.4 keV. However, the equivalent widths of both the narrow and broad Fe K_α lines in MCG-2-58-22 are much lower than those observed in NGC 4051. The X-ray spectrum of III Zw2 displays only a broad iron line. However, accretion disk model fits (for inclination $\leq 40°$) to the observed profile yield energies which are substantially higher (> 7.5 keV) than the line center energies of Fe K_α emission (6.4–6.97)(Chapter 1., §3.4.1).

3. A relativistic O VIII line is observed in the soft X-ray spectra of NGC 4051. A broad O VIII line emission is also detected in MCG-2-58-22; notably the first detection of its kind in a high luminosity Seyfert. There is no significant evidence for an O VIII line in the soft X-ray spectrum of III Zw2 (EW $<$ 100 eV)

4. The X-ray emission in NGC 4051 varies rapidly on very short time-scales. The X-ray emission in the higher luminosity sources MCG-2-58-22 and III Zw2 does not exhibit rapid flux variations over time-scales of $\sim$ few 10^3 s. However on time-scales of months the X-ray emission in both sources shows large amplitude variations in flux. Similar large amplitude variability over time-scales of months has also been reported in NGC 4051 (Uttley et al. 1999).

5. The emission in III Zw2 exhibits correlated variability from the radio to the X-rays. Related variations in flux over small spectral ranges (optical (U, B, V, R, I), infrared (J, H, K, L) and UV (1308 Å and 2303 Å)) are observed in MCG-2-58-22. Unfortunately, there is no overlap between the time intervals over which observations at different wave-bands were made and it is not possible to determine if the observed variations at the infrared, optical, UV and X-ray wavelengths are linked with each other.

6. A strong reflection component is measured in the spectra of all three sources.

6.2 The underlying continuum

It is generally thought that the X-ray emission in AGN is a single power-law and almost all other features observed in the X-ray spectrum are due to the re-processing of the primary X-ray continuum by material in its vicinity (Haardt & Maraschi 1993, Lightman & White 1988, George & Fabian 1991, Reynolds & Fabian 1995, Cappi et al. 1996). The soft X-ray excess is either optically thick emission from the disk or a result of re-processing of the illuminating power-law continuum by the disk, the Fe K_α line and the observed spectral hardening at higher X-ray energies is due to reflection/re-processing of primary X-rays by the disk and/or other material (e.g. broad and narrow line clouds, torus etc.) and the narrow emission and absorption features are imprinted on to the X-ray spectrum by a warm absorber in the AGN rest frame.

The underlying continuum in the $XMM-Newton$ X-ray spectra of the radio-quiet Seyfert 1 galaxies studied in this thesis (NGC 4051 and MCG-2-58-22) shows substantial curvature and cannot be modelled by a single power-law. The spectral curvature is greater, and the change in spectral gradient from steep to hard occurs at lower X-ray energies, in the less luminous source NGC 4051 ($L_{2-10} \approx 10^{41}$ erg s^{-1}, Fig 5.17) compared to MCG-2-58-22 ($L_{2-10} \approx 10^{44}$ erg s^{-1}, Fig 4.9). Such increase in spectral curvature and decrease in the energy at which the change in spectral slope takes place, with decrease in source luminosity has also been detected in several other AGN observed with $XMM-Newton$ (Pounds & Reeves 2002). The X-ray continuum in III Zw2, a luminous quasar ($L_{2-10} \approx 10^{45}$ erg s^{-1}) with relativistic jets pointed straight towards us, however, does not show significant spectral curvature at least in the 0.3−10 keV energy range and can be successfully modeled with a single power-law.

The effectiveness of spectral information as a diagnostic tool to study the X-ray emitting environment depends critically on the correct interpretation and modeling

of the spectral components. The high sensitivity and signal to noise of the XMM-Newton data have allowed for a better identification of spectral components in the X-ray spectra of AGN and have shown that the steeper low energy X-ray emission in NGC 4051 and MCG-2-58-22 is not a black body and that the observed flattening of the power-law slope at higher X-ray energies cannot be completely accounted for by the presence of a Compton reflection hump (§4.4.1 and §5.3.1). The spectral shape, however, can be successfully modeled using two power-laws: a steep component ($\Gamma \geq 2$) characterising the low energy X-ray emission superimposed onto a flatter component ($\Gamma \approx 1-1.3$) extending to higher X-ray energies.

How does change in interpretation of the spectral shape from the conventional blackbody plus power-law to two power-laws, in NGC 4051 and MCG-2-58-22, affect our understanding of the physical processes taking place in the inner regions of these (and other similar) AGN? These are some of the issues that this study has tried to tackle.

6.2.1 The steep power-law component (SP)

Results of previous analysis where the steep lower energy emission in AGN was successfully modeled as a thermal black body suggested that the steep component does not "contaminate" data at energies E > 2 keV (Pounds et al. 1994, Mushotzky 1993). However, the $XMM-Newton$ RGS data have shown that the emission below 2 keV does not resemble a black body spectrum and instead is made up of complex emission and absorption features imprinted onto an underlying power-law (this study, Branduardi-Raymont et al. 2000, Mason et al. 2002). When the steeper low energy continuum is modeled as a power-law it is seen that this steep power-law (SP from now on) contributes almost 75% of the total flux (in the 0.3−10 keV band) and extends to energies much higher than 2 keV and in fact dominates emission in the 0.3−10 keV range in both the low and high luminosity sources studied in this thesis

.

In the case of NGC 4051 where time resolved spectroscopy was possible it is seen that the SP varies rapidly in flux (and is responsible for almost all the observed flux variability) maintaining a relatively stable photon index (in the 'normal' state) which causes the SP contribution to energies beyond 2 keV to increase and decrease along with the source brightness. If we assume that the X-ray variability in NGC 4051 is a microcosm of X-ray variability in all AGN (as suggested by Uttley et al. 1999, based on comparison of long time-scale X-ray variability in NGC 4051 and Galactic black hole candidates) and that the range of behaviours it exhibits over a short time is analogous to that occurring in more luminous sources over longer periods of time (several months), then the tendency of the SP to contribute more and more to energies $>$ 2 keV with increasing luminosity has important repercussions for single power-law measurements made in the 2–few 10s of keV energy range of AGN.

Spectral measurements at energies $>$ 2 keV have revealed effects such as softening of the photon index with source brightness to be a common phenomenon in AGN (Yaqoob et al. 1993, Grandi et al. 1992, Kunieda et al. 1992, Nandra et al. 1991,1990, Maraschi et al. 1991, Matsuoka et al. 1990). These results have been interpreted as indications of physical changes in the X-ray producing environment (i.e. changes in the properties of the corona) and several theories have been proposed to explain these observations (e.g. the thunder-cloud model; Merloni & Fabian 2001). However, this study has shown that it is the variable contribution of the SP to the 2–few 10's of keV energy range that gives rise to the photon index–flux correlation and other effects like the saturation of photon index at high luminosity, which are probably artifacts of modeling the spectra in this particular energy range with a single power-law and may not necessarily indicate a physical change in the properties of the X-ray producing environments.

Since the 2–few 10s keV energy range consists of contribution from both the SP and the harder power-law, single power-law measurements in this energy range are unlikely to be a reliable measure of either of the two components. In order to disentangle the complexities in AGN spectra and to measure the strength and extent

of the various continuum components reliably high signal to noise data spanning both the soft and hard bandwidths is required. *XMM − Newton* and Chandra data provide an excellent opportunity to analyse spectra over wider energy bands and thus better understand the intrinsic behaviour of different components of X-ray emission in AGN.

In order to investigate the properties of the X-ray producing regions of the Seyfert galaxies studied in this thesis, I compare the SP of these sources. Although I do not know if a harder component exists at higher energies in III Zw2, for the purpose of this discussion the single power-law detected in the 0.3−10 keV range will be considered to be the SP. In the low luminosity source NGC 4051 ($L_{2-10} \sim 10^{40-41}$ erg s^{-1}) the SP has a photon index of $\Gamma \approx 2.5$ and out-shines the hard power-law emission up to $\sim$ 4 keV (for the integrated spectrum). In the higher luminosity source MCG-2-58-22 ($L_{2-10} \sim 10^{44}$ erg s^{-1}), the SP has a photon index $\Gamma \approx 2$ which is typically observed in Seyfert galaxies (Nandra 1994) but it out-shines the hard power-law emission almost up to 8 keV. The SP in the luminous quasar III Zw2 ($L_{2-10} \sim 10^{45}$ erg s^{-1}) has a slope of $\Gamma \approx 1.7$ and is visible at least up to 10 keV. A consistent interpretation of these data is that, the brighter the source the less steep is the photon index and the higher is the energy up to which the SP is visible above the hard power-law component. Although the strength and shape of the SP in the three sources is different it exhibits one common property: it undergoes large changes in flux without apparent changes in the photon index.

The III Zw2 data suggests that we are probably observing Compton up-scattered X-ray emission from the base of a relativistic jet (§3.4.3) and as such the constant spectral index of $\Gamma \approx 1.7$ can be attributed to the population of up-scattering synchrotron electrons. Observations of broad line emission (O VIII, Fe K_α) in NGC 4051 and MCG-2-58-22 suggests that we are observing emission from an accretion disk which is illuminated by X-ray source/s from above (i.e. some kind of a corona). The two phase disk-corona model (Haardt et al. 1996) predicts that flux variations with a constant spectral index can occur in a pair dominated corona if the variations in

flux are within a factor of ~ 2. However, the observed 6−fold flux variations in NGC 4051 over short time-scales and in MCG-2-58-22 over long time-scales argue against the presence of a pair dominated corona in these sources and suggests and some mechanism other than pair balance is probably responsible for the constant spectral index. The presence of a pair dominated corona in Seyfert galaxies is also not supported by high energy observations (OSSE) which show spectral breaks or cutoffs in the hard X-ray spectra of some galaxies at $\sim$ few 100 keV and instead favour thermal or quasi-thermal Comptonisation models for X-ray production (Zdziarski et al. 2000, Maisack et al 1993, Cameron et al. 1992).

The X-ray emission in NGC 4051 and MCG-2-58-22 is very different on short time-scales of $\sim$ few 10^3 s. NGC 4051 displays large amplitude (7-fold), rapid and sometimes non-linear X-ray variability (Green et al. 1999) (suggestive of turbulent processes like magnetic flares), while the X-ray emission in MCG-2-58-22 is relatively unvarying exhibiting $< 30\%$ flux variations. This suggests that either the origin of the X-ray emission in the two sources is different or that the X-ray emitting region in MCG-2-58-22 is so large that it washes out any rapid variability. The $XMM - Newton$ data for both NGC 4051 and MCG-2-58-22 favour the model in which X-ray sources are located close to the disk surface i.e. active regions (Haardt et al. 1994, Nayakshin 1998) suggesting a common origin. The black hole mass estimate for MCG-2-58-22 (10^9 $M_\odot$, §4.5.3) is much higher than that for NGC 4051 (10^{6-7} $M_\odot$, §5.4.4) which is suggestive of a larger X-ray emitting region in MCG-2-58-22 compared to NGC 4051 (Green et al. 1993, Saxton et al. 1993). MCG-2-58-22 exhibits broad line emission from highly ionised iron indicating the presence of a heavily ionised accretion disk. Since the ionisation state of the disk is governed by the intensity of the X-ray irradiation from above it is likely that the X-ray emitting region/s in MCG-2-58-22 is/are indeed also stronger than those in NGC 4051 (which displays line emission from neutral iron). The two phase model predicts a higher coronal temperature for MCG-2-58-22 ($kT \approx 100$ keV, for $\Gamma \approx 2$) than for NGC 4051

($kT \approx 40$ keV, for $\Gamma \approx 2.5$)(Haardt et al 1997). This suggests that the luminous X-ray source MCG-2-58-22 has larger, stronger (in intensity) and hotter X-ray emitting regions compared to the lower luminosity source NGC 4051.

6.2.2 The hard power-law component

Hardening of the X-ray spectrum in AGN at higher energies was observed in the late 80s by observatories such as GINGA which allowed for low resolution spectroscopy in the 2–20 keV band (Nandra 1991, Matsuoka et al. 1990). In the light of increasing evidence in favour of an X-ray illuminated accretion disk (observations of simultaneous variability in UV lines and X-ray continuum, Clavel et al. 1992), in a low ionisation state (observations of Fe K_α lines at 6.4 keV, Nandra et al. 1991, Matsuoka et al. 1990, Pounds et al. 1989), in the inner regions of AGN, the hard X-ray spectrum was interpreted in terms of Compton reflection from the surface of the disk which gives rise to the Fe K_α line and a broad hump peaking at $\sim 20-30$ keV which causes the observed spectral hardening at energies $\gtrsim 10$ keV (Lightman & White 1988, George & Fabian 1991).

The Compton reflection model has had moderate success in reproducing the high energy (relatively low signal to noise) spectra of Seyfert 1 galaxies obtained with observatories such as GINGA, BeppoSAX and RXTE . However, due to the lack of data below 2 keV and the relatively low sensitivity of these detectors, neither the intrinsic power-law slope nor the reflected spectrum could be well constrained. The relatively low measurement accuracy of these data means that a definitive comparison between theory and observations could not be made. Also, although the model provides a theoretically self-consistent explanation for the iron emission line, absorption edge and the hard tail, the models (in XSPEC) commonly used to fit data (PEXRAV, PEXRIV) do not include a self consistent prescription for all three components. Almost all previous results accounting for the hard tail with Compton reflection needed the addition of an iron line separately and hence it is

difficult to ascertain if the material producing the spectral 'hump' and absorption edge could also produce the emission line of observed strength and vice versa and the self-consistency of these results is uncertain.

The high signal to noise, sensitivity and wider energy range of the XMM-Newton detectors have allowed simultaneous measurements of both the soft and hard spectral components in AGN with much higher accuracy than was possible with previous detectors. The $XMM - Newton$ data provides a much tighter constrain on the measured spectral components and shows that the spectral hardening in the radio quiet Seyfert I galaxies studied in this thesis (NGC 4051 and MCG-2-58-22) cannot be completely accounted for by Compton reflection from a face on disk. I have significantly detected ($> 4\sigma$ level) a hard power-law component at higher energies in addition to the luminous steep power-law dominant at lower X-ray energies in the two sources. Although the origin of the hard power-law is not clearly understood, the almost unvarying nature (over 103 ks) of both the hard power-law flux and the relativistic Fe K_α line in NGC 4051, a similar decrease (factor of 10) in their flux over time-scales of years and their continued presence during the low states when the variable components have disappeared (or drastically reduced) suggests that it is probably associated with the nuclear regions (§5.4.2).

In recent years X-ray timing studies have shown that AGN and Galactic Black Hole Candidates (BGHCs) have similar shaped power density spectra which scale with the mass/luminosity of the object (Uttley et al. 2001). The power spectra in both classes of objects show a flattening at lower frequencies (Mchardy et al. 1998, Edelson & Nandra 1999) and a spectral break at higher frequencies (Nowak & Chiang 2000). The results of my spectral analysis, i.e. the low ($\approx 25\%$) flux contribution of the hard power-law to the 0.3−10 keV energy range as observed in NGC 4051 and MCG-2-58-22 and the relatively constant nature of the hard power-law inferred from the time resolved X-ray spectroscopy of NGC 4051, has close parallels with the results of timing studies which also suggest the presence of a constant component contributing $\sim 25\%$ of the total flux in the light-curves of black hole candidates and

X-ray binaries (Uttley & McHardy 2002). The observed similarities between AGN and GBHCs suggests that the central engines in accreting black holes may not be very different and as such there probably exists some fundamental energy production mechanism/s which is/are common to the nuclear regions of these objects.

6.3 Soft X-ray emission lines

Although line emission from medium-Z elements at soft X-ray energies due to re-processing of the illuminating power-law emission by the disk, has been predicted by reflection models over the years (George & Fabian 1991, Nayakshin et al. 2001, Ballantyne et al. 2001), it was only after the launch of high resolution detectors like $XMM-Newton$ that prominent broad emission line-like features were detected in the X-ray spectra of AGN. In the case of Mrk 766 and MCG-6-30-15 these features have been interpreted in terms of relativistically broadened emission lines from H-like oxygen, nitrogen and carbon by Branduardi-Raymont (2001) but instead as complex absorption by Lee et al. (2001) in MCG-6-30-15 using *Chandra* HETG data (E > 0.5 keV). Although the relativistic lines versus the dusty warm absorber debate is still ongoing, recent studies have shown that the relativistic line plus warm absorber interpretation provides a far superior fit to the RGS data compared to the dusty warm absorber model both in terms of narrow absorption lines and the overall spectral profile (Sako et al. 2002, Mason et al. 2003). One of the strongest arguments in favour of the relativistic line model for the soft X-ray lines is the observed consistency between the low energy line profiles and the Fe K_α profile (this study, Branduardi-Raymont 2001, Mason et al. 2003).

Apart from Mrk 766 and MCG-6-30-15 relativistic soft X-ray lines have been detected in only three more Seyfert galaxies namely, MCG-2-58-22 (Chapter 4), NGC 4051 (Chapter 5)and NGC 5548 (Kaastra et al. 2000). Soft X-ray spectra of Mrk 766, MCG-6-30-15 and NGC 5548 display line emission from O VIII, N VII and C VI while only an O VIII line is observed in the X-ray spectra NGC 4051 and

MCG-2-58-22. Emission from H-like oxygen is the strongest and is observed in all 5 sources (see Table 6.1).

Source		O VIII				
Name	L_{2-10} (erg s^{-1})	emissivity (q)	redshift z	L_{OVIII} ph s^{-1}	EW (eV)	reference
MCG-2-58-22	3×10^{44}	$3.1^{+0.5}_{-0.8}$	0.04732	$\sim 2.3\times10^{51}$	15±5	1
NGC 5548	4×10^{43}	3.9^{f}	0.01676	$\sim 7.8\times10^{50}$	20	4
Mrk 766	7×10^{42}	3.66±0.22	0.01293	$\sim 1.3\times10^{51}$	141±9	2,3
MCG-6-30-15	6×10^{42}	4.49±0.15	0.00775	$\sim 1.3\times10^{51}$	162±8	2, 3
NGC 4051	5×10^{41}	$6.22^{+0.17}_{-0.11}$	0.00234	$\sim 7.0\times10^{49}$	70±6	1

1 This study

2 Branduardi-Raymont et al. 2001

3 Sako et al. 2003

4 Kaastra et al. 2002

f fixed

Table 6.1: Comparison of O VIII line parameters in sources of different luminosities.

The luminosity of the O VIII line shows a general increase with source continuum luminosity (Table 6.1). A comparison of the derived emissivity index of the O VIII line suggests that as the source luminosity increases the line emission occurs over a wider region of the inner disk (Table 6.1). In Mrk 766 a decrease in the source flux results in a decrease in soft X-ray line intensities (Mason et al. 2003). Similarly, in NGC 4051 the O VIII line flux and steep power-law flux show related variations. The observed coupling between the soft X-ray lines and the power-law flux suggests that line emission arises from regions of the disk in close proximity to the variable X-ray sources. If this is the case, the increase in the O VIII line emitting region (as indicated by the measured line emissivity index) with source luminosity

is interpretable in terms of a larger spatial extent of the variable X-ray sources in more luminous AGN.

If the features observed at low X-ray energies are indeed broad emission lines from medium-Z elements they provide further evidence in favour of an accretion disk surrounding a central black hole in the nuclear regions of AGN. As such they could prove to be valuable probes of the density and ionisation structure of the disk. Theoretical spectra from ionised accretion disks have been studied by several authors in the past (Ross & Fabian 1993, Nayakshin & Kallman 2001, Ballantyne et al. 2002). Although the details of the individual model calculations differ from each other they all predict hydrogen-like emission lines from medium-Z elements in addition to the Fe K$-\alpha$ line emission. Also almost all reflection models predict the Lyα O VIII line to be the strongest of the soft X-ray emission lines (Ross & Fabian 1993, Nayakshin & Kallman 2001, Ballantyne et al. 2002) which is in agreement with *XMM − Newton* observations (this study, Branduardi-Raymont et al. 2001, Sako et al. 2002, Kaastra et al. 2002). This is encouraging and instills confidence that we have at least a basic understanding of the structure and physics of accretion disks.

However, the details of the mechanisms underlying soft X-ray line emission is yet unclear and highly controversial. The results of model calculations of theoretical spectra from ionised accretion disks are sensitive to the assumed ionisation structure of the disk (which is not well understood and for which there are almost no observational constrains available) and as such differ substantially from one model to another (Sako et al. 2003, Ballantyne &Fabian 2001, Nayakshin et al. 2001). Reflection models by Ballantyne & Fabian 2001) predict substantial Fe L line emission which is not observed. The predicted equivalent width for the O VIII line (EW $\sim$ 10 eV) is consistent with that observed in MCG-2-58-22 and NGC 5548 (EW $\sim$ 20 eV) but is much smaller than that observed in MRK 766, MCG-6-30-15 and NGC 4051 (70−160 eV). The Nayakshin et al. (2001) model successfully reproduces the equivalent widths of the O VIII lines in NGC 4051 and MCG-2-58-22. The model

by Sako et al. 2002 however, predicts negligible Fe L line emission and O VIII line equivalent width of a few hundred eV as found in MCG-6-30-15 and Mrk 766.

The *XMM – Newton* and *Chandra* data have provided us with a wealth of information in the soft X-ray band. However, the current reflection models although improved, lack the sophistication to fully exploit the diagnostic potential of the high resolution, high signal to noise data. The ability of the reflection models to predict soft X-ray lines demonstrates a fair understanding of the accretion disk physics. However, the finer details are still not within our grasp, mainly due the dearth of vital information on the ionisation structure and metallicity of accretion disks. The high resolution data provide a unique opportunity to invert this problem and use the soft X-ray spectra to gain information on the composition and state of accretion disks in AGN and to understand the properties of AGN accretion flows.

The real test of a model lies not just in its ability to reproduce the observed emission profile but in its ability to also properly account for the changes in the line profile over time. Spectral variability information can provide valuable observational constrains and help discriminate between various theoretical models. The correlated variations observed between the O VIII line and the soft power-law flux in NGC 4051 (Chapter 4) is compatible with the relativistic line model. The dusty warm absorber model is able to reproduce a part of the soft X-ray spectrum in MCG-6-30-15 (Lee et al. 2001) but it is not known if it can reproduce soft X-ray spectra of other AGN or if it is able to account for variations as those observed in the soft X-ray spectrum of MCG-6-30-15, Mrk 766, NGC 4051 etc. At present the relativistic line model does look more promising than the dusty warm absorber model. Although many questions regarding the soft X-ray features in AGN still remain unanswered, the *XMM – Newton* and *Chandra* data have made a substantial contribution to our understanding of soft X-ray emission in AGN and have taken us a step closer to unraveling the accretion disk phenomenon.

6.4 Iron line emission in Seyfert galaxies

6.4.1 Narrow Fe K_α lines

A strong narrow line at 6.4 keV with equivalent width consistent with that expected from reflection by dense, relatively cold neutral material (50−150 eV) is being detected in an increasing number of Seyfert galaxies ($L_{2-10} < 10^{45}$ erg s^{-1}; Pounds et al. 2002, Reeves 2002) with *XMM − Newton*. The intrinsic width of most of these lines, including the narrow line in MCG-2-58-22 (Chapter 4) is too narrow to be resolved by the EPIC detectors (typical FWHM resolution at 6.4 keV < 120 eV which corresponds to line velocity width (FWHM) < 5000 km s^{-1}) which suggests that they probably originate in neutral material distant from the inner disk region. Reflection by the molecular torus invoked in unified AGN theories has been proposed by several authors as the site of line emission, and in the absence of accurate measurements of the line velocity widths remains a strong candidate.

However, reflection from a Compton thick target like the molecular torus is expected to produce a substantial neutral edge along with the narrow Fe K_α. This is not observed in some sources (e.g. NGC 4051, Chapter 5) which casts doubts on the torus origin of the narrow line in these sources. A narrow Fe K_α emission line unaccompanied by a substantial absorption edge is indicative of reflection from a Compton thin target (Shields et al. 1995) and points towards the broad line clouds (which are expected to be Compton thin) as a likely origin. The narrow line in NGC 4051 (which is marginally resolved by the EPIC; Chapter 5) displays a velocity width of FWHM $\sim$ 13,000 km s^{-1} which is consistent with an inner BLR origin.

The unresolved narrow lines detected by EPIC have upper limits of FWHM < 10,000 km s^{-1} (Yaqoob et al. 2001) which indicates an origin in any one or more of these locations: the outer accretion disk, the broad line region (BLR), narrow line region (NLR) or the molecular torus. However, narrow lines in a handful of AGN have been recently resolved by *CHANDRA* HETG providing a slightly better constrain on their origin. The Fe K_α line in NGC 3783 has a velocity width of

FWHM $\sim$ 1700 km s^{-1} consistent with an origin in the outer BLR or the inner part of the torus (Kaspi et al. 2002) while those in NGC 5548 and MCG-6-30-15 display velocity width of FWHM $\sim$ 4500 km s^{-1} and FWHM $\sim$ 11,000 km s^{-1} respectively indicating an origin in the BLR or the outer edge of the disk (Yaqoob et al. 2001, Lee et al. 2002) . Although more precise measurements of the intrinsic line width and flux variability are required to better constrain the origin of narrow Fe K_α lines, the *XMM − Newton* and *Chandra* observations do suggest that the narrow Fe K_α lines in AGN may be emitted over a wide spatial region, from the outer disk and broad line region to the molecular torus (Kaspi et al. 2002, Yaqoob et al. 2001, Lee et al. 2002, Chapter 4). If this is the case they have the potential to provide valuable information on the distribution of dense neutral material in the inner regions of AGN.

A narrow line at 6.4 keV is far less common in high luminosity sources ($> 10^{45}$ erg s^{-1}, Pounds et al. 2002, Reeves 2002) and is also not detected in the X-ray spectra of III Zw2 ($L_{2-10} \approx 10^{45}$ erg s^{-1}; Chapter 2). One possible explanation is the relative dearth of neutral material in the vicinity of high luminosity sources probably due to the reduction in the covering fraction of the BLR. Or alternately, if the lines arise from the torus, their absence could be interpreted as circumstantial evidence in favour of the torus being flattened by radiation pressure as suggested by some authors (Konigl & Kartje 1994).

6.4.2 Broad Fe K_α lines

A broad excess around 6 keV is commonly observed in the X-ray spectra of Seyfert galaxies. This broad feature is generally interpreted as iron line emission or as Compton reflection. Recently complex absorption has also been proposed as an origin for the observed broad spectral feature around 6 keV (Kinkhabwala et al. 2002).

Iron emission

A broad iron emission line can be produced due to blending of narrow lines, or by broadening of an intrinsically narrow line as a result of Comptonisation in a surrounding medium or relativistic effects from a region of extreme gravity.

- *Blend of narrow lines* : The presence of iron in different stages of ionisation can result in narrow line emission between 6.4−6.97 keV which can appear as a broad profile in low resolution spectra. Since there are no known abundant elements that emit in the 3−6 keV region this model cannot account for the observed red wing of the Fe K_α line which requires emission below 6.4 keV. Skibo et al. (1997) have suggested that spallation of iron nuclei by high energy photons (> 10 MeV) could result in increased abundance of sub-Fe elements like Ti, V, Cr and Mn giving rise to a collection of fluorescence emission lines just below 6.4 keV. The unresolved emission from these elements could account for the observed Fe K_α red wing in Seyfert spectra. There are serious doubts about the plausibility of this model mainly because the spallation process would require a very high degree of efficiency and also the variations in broad line profiles observed in several sources would require all the fluorescence lines to vary simultaneously which is very unlikely (Fabian et al. 2002, Nandra 1999).

- *Comptonisation* : Czerny, Zbyszewska & Raine (1991) suggested that an intrinsically narrow line can be broadened by Compton down-scattering in a surrounding cool medium ($kT < 0.25$) of high optical depth ($\tau \sim 5$). Fabian et al. (1995) argued against this model on the basis that the Comptonising medium would have to be closer than 50 Schwarzschild radii from a $10^7 M_\odot$ black hole and at this small radius gravitational effects would anyway override effects of Comptonisation. Also the temperature of this medium would have to be larger than the proposed 0.25 keV. This model was developed further by Misra & Khembhavi (1998) but it still had one major drawback. Since

the power-law continuum emission would also pass through any Comptonising cloud present it would also get down scattered through multiple scatterings by the Comptonising medium and a spectral break would be expected at $\sim$ 30 keV. Such a break is not observed in Seyfert galaxies (Guainazzi et al. 1999, Zdziarski et al. 1995).

- *Relativistic broadening* : A narrow line can be broadened by gravitational and Doppler energy shifts in the vicinity of a black hole (Laor 1991, Fabian et al. 1989). The interpretation that we are observing effects of extreme gravity from the immediate vicinity of a super-massive black hole accreting via an accretion disk may be bold, but this model has been able to reproduce the observed line profiles in Seyfert galaxies remarkably well and has withstood the test of time, unlike some of the alternate hypothesis discussed above. In fact the skewed line profile in MCG-6-15-30 with its extreme red extension is very difficult to explain without relativistic effects from around a black hole.

Doppler and gravitationally broadened iron lines from the surface of an accretion disk is now the most widely accepted explanation for the broad excess around 6 keV observed in X-ray spectra of Seyfert galaxies. Detection of broad emission lines is also one of the strongest pieces of evidence we have in favour of the existence of black holes fueled by accretion disks at the center of AGN. A broad excess around iron line energies is observed in the XMM-Newton spectra of all three AGN studied in this thesis. The excess in the radio-quiet Seyfert galaxies MCG-2-58-22 and NGC 4051 is best fit by an emission line profile from an accretion disk around a black hole. Although the disk emission line models do reproduce the broad excess in III Zw2 they yield energies much higher than the line center energies of iron emission. Contribution of unresolved, Doppler shifted iron emission from the base of relativistic jets and/or ejecta in addition to disk emission could be one possible explanation for the observed high line energy in III Zw2 (chapter 3).

The Fe K_α profile in low luminosity radio-quiet source NGC 4051 ($L_{2-10} \approx 10^{41}$ erg s^{-1}; Chapter 5) shows an extended red wing, a prominent narrow component at 6.4 keV and little flux blue-ward of 6.4 keV. The line emission in higher luminosity radio-quiet source MCG-2-58-22 ($L_{2-10} \approx$ few 10^{44} erg s^{-1}; Chapter 4) shows a weaker red wing, relatively more flux blue-ward of 6.4 keV and a weaker narrow core compared to NGC 4051. The Fe K_α line emission in the luminous quasar (with relativistic jets), III Zw2 ($L_{2-10} \approx$ few 10^{45} erg s^{-1}; Chapter 3) shows a strong blue wing extending down to almost 7.6 keV (in the source rest frame $z = 0.089$; Chapter 3), a relatively weak red wing (similar to that seen in MCG-2-58-22) and no evidence for a narrow line at 6.4 keV (EW $<$ 48 eV). These observed changes in the Fe K_α line profile with source luminosity are in good agreement with the results of Nandra et al. 1997.

A decrease in equivalent width with increasing source luminosity, the 'X-ray Baldwin effect' in AGN was first suggested by Iwasawa & Taniguchi 1993 and later confirmed by Nandra et al. 1997, who found a strong anti-correlation between the source luminosity and equivalent width of both the narrow component at 6.4 keV and the broad disk component. The study of the narrow line at 6.4 keV in NGC 4051, MCG-2-58-22 and III Zw2 shows that the line is weaker in sources of higher luminosity. Although, the broad iron line emission in the higher luminosity radio-quiet Seyfert MCG-2-58-22 is weaker than than observed in the low luminosity radio-quiet Seyfert NGC 4051, the equivalent width of the iron line (EW $\sim$ 800 eV; Chapter 3) in the luminous quasar with relativistic jets, III Zw2 (the brightest of the three sources studied in this thesis) is comparable to that observed in the NGC 4051 (the lowest luminosity source studied in this thesis), which cannot be reconciled with the X-ray Baldwin effect. However, contribution from relativistic jets to the iron line emission could be responsible for the observed high equivalent width in III Zw2.

The broad iron line emission in NGC 4051 is neutral and shows a highly extended red wing, a signature of extreme relativistic effects, which suggests the presence of a

rotating (Kerr) black hole at the center of this galaxy. The derived emissivity index for the Fe K_α line emission is high ($q \sim 7$; Chapter 5) and suggests that most of the emission arises from regions very close to the black hole. The broad line emission in the more luminous source, MCG-2-58-22, is from highly ionised iron (indicating the presence of a very ionised disk) and displays a relatively weaker red wing. This suggests that either the line emission in MCG-2-58-22 is subject to lesser relativistic distortions (i.e. the central black hole in MCG-2-58-22 is non-rotating) or that, this galaxy too, has a Kerr black hole at its center, but the stronger X-ray irradiation of the disk, probably ionises the iron atoms completely in the innermost regions (which would give rise to the extreme red wing), which causes most of the extended red tail to disappear. The current XMM-Newton data cannot resolve this issue. The smaller derived emissivity index ($q \sim 3$) for the Fe K_α line emission in the more luminous source MCG-2-58-22, suggests that the line emission arises over a wider area of the inner disk compared to the low luminosity source NGC 4051.

Compton reflection

ASCA observations had indicated that broad iron lines were a common feature in the X-ray spectra of Seyfert galaxies. However, Lubiński & Zdziarski. 2001 have suggested that the the Fe K_α lines in AGN detected by ASCA are probably not as broad and strong as had been previously thought. Although this claim has been strongly disputed by Yaqoob et al. 2001, the detection of gravitationally broadened iron lines in relatively few sources with XMM-Newton has raised doubts about the interpretation of the excess around 6 keV. The presence of broad Fe K_α lines in the $XMM-Newton$ spectra of significant number of sources is currently under dispute mainly because the excess around iron line energies can also be adequately described by reflection and/or an absorption of primary X-rays (Pounds & Reeves 2002, Page, Davis & Salvi. submitted). However, this interpretation cannot account for the broad excess observed around 6 keV in the X-ray spectra of all three AGN studied in this thesis.

Strong narrow lines are now observed in a majority of Seyfert 1 galaxies either superimposed on to an underlying broad profile or by themselves. The observed profile of a strong narrow line at 6.4 keV on top of a broad underlying feature with a dip at $\sim$ 7 keV closely resembles a reflection plus absorption spectrum (George & Fabian 1991) and has been interpreted as such by some authors or as a relativistically broadened Fe K_α line with a blue cut-off near 7 keV underlying a narrow Fe K_α line by others. The reflection plus absorption interpretation however, does provide a simpler and self consistence (although not necessarily correct) explanation for the X-ray spectrum above 3−4 keV and hence warrants a thorough examination.

The key to proper identification of the broad excess as a red wing of the Fe K_α line or reflection lies in the ability to discriminate between the blue cut-off of the broad emission line and an absorption edge, which highlights the importance of correctly fitting the data around 7 keV. Proper identification of features in this energy range is made even more difficult by the presence of high ionisation Fe K_α and Fe K_β emission and/or absorption lines. The X-ray spectra of some sources do show some visual indication of absorption above 7 keV, however, it must be remembered that complicated emission features can be mistaken for absorption edges in lower resolution spectra as has been revealed in the low energy spectrum by the high resolution RGS data (e.g. O VII and O VIII edges). The sensitivity of XMM-Newton in the iron K-band is not high enough to resolve these issues.

Complex absorption

The presence of absorbing material in our line of sight has been clearly revealed by the narrow emission and absorption features observed in the RGS spectra of Seyfert galaxies. Until recently, line of sight absorbing material was not thought to affect the spectrum above 3 keV, however, the latest warm absorber model put forth by Kinkhabwala (2002) shows otherwise. This model incorporating all ionisation states of all elements has shown that complex absorption by several species of different

elements can account for all the observed features in the X-ray spectrum of MCG-6-30-15 including the soft excess and characteristic broad Fe K_α profile. Although the interpretation is challenging the preliminary results do look very promising. However, it remains to be seen if the model can reproduce other X-ray spectra and account for the variability patterns observed across the wide X-ray band from 0.3−10 keV.

Apart from the complex absorption model (which is still work in progress) none of the alternate models really seem to challenge the accretion disk model. Although the RGS data have proven without doubt the presence of a warm absorber and its ability to substantially modify features in the intrinsic soft X-ray spectrum, the claim that all the observed features in the broad 0.3−10 keV spectral range are a result of complex absorption is also equally bold and requires critical investigation.

Also there are several issues that need to be studied in detail before the fate of broad iron lines in *XMM − Newton* spectra can be decided. Although initial *XMM − Newton* observations have indicated the absence of broad lines in a significant number of sources, it is worth noting that very long observations have been available for only a handful of sources and a broad Fe K_α line has been detected in almost all of them. Hence it is possible that the broad lines in some sources are weak and hence were not detected during the relatively short exposures. Long observations of sufficient number of sources are required before any decision can be made about the absence of broad iron lines in *XMM − Newton* spectra. Also, of the broad lines detected by *XMM − Newton*, a significant fraction lie at energies of highly ionised iron indicating the presence of ionised disks in an increasing number of sources. Hence it is also possible that the inner disks in some sources are very hot and ionised to the point where most of the iron is fully stripped resulting in no Fe K_α emission. Clearly we need to properly interpret the information that *XMM − Newton* has provided us.

We can certainly look forward to exciting times ahead regarding the interpretation of spectral features in the XMM-Newton data. The issue of broad Fe K_α

lines however, is still open and it remains to be seen if XMM-Newton can provide conclusive evidence either in favour or against the presence of broad lines in the X-ray spectra of AGN in the near future.

6.5 Do AGN have fundamentally similar central engines ?

Although III Zw2 exhibits huge radio flares the properties of its X-ray and radio emission are not typical of radio-loud AGN and instead are an intriguing mix of those observed in radio-quiet and radio-loud objects. Its power-law X-ray emission with $\Gamma = 1.7$ and the absence of a soft X-ray excess (Chapter 2) is consistent with observations of RL sources (Williams et al. 1992, Lawson et al. 1992) while its substantial reflection component and strong broad iron line (Chapter 2) is unlike that seen in radio-loud AGN (Williams et al. 1992, Nandra et al. 1997). The variability amplitude (20-fold) of the radio emission in III Zw2 is much larger than that observed in typical blazars like 3C 279. However, its radio–optical flux density ratio $R \sim 200$ (Falcke et al. 1999) is much lower than that of RL AGN (~ 2000) and its extended radio flux density is too weak for it to be a radio galaxy (Unger et al. 1987). RL AGN are generally found in elliptical galaxies while the spiral host galaxy and the shape and luminosity of the extended radio emission in III Zw2 is typical of radio-quiet Seyfert galaxies. The curious dichotomy at radio wavelengths has lead Falcke et al. (1999) to suggest that III Zw2 may be a radio-intermediate quasar i.e. radio-quiet quasar with relativistic jets pointed towards the observer.

The observed broad band emission properties of III Zw2 lend support to the idea that both radio-loud and radio-quiet AGN may have fundamentally similar central engines which power nuclear relativistic jets with the difference being, that in the case of radio-loud AGN some (poorly understood) combination of factors (host galaxy type, black hole mass, accretion rate, black hole spin, etc) leads to the

formation of parsec scale jets which are so powerful that they are detected at any orientation angle of the source while in radio-quiet AGN the nuclear jets are weak and small (sub parsec) and can go undetected unless the jets are pointed straight towards the observer. It is also possible that AGN evolve from being radio-loud to radio-quiet (or vice-versa) with sources like III Zw2 probably in the middle of the transitional period.

If this unified AGN picture is correct we should also find some evidence for nuclear relativistic jets (although pointing away from us) in the two radio-quiet Seyferts studied in this thesis. MCG-2-58-22 shows a compact, high brightness flat spectrum radio core (similar to III Zw2) with weak east-west extensions. Such flat spectrum cores are interpreted as self absorbed synchrotron radio emission from the base of a relativistic jets (Mundell et al. 2000). NGC 4051 also shows evidence for a compact radio triple source with a flat spectrum core and collimated ejection on a scale less than 40 pc along with extended radio emission. Christopoulou et al. (1997) have suggested that the extended radio emission could be a continuation of the centrally collimated flows, a scenario somewhat similar to that observed in Fanaroff-Riley I radio galaxies but on a weaker scale.

This is encouraging and does lend support for the hypothesis that the central engines in Seyfert galaxies are probably not intrinsically different. In sources like III Zw2 where the relativistic jets are pointed straight towards the observer the observed broad band emission is likely to be dominated by emission from the jet which overwhelms emission from all other sources. In sources like MCG-2-58-22 and NGC 4051 where the weak relativistic jets are not encountered face-on, emission from other sources like the accretion disk, corona and dust is visible and dominates the observed energy output.

Chapter 7

Conclusions

To understand the central engines in AGN I have studied the X-ray spectra and multi-wavelength variability of 3 observationally very different AGN: a radio−intermediate quasar III Zw2, a luminous radio-quiet Seyfert 1 galaxy MCG-2-58-22 and a low luminosity narrow line Seyfert 1 galaxy NGC 4051. This study has uncovered further complexities in the X-ray emission of Seyfert galaxies, revealing probably some of the fine structure in the widely accepted AGN paradigm.

As observed at radio wavelengths, the X-ray emission in III Zw2 also shows properties of both radio-loud and radio-quiet AGN which lends support to the hypothesis of Falcke et al. (1999) that III Zw2 is probably a radio-quiet quasar with relativistic jets pointed towards the observer i.e. a radio-intermediate quasar.

The 0.3−10 keV X-ray continuum in III Zw2 can be described by a power-law of $\Gamma \approx 1.7$ and Compton reflection. The radio to optical spectral energy distribution mimics a typical synchrotron spectrum: self-absorbed at low energies (radio/millimeter), power-law over a broad wavelength range and a cut-off at high energies. Multi-wavelength light curves show related variations variations from the radio the X-rays. I interpret the radio to optical emission as synchrotron radiation, self absorbed in the radio/millimeter region and the X-rays as mainly due to Compton up-scattering of low energy photons by the population of high energy electrons that give rise to the synchrotron radiation.

The X-ray continuum in the radio-quiet Seyfert galaxies MCG-2-58-22 and NGC 4051 displays significant curvature. The *XMM − Newton* data reveal that the steeper soft X-ray spectrum is not a black body nor can the broad band X-ray continuum be successfully described by a simple power-law plus Compton reflection from a face-on disk. The continuum can, however, be successfully modeled with 2 power-laws plus Compton reflection. The steeper luminous power-law ($\Gamma = 2-2.5$) contributing typically 75% of the flux in the 0.3−10 keV range is superimposed on to a harder component (Γ =1−1.3), indicating the presence of two different electron scattering regions in the inner regions of Seyfert galaxies.

The luminous steep power-law undergoes large variations in flux (over time-scales of a few 10^3 s in NGC 4051 and a few years in MCG-2-58-22) maintaining an almost constant photon index. The power-law X-ray emission in the III Zw2 also exhibits similar behaviour over time-scales of years. The strength and dynamic nature of this component certainly associates it with regions close to the black hole. Study of X-ray emission in NGC 4051 shows that the hard power-law is relatively unvarying in flux and photon index over time-scales of days. The close parallels between the observed behaviour of the hard power-law and the broad Fe K_α line in NGC 4051 suggests that it is probably also associated with the nuclear regions.

Observations over small energy ranges, spanning just the soft (E < 2 keV) or hard (E > 2 keV) bands, cannot disentangle the complexities in the X-ray continuum. Time resolved X-ray spectroscopy of NGC 4051 has shown that modeling spectra over the 2−10 keV band gives rise to photon index−flux correlations and other effects like saturation of photon index at high luminosity, which are probably artifacts of modeling the spectra with a single power-law in this particular energy range and may not necessarily indicate a physical change in the properties of the X-ray emitting region.

Broad O VIII and Fe K_α lines are detected in the X-ray spectra of the two radio-quiet Seyfert galaxies NGC 4051 and MCG-2-58-22. The detection of broad O VIII emission lines with profiles consistent with those of broad Fe K_α lines, provides

further support in favour the AGN paradigm, of a black hole surrounded by an X-ray illuminated accretion disk. A broad excess between 5.5−7.5 keV is also observed in the X-ray spectra of III Zw2. However, this emission cannot be entirely explained in terms of Fe K_α emission from a low inclination relativistic disk and may contain contribution from the base of a relativistic jet and/or ejecta.

The *XMM−Newton* data for MCG-2-58-22 and NGC 4051 favour the geometry in which the accretion disk is unevenly illuminated by X-ray sources close to its surface. The derived emissivity indices (q) for the O VIII and Fe K_α suggests that the line emission arises over a wider region of the inner disk in higher luminosity sources, perhaps an indication of a larger spatial extent of the X-ray emitting sources in more luminous sources (since the coupling of the O VIII line flux and the soft power-law flux in NGC 4051 suggests that the line emission arises from regions in close proximity to the variable X-ray sources).

The iron line emission in the radio-quiet Seyfert galaxies (studied here) consists of a narrow core at 6.4 keV superimposed on to a broader component. The narrow line is weaker in more luminous sources. The 6.4 keV line in NGC 4051 displays a large velocity width indicating an origin much closer than the torus, possibly within the BLR. The narrow line in MCG-2-58-22 is unresolved by EPIC which indicates an origin anywhere between the outer edge of the disk and torus.

The broad Fe K_α line emission in the low luminosity source NGC 4051 is from ionisation states < Fe XVI and shows an extreme red extension indicating the presence of a neutral or mildly ionised disk around a Kerr (rotating) black hole while that in MCG-2-58-22 is from heavily ionised species of iron ($\geq$ Fe XXV), a signature of a highly ionised accretion disk and perhaps an indication of stronger X-ray sources in more luminous AGN.

The hydrostatic balance reflection model for an accretion disk around a black hole can adequately reproduce both the broad Fe K_α and O VIII emission lines in MCG-2-58-22 and NGC 4051 in a self consistent manner along with the reflected continuum.

The X-ray emission in the low luminosity source NGC 4051 varies rapidly over time-scales of few 100 seconds while that in the higher luminosity sources MCG-2-58-22 and III Zw2 is relatively unvarying over time-scales of few 10^4 s, probably due to the presence of larger X-ray emitting regions in more luminous sources. The larger black hole mass estimates obtained by me for the higher luminosity sources MCG-2-58-22 (10^9 $M_\odot$) and III Zw2 (10^9 $M_\odot$) compared to NGC 4051 (10^7 $M_\odot$) lends support to this argument.

References

Abramowicz, M. A., Chen, X.-M., Granath, M., Lasota, J.-P, *Astrophys. J.*, **471**, 762

Allen, D. A., 1976, *Mon. Not. R. astr. Soc.*, **174**, 29P

Aller, H. D., Aller, M. F., Latimer, G. E., Hodge, P. E., 1985, *Astrophys. J., Supplement series*, **59**, 513

Andrews, D. 1984, *EXOSAT Express*, 3, 1

Antonucci, R., 1993, *Annual Reviews*, **31**, 473

Antonucci, R. R. J., Miller, J. S., 1985, *Astrophys. J.*, **297**, 621

Arnaud, K. A., Branduardi-Raymont, G., Culhane, J. L., Fabian, A. C., Hazard, C., McGlynn, T. A., Shafer, R. A., Tennant, A. F., Ward, M. J., 1985, *Mon. Not. R. astr. Soc.*, **217**, 105

Baldwin, J. A., Wampler, E. Joseph, Gaskell, C. Martin, 1989, *Astrophys. J.*, **338**, 630

Ballantyne, D. R., Ross, R. R., Fabian, A. C., 2002, *Mon. Not. R. astr. Soc.*, **336**, 867

Ballantyne, D. R., Iwasawa, K., Fabian, A. C., 2001, *Mon. Not. R. astr. Soc.*, **323**, 506

Ballantyne, D. R., Ross, R. R., Fabian, A. C., 2001, *Mon. Not. R. astr. Soc.*, bf327, 10

Ballantyne, D. R., Fabian, A. C., 2002, *Mon. Not. R. astr. Soc.,* **328**, L11

Ballantyne, D.R., Iwasawa, K., Fabian, A. C., 2001, *Mon. Not. R. astr. Soc.,* **323**, 506

Barr, P., White, N. E., Sanford, P., Ives, J. C., 1977, *Mon. Not. R. astr. Soc.,* **181**, 43

Barth, A. J., Filippenko, A. V., Moran, E. C., 1999, *Astrophys. J.,* **525**, 673

Barvainis, R., 1993, *Astrophys. J.,* **412**, 513

Bill Keel
http://www.astr.ua.edu/keel/agn/

Bleeker, J. A. M. 1975, *ESA X-Ray Astronomy and Related Topics*, **89**

Bloom, Steven D., Marscher, Alan P., 1996, *Astrophys. J.,* **461**, 657

Bloom et al., 1999, ApJ *Supplement series*, **122**, 1

Boella G., Chiappetti L., Conti G., et al., 1997 *Astr. & Astrophys., Supplement series* **122**, 327

Boller, T., Brandt, W. N., Fink, H., 1996, *Astr. & Astrophys.,* , 305, 53

Bon, E., C Popovic, L. Mediavilla, E. G., 2001, *Astronomische Gesellschaft Abstract Series*, **18**, 175

Böttcher, M., 2000, *GeV-TeV Gamma Ray Astrophysics Workshop*, eds,

Brandt, W. N. ,Mathur, S., Elvis, M., Boller, 1997, AAS, *Bulletin of the American Astronomical Society*, 29, 846

Branduardi-Raymont, G., Mason, K. O., Ogle, P. M., Page, M. J., Puchnarewicz, E. M., Behar, E., 2002, *Workshop on X-ray Spectroscopy of AGN with Chandra and XMM-Newton*, held at MPE Garching, December 3-6, 2001, MPE, **279**, 19

Branduardi-Raymont, G., Sako, M., Kahn, S. M., Brinkman, A. C., Kaastra, J. S., Page, M. J., 2001, *Astr. & Astrophys.,* **365**, L140

Brenda L. D., Michael H. S., David B.K., Melville, N.Y., **515**, 31

Bridle, A. H., Perley, R. A., 1984, *Annual review of astronomy and astrophysics*, **22**, 319

Briel, U. G., Pfeffermann, E., Hartner, G. Hasinger, G. 1988, in *X-ray instrumentation in astronomy II* Proceedings of the Meeting, San Diego, CA, 401

Brunthaler, A., Falke, H., Bower, G. C., Aller, M., Aller, H., Terrasranta, H., 2000, *Proceedings of the 5th european VLBI Network Symposium held at Chalmers University of Technology*, Sweden, Eds.: J.E. Conway, A.G. Polatidis, R.S. Booth and Y.M. Pihlstrm, 11

Brunthaler, A., et al. 2000, *Astr. & Astrophys.*, **357**, L45

Cameron, R. A., Grove, J. E., Johnson, W. N., Kroeger, R. A., Kurfess, J. D., Strickman, M. S., Jung, G. V., Grabelsky, D. A., Purcell, W. R., Ulmer, M. P., 1992, *American Astronomical Society*, **24**, 1237

Cappi, M., Mihara, T., Matsuoka, M., Hayashida, K., Weaver, K. A., Otani, C., 1996, *Astrophys. J.*, **458**, 149

Carleton, N. P., Elvis, M., Fabbiano, G., Willner, S. P., Lawrence, A., Ward, M., 1987, *Astrophys. J.*, **318**, 595

Carter, B. S., 1990, *Mon. Not. R. astr. Soc.*, **242**, 1

Chapman, G. N. F., Geller, M. J., Huchra, J. P. 1985, *Astrophys. J.*, **297**, 151

Choi, C-S., Dotani, T., Yi, I., Kim, C.H., 2002, astro-ph/0007195, submitted to *Astrophys. J.*,

Choi, C-S., Dotani, T., Chang, H-Y., Yi, I., 2002, *Journal of the Korean Astronomical society*, **35**, 1

Christopoulou, P. E., Holloway, A. J., Steffen, W., Mundell, C. G., Thean, A. H. C., Goudis, C. D., Meaburn, J., Pedlar, A., 1997, *Mon. Not. R. astr. Soc.*, **284**, 385

Clavel, J.,, Nandra, K., makino, F., Pounds, K. A., Reichert, G. A., et al. 1992, *Astrophys. J.,* **393**, 113

Clements, S. D., Smith, A. G., Aller, H. D., Aller, M. F. 1995, *Astr. J.,* **110**, 529

Collinge, M. J. et al., 2001, *Astrophys. J.,* **557**, 2

Condon, J. J., O'Dell, S. L., Puschell, J. J., Stein, W. A. 1981 *Astrophys. J.,* , **246**, 624

Czerny, B., Elvis, M., 1987, *Astrophys. J.,* **321**,305

Czerny, B., Zbyszewska, M., Raine, D. J., 1991, *ron Line Diagnostics in X-ray Sources, Proceedings of a Workshop Held in Varenna, Como, Italy*, Eds. Aldo T., Giulio C. P., and Luigi S., Springer-Verlag Berlin Heidelberg New York

Dabrowski, Y., Fabian, A. C., Iwasawa, K., Lasenby, A. N, Reynolds C. S. 1997, *Mon. Not. R. astr. Soc.,* **288**, L11

di Matteo, T., Fabian, A. C., Rees, M. J., Carilli, C. L., Ivison, R. J., 1999, *Mon. Not. R. astr. Soc.,* **305**, 492

de Robertis, M. 1985, *Astrophys. J.,* **289**, 67

de Vries, M., Kuijpers, J., 1992, *Astr. & Astrophys.,* **266**, 77

de Vaucouleurs, G., de Vaucouleurs, A., Corwin, H. G., Jr., Buta, R. J., Paturel, G., Fouque, P., 1991, *Third Reference Catalogue of Bright Galaxies*, 1, 7, Springer-Verlag Berlin Heidelberg New York

di Matteo, T., Fabian, A. C., Rees, M. J., Carilli, C. L., Ivison, R. J., 1999, *Mon. Not. R. astr. Soc.,* **305**, 492

den Herder, J. W., et al. 2001, *Astr. & Astrophys.,* L7

Done, C., Nayakshin, S., 2001, *Mon. Not. R. astr. Soc.,* **328**, 616

Done, C., Ward, M. J., Fabian, A. C., Kunieda, H., Tsuruta, S., Lawrence, A., Smith, M. G.; Wamsteker, W., 1990, *Mon. Not. R. astr. Soc.,* **243**, 713

Durret, F.,1989, *Astr. & Astrophys.*, **81**, 253

Edelson, R. A., Malkan, M. A. 1987, *Astrophys. J.*, **323**, 516

Edelson, R. A., Malkan, M. A., 1986, *Astrophys. J.*, **308**, 59

Edelson, R. A., nandra, K., 1999, *Astrophys. J.*, **514**, 682

Elvis, M., Wilkes, B. J., McDowell, J. C., Green, R. F., Bechtold, J, Willner, S. P., Oey, M. S., Polomski, E.,; Cutri, R., 1994, *Astrophys. J. Suppl.*, **95**, 1

Fabian, A. C., Vaughan, S., Nandra, K., Iwasawa, K., Ballantyne, D. R., Lee, J. C., De Rosa, A., Turner, A., Young, A. J., 2002, *Mon. Not. R. astr. Soc.*, **335**, L1

Fabian, A. C., Nandra, K., Reynolds, C. S., Brandt, W. N., Otani, C., Tanaka, Y., Inoue, H., Iwasawa, K., 1995, *Mon. Not. R. astr. Soc.*, **277**, L11

Fabian, A. C., Rees, M. J., Stella, L. & White, N. E. 1989, *Mon. Not. R. astr. Soc.*, **238**, 729

Fabian, A. C., Guilbert, P. W., Arnaud, K. A., Shafer, R. A., Tennant, A. F., Ward, M. J. 1986, *Mon. Not. R. astr. Soc.*, **218**, 457

Falcke, H, Nagar, N, M., Wilson, A. S., Ho, L. C., Ulvestad, J. S., 2001, *Black Holes in Binaries and Galactic Nuclei*, Proceedings of the ESO Workshop held at Garching, Ed. Lex K., Edward P. J. van den Heuvel, Patrick A. Woudt, 218. Springer.

Falcke, H., et al. 1999, *Astrophys. J.*, **514**, L17

Fanaroff, B. L., Riley, J. M., 1974, MNRAS **167**, 31P

Franceschini, A., Bassani, L., Cappi, M., Granato, G. L., Malaguti, G., Palazzi, E., Persic, M., 2000, *Astr. & Astrophys.*, **353**, 910

Frogel, J A., Gillett, F. C., Terndrup, D. M., Vader, J. P., 1998, *Astrophys. J.*, **343**, 672

Frontera F., Costa E., Dal Fiume D., et al., 1997, *Astr. & Astrophys., Supplement*

series **122**, 371

Georganopoulos, M., 2000, *Astrophys. J.,* **543**, L15

George, I. M., Fabian, A. C., 1991, *Mon. Not. R. astr. Soc.,* **249**, 352

Ghosh, K. K., Soundararajaperumal, S., 1992 *Astrophys. J.,* , **398**, 501

Giacconi, R., et al. 1979, *Astrophys. J.,* **230**, 540

Gondoin, P., Orr, A., Lumb, D., Santos-Lleo, M., 2002, *Astr. & Astrophys.,* **388**, 74

Grandi, P., Tagliaferri, G., Giommi, P., Barr, P., Palumbo, G. G. C., 1992, *Astrophys. J. Suppl.,* **82**, 93

Green, A. R., McHardy, I. M., Done, C., 1999, *Mon. Not. R. astr. Soc.,* **305**, 309

Green, A. R., McHardy, I. M., Lehto, H. J., 1993, *Mon. Not. R. astr. Soc.,* **265**, 664

Greenstein, J. L., Matthews, T., 1963, *Nature,* **197**, 1041

Guainazzi, M. et al., 1998, *Mon. Not. R. astr. Soc.,* **301**, L1

Guainazzi, M., Perola, G. C., Matt, G., Nicastro, F., Bassani, L., Fiore, F., dal Fiume, D., Piro, L., 1999, *Astr. & Astrophys.,* **346**, 407

Haardt, F, Maraschi, L, 1993, *Astrophys. J.,* **380**, L51

Haardt, F, Maraschi, L, 1993, *Astrophys. J.,* **413**, 507

Haardt, F., Maraschi, L., Ghisellini, G., 1994, *Astrophys. J.,* **432**, L95

Haardt, F, Maraschi, L, Ghisellini, G, 1997, *Astrophys. J.,* **476**, 620

Hall, R., Rickett, M. J., Page, C. G., Pounds, K. A. 1981, *Sp. Sci. Rev.,* **30, 47**

Harris, D. E., Stern, C. P., Biretta, J. A. 1990, *Imaging X-Ray Astronomy,* 299

Hartman & Impey
http://zeba.uoregon.edu/ js/ast123/lectures/lec15.html

Hazard, C., Mackey, M. B., Shimmins, A. J., 1963, *Nature,* **197**, 1037

Holland, W. S., et al. 1999, *Mon. Not. R. astr. Soc.,* **303**, 659

Huchra, J., Latham, D.W., da Costa, L. N., Pellegrini, P. S., Willmer, C. N. A., 1993, *Astr. J.,* **105**, 1637

Hyland, A. R., Allen, D. A. 1982, *Mon. Not. R. astr. Soc.,* **199**, 943

Inoue, H. 1990, *Proceedings, 23rd ESLAB Symp*, Ed. Hunt, J., Battrick, B., Paris: ESA, 783

Inoue, H. 1993, *Experimental Astronomy*, 4, 1

Iwasawa, K., Taniguchi, Y., 1993, *Astrophys. J.,* **413**, L15

Ives, j., Sanford, P., Penston, M., 1976, *Astrophys. J.,* **207**, L159

Jaffe, W., Ford, H., Ferrarese, L., van den Bosch, F., O'Connell, R. W., 1996, *Astrophys. J.,* **460**, 214

Jansen, F., et al. 2001, *Astr. & Astrophys.,* **365**, L1

Jang, M., Miller, H. R. 1997, *Astr. J.,* **114**, 565

Kaastra, J. S., de Korte, P. A. J. 1988, *Astr. & Astrophys.,* **198**, 16

Kaastra, J. S., Mewe, R., Liedahl, D. A., Komossa, S., Brinkman, A. C., 2000, *Astr. & Astrophys.,* **354**, L83

Kaspi, S. et al., 2002, *Astrophys. J.,* **574**, 643

Kawaguchi, T., Shimura, T., Mineshige, S., 2001, *Astrophys. J.,* **546**, 966

Kinkhabwala, A., 2002, *High Resolution X-ray Spectroscopy with XMM-Newton and Chandra, Proceedings of the international workshop held at the Mullard Space Science Laboratory of University College London*, Ed. Branduardi-Raymont, G.

Komossa, S., Fink, H., 1997, *Astr. & Astrophys.,* **322**, 719

Konigl, A., Kartje, J. F., 1994, *Astrophys. J.,* **434**, 446

Kotilainen, J. K., Ward, M. J., Williger, G. M., 1993 *Mon. Not. R. astr. Soc.,* **263**,

655

Krolik, J. H., McKee, C. F., Tarter, C. B. 1981, *Astrophys. J.*, **249**, 422

Kukula, Marek J., et al., 1998, *Mon. Not. R. astr. Soc.*, **297**, 366

Kunieda, H., Hayakawa, S., Tawara, Y., Koyama, K., Tsuruta, S., Leighly, K., 1992, *Astrophys. J.*, **384**, 482

Landau, R., Epstein, E. E., Rather, J. D. G. 1980, *Astr. J.*, **85**, 363

Laor, A., Fiore, F., Elvis, M., Wilkes, B. J., McDowell, J. C., 1997, *Astrophys. J.*, **477**, 93

Laor, A., 1991, *Astrophys. J.*, **376**, 90

Laor, A., Netzer, H., 1989, *Mon. Not. R. astr. Soc.*, **238**, 897

Lawrence, A.,Watson, M.G., Pounds, K.A., Elvis, M., 1987, *Nature*, **325**, 694

Lawrence, A., Papadakis, I., 1993, *Astrophys. J.*, , 414, L85

Lawson, A. J., Turner, M. J. L., Williams, O. R., Stewart, G. C., Saxton, R. D., 1992, *Mon. Not. R. astr. Soc.*, **259**, 743

Lawson, A., 1995, *The hard X-ray emission of AGN*, Ph.D Thesis, Univ. of Leicester

Lebofsky, M. J., Rieke, G. H., 1980, *Nature*, **284**, 410

Lee, Julia C., Iwasawa, Kazushi, Houck, John C., Fabian, Andrew C., Marshall, Herman L., Canizares, Claude R., 2002, *Astrophys. J.*, **570**, L47

Lee, J. C., Ogle, P. M., Canizares, C. R., Marshall, H. L., Schulz, N. S., Morales, R., Fabian, A. C., Iwasawa, K., 2001, *Astrophys. J.*, **554**, L13

Lightman, Alan P., White, Timothy R., 1988, *Astrophys. J.*, **335**, 57

Lloyd, C. 1984, *Mon. Not. R. astr. Soc.*, **209**, 697

Lobanov, A. P., 1998, *Astr. & Astrophys., Supplement series*, **132**, 261

Lubinski, P., Zdziarski, A. A., 2001, *Mon. Not. R. astr. Soc.*, **323**, L37

Magdziarz & Zdziarski 1995 *Mon. Not. R. astr. Soc.*, **273**, 837

Maisack, M., Johnson, W. N., Kinzer, R. L., Strickman, M. S., Kurfess, J. D., Cameron, R. A., Jung, G. V., Grabelsky, D. A., Purcell, W. R., Ulmer, M. P., 1993, *Astrophys. J.*, **407**, L61

Malkan, M. A., Sargent, W. L. W., 1982, *Astrophys. J.*, **254**, 22

Malkan, M. A., Filippenko, A. V., 1983, *Astrophys. J.*, **275**, 477

Maraschi, L., Chiappetti, L., Falomo, R., Garilli, B., Malkan, M., Tagliaferri, G., Tanzi, E. G., Treves, A., 1991, *Astrophys. J.*, **368**, 138

Markowitz, A., Edelson, R. 2001, *Astrophys. J.*, **547**, 684

Marscher, A. P., 1987, in *Superluminal radio sources*, ed. Zensus, J. A. and Pearson, T. J., (Cambridge:Cambridge Univ. Press), 280

Marshall N., Warwick R. S., Pounds K., 1981, *Mon. Not. R. astr. Soc.*, **194**,897

Masnou, J. L., Wilkes, B. J., Elvis, M., McDowell, J. C., Arnaud, K. A. 1992, *Astr. & Astrophys.*, **253**, 35

Mason et al., 2003, *Astrophys. J., in press*

Mathur, S., Kuraszkiewicz, J., Czerny, B., 2001, *New Astronomy*, **6**, 321

Matsuoka, M., Yamauchi, M., Piro, L., Murakami, T., 1990, *Astrophys. J.*, **361**, 440

Matt, G., Fabian, A. C., Ross, R. R., 1993, *Mon. Not. R. astr. Soc.*, **262**, 179

Matt, G., Perola, G. C., Piro, L. 1991, *Astr. & Astrophys.*, **247**, 25

Matthews, T. A., Sandage, A. R., 1963, *Astrophys. J.*, **138**, 30

Mayer, W. F. 1975, *APL Technical Digest*, **14**, 14

McAlary, C. W., McLaren, R. A., McGonegal, R. J., Maza, J. 1983, *Astrophys. J., Supplement series*, **52**, 341

McHardy, I. M., Papadakis, I. E., Uttley. P., 1998, *The Active X-ray Sky: Results*

from BeppoSAX and RXTE, Ed. Scarsi, L., Bradt, H., Giommi, P., Fiore, f., Amsterdam: Elsevier, 509

McHardy, I. M. et al., 1999, *Mon. Not. R. astr. Soc.,* **310**, 571

Merloni, A., Fabian, A, C., 2002, to appear in Proceedings of the Symposium on *'New Visions of the X-ray Universe in the XMM-Newton and Chandra Era'*, 26-30 November 2001, ESTEC, The Netherlands

Merloni, A., Fabian, A. C., 2002, *Mon. Not. R. astr. Soc.,* **332**, 165

Merloni, A., Fabian, A. C., 2001, *Mon. Not. R. astr. Soc.,* **328**, 958

Mirabel, I. F., Dhawan, V., Chaty, S., Rodriguez, L. F., Marti, J., Robinson, C. R., Swank, J., Geballe, T., 1998, *Astr. & Astrophys.,* **330**, L9

Misra, R., Kembhavi, A. K., 1998, *Astrophys. J.,* **499**, 205

Mundell, C. G., Wilson, A. S., Ulvestad, J. S., Roy, A. L., 2000, *Astrophys. J.,* **529**, 816

Mushotzky, R. F., Serlemitsos, P. J., Becker, R. H., Boldt, E. A., Holt, S. S., 1978, *Astrophys. J.,* **220**, 790

Mushotzky, R. F., 1982, *Astrophys. J.,* **256**,92

Mushotzky, R. F., Done, C., Pounds, K. A., 1993, *Annual review of astronomy and astrophysics*, **31**, 717

Nandra, K., Pounds, K. A., Stewart, G. C., 1990, *Mon. Not. R. astr. Soc.,* **242**, 660

Nandra, K., Pounds, K. A., Stewart, G. C., George, I. M., Hayashida, K., Makino, F., Ohashi, T., 1991, *Mon. Not. R. astr. Soc.,* **248**, 760

Nandra, K., Pounds, K. A., 1994, *Mon. Not. R. astr. Soc.,* **268**, 405

Nandra, K., George, I. M., Mushotzky, R. F., Turner, T. J., Yaqoob, T., 1997, *Astrophys. J.,* **477**, 602

Nandra et al. 2000, *Astrophys. J.,* **544**, 734

Nandra, K., 1999, *Proceedings of X-ray Astronomy '99 - Stellar Endpoints, AGN and the Diffuse Background*

Narayan, R., Yi, I., 1994, *Astrophys. J.*, **428**, L13

Nayakshin, S., Melia, F., 1997, *Astrophys. J.*, **484**, L103

Nayakshin, S. V., 1998, *PhD Thesis*, University of Arizona

Nayakshin, S., Kallman, T.R., 2001, *Astrophys. J.*, 546, 406

Nayakshin, S., Kazanas, D., Kallman, T.R., 2000, *Astrophys. J.*, **537**, 833

Nayakshin, S., Kazanas, D., Kallman, T. R., 2001, *Proceedings of a joint workshop held by the Center for Astrophysics (Johns Hopkins University) and the Laboratory for High Energy Astrophysics (NASA/ Goddard Space Flight Center)* in Baltimore, MD, 2001, T. Yaqoob and J. H. Krolik

Novak, M., Chiang, J., 2000, *Astrophys. J.*, **531**, L13

Novikov, I. D., Thorne, K. S., 1973, *Balck Holes*, Ed. DeWitt, C., Gordon, B., Breach, NY, 343

O'Brien, P. T., Reeves, J. N., 2001, *Two Years of Science with Chandra*, Abstracts from the Symposium held in Washington, DC, 5-7 September, 2001.

O'Brien, P. T., Reeves, J. N., Turner, M. J. L., Pounds, K. A., Page, M., Gliozzi, M., Brinkmann, W., Stephen, J. B.,,Dadina, M., 2001, *Astr. & Astrophys.*, **365**, L122

Oke, J. B., 1963, *Nature*, **197**, 1040

Orr, A., Barr, P., Guainazzi, M., Parmar, A. N., Young, A. J., 2001, *Astr. & Astrophys.*, 376, 413

Osterbrock, D. E., Shuder, J. M., 1982, *Astrophys. J. Suppl.*, **49**, 149

Padovani, P., Rafanelli, P., 1988, *Astr. & Astrophys.*, **205**, 53

Page, M., Davis, S., Salvi, N., 2002, *submitted to MNRAS*

Parma, P., Murgia, M., de Ruiter, H. R., Fanti, R., 2002, *New Astronomy Reviews*, 46, 313

Parmar, A.N., Martin, D.D.E., Bavdaz, M., et al. 1997, *Astr. & Astrophys., Supplement series*, **122**, 309

Peterson, B. M., McHardy, I. M., Wilkes, B. J. 2000, *New Astronomy Reviews*, **44**, 491

Peterson, B. M. et al., 2000, *Astrophys. J.*, **542**, 161

Peterson, B. M., Wandel, A., 2000, *Astrophys. J.*, **540**, L13

Petre, R., Mushotzsky, R. F., Krolik, J. H., Holt, S. S. 1984, *Astrophys. J.*, **280**, 499

Petrucci et al., 2002, *Astr. & Astrophys.*, **388**, L5

Pfeffermann, E., et al. 1987, *Presented at the Society for Photo-Optical Instrumentation Engineers (SPIE)*, Berlin, West Germany

Piro, L., Matt, G., Ricci, R., 1997, *Astr. & Astrophys., Supplement series*, **126**, 525

Porquet, D., Dubau, J., 2000, *Astrophysical Plasmas: Codes, Models, and Observations*, Proceedings of the conference held in Mexico City, October, **9**, 316

Pounds, K. A., Reeves, J. N., 2002, astro-ph/0201436, *to appear in the Proceedings of the Symposium on 'New Visions of the X-ray Universe in the XMM-Newton and Chandra Era'*, ESTEC, The Netherlands

Pounds, K. A., 1990, *Mon. Not. R. astr. Soc.*, **242**, 20

Pounds, K. A., Nandra, K., Fink, H. H., Makino, F., 1994, *Mon. Not. R. astr. Soc.*, **267**, 193

Pounds, K. A., Nandra, K., Fink, H. H., Makino, F., 1994, *Mon. Not. R. astr. Soc.*, **267**, 193

Pounds, K. A., Nandra, K., Stewart, G. C., Leighly, K., 1989, *Mon. Not. R. astr.*

Soc., **240**, 769

Pounds, K.A., McHardy, I.M., 1988, *Physics of neutron stars and black holes*, ed. Tanaka, Y., Tokyo, Japan, p285

Pounds, K. A., Stanger, V. J., Turner, T. J., King, A. R., Czerny, B., 1987, *Mon. Not. R. astr. Soc.*, **224**, 443

Pounds, K.A., 1986, in *Proc. Conf. Variability of Galactic and Extragalactic X-rat sources*, ed, A. Treves, Como, Italy, p.1

Pringle, J. E., 1981, *Annual review of astronomy and astrophysics*, **19**, 137

Rees, Martin. J., 1998, *Black Holes and Relativistic Stars* Ed. Robert, M. Wald., Chicago : University of Chicago Press, 79

Reeves, J., 2002, *Active Galactic Nuclei: from Central Engine to Host Galaxy Abstract Book*, meeting held in Meudon, France, July 23-27, 2002, Eds.: S. Collin, F. Combes and I. Shlosman. To be published in ASP (Astronomical Society of the Pacific), Conference Series, 7

Reeves, J. N., Turner, M. J. L., Pounds, K. A., O'Brien, P. T., Boller, Th., Ferrando, P., Kendziorra, E., Vercellone, S., 2001, *Astr. & Astrophys.*, **365**, L134

Reeves, J. N. & Turner, M.J.L., 2000, *Mon. Not. R. astr. Soc.*, **316**, 234

Reynolds, C. S., Fabian, A. C., 1995, *Mon. Not. R. astr. Soc.*, **273**, 1167

Reynolds, C. S. 1997, *Mon. Not. R. astr. Soc.*, **286**, 513

Rieke, G. H., Lebofsky, M. J., 1979, *Astrophys. J.*, , **227**, 710

Rodriguez, E. J. M., Perez, G. A. M., Lemke, D., Meisenheimer, K., 1996, *Astr. & Astrophys.*, **315**, L129

Ross, R. R., Fabian, A.C., 1993, *Mon. Not. R. astr. Soc.*, **261**, 74

Ross, R. R., Fabian, A. C., Mineshige, S., 1992, *Mon. Not. R. astr. Soc.*, **258**, 189

Rybicki, G., Lightman, A., 1979, *Radiative processes in astrophysics*, John Wiley &

Sons, Inc

Sako, M., Kahn, S. M., Branduardi-Raymont G., Kaastra, J. S., Brinkman, A. C., Page, M. J., Behar, E., Paerels, F., Kinkhabwala, A., Liedahl, D. A., den Herder, J. W., 2002, astro-ph/0112436, *submitted to ApJ*

Salvati, M. et al., 1993, *Astr. & Astrophys.*, **274**, 174

Salvi et al., 2003, *in preparation*

Sandage, A., 1965, *Astrophys. J.*, **141**, 1560

Saxton, R. D., et al. 1993 *Mon. Not. R. astr. Soc.*, , **262**,63

Schlegel, E. M., 1998, *New Astronomy*, **3**, 427

Schlegel, D.J., Finkbeiner, D. P., Davis, M., 1998, *Astrophys. J.*, **500**, 525

Schmidt, M., 1963, *Nature*, **197**, 1040

Schmidth, M., Green, R. F., 1983, *Astrophys. J.*, **239**, 352

Schnopper, H. W., et al. 1978, *Astrophys. J.*, **222**, L91

Sembay, S.,Hanson, C. G., Coe, M. J., 1987, *Mon. Not. R. astr. Soc.*, **226**, 137

Seyfert, C.K., 1943, *Astrophys. J.*, **97**, 28

Shakura, N. I., Sunyaev, R. A., 1973, *Astr. & Astrophys.*, **24**, 337

Shields, G., A., 1978, *Nature*, **272**, 706

Shields, J. C., Ferland, G. J., Peterson, B. M., 1995, *Astrophys. J.*, **441**, 507

Shih, D.C., K. Iwasawa, Fabian, A.C., 2002, astro-ph/0202432

Singh, K. P., 1999, *Mon. Not. R. astr. Soc.*, **309**, 991

Smith, G., Gene Smith's Astronomy Tutorials
http://casswww.ucsd.edu/public/tutorial/AGN.html

Skibo, J. G., 1997, *Astrophys. J.*, **478**, 522

Stark, J. P., Davidson, P. J. N., Culhane, L., 1977, *Mon. Not. R. astr. Soc.,* **174**, 35

Strüder, L., et al. 2001, *Astr. & Astrophys.,* L18

Sun, W. H, Malkan, M. A., 1989, *Astrophys. J.,* **346**, 68

Svensson, R, Zdziarski, A. A., 1994, *Astrophys. J.,* **436**, 599

Tanaka, Y., Nandra, K., Fabian, A. C., Inoue, H., Otani, C., Dotani, T., Hayashida, K., Iwasawa, K., Kii, T., Kunieda, H., Makino, F., Matsuoka, M., 1995, *NATURE* **375**, 659

Tagliaferri, G., et al. 1988, *Astrophys. J.,* **331**, L113

Telesco, C. M., Decher, R., Joy, M., 1990, *Astrophys. J.,* **343**, L13

Terashima, Y., Iyomoto, N., Ho, L. C., Ptak, A. F., 2001, in *X-ray Emission from Accretion onto Black Holes*, Proceedings of a joint workshop held by the Center for Astrophysics (Johns Hopkins University) and the Laboratory for High Energy Astrophysics (NASA/ Goddard Space Flight Center) in Baltimore, Eds.: T. Yaqoob and J. H. Krolik

Teräsranta, H. et al. 1998, *Astr. & Astrophys., Supplement series*, **132**, 305

Turner, T. J., Mushotzky, R. F., Yaqoob, T., George, I. M., Snowden, S. L., Netzer, H., Kraemer, S. B., Nandra, K., Chelouche, D., 2002, *Astrophys. J.,* **574**, L123

Turner, M. J. L., et al. 2000, *Astr. & Astrophys.,* L27

Turner, T. J., George, I. M., Mushotzky, R. F., 1993, *Advances in Space Research*, **13**, 387

Turner, M. J. L. 1990, *Mon. Not. R. astr. Soc.,* **244**, 310

Turner, T. J., Pounds, K. A. 1989, *Mon. Not. R. astr. Soc.,* **240**, 833

Turner, M. J. L., Smith, A., Zimmermann, H. U. 1981, *Space Science Review*, **30**, 513

Unger, S. W., Lawrence, A., Wilson, A. S., Elvis, M., Wright, A. E., 1987, *Mon. Not. R. astr. Soc.,* **228**, 521

Urry, C. M., Padovani, P., 1995, *Publs astr. Soc. Pacif.,* **107**, 803

Uttley, P., McHardy, I, 2002, *Mon. Not. R. astr. Soc.,* accepted for publication

Uttley, P., McHardy, I. M., 2001, *Mon. Not. R. astr. Soc.,* **323**, L26

Uttley, P., McHardy, I. M., Papadakis, I. E., Guainazzi, M., Fruscione, A., 1999, *Mon. Not. R. astr. Soc.,* **307**, L6

Veron-Cetty, M.-P., Veron, P., 2001, *Astr. & Astrophys.,* **374**, 92

Veron-Cetty, M. P., Veron, P., 1985, *A Catalogue of Quasars and Active Nuclei,* ESO Scientific Report, Garching: European Southern Observatory (ESO), 2nd ed

Voges, W., et al. 1999, *Astr. & Astrophys.,* **349**, 389

Walter, R., Fink, H. H., 1993, *Astr. & Astrophys.,* **274**, 105

Wandel, A. 1999, *Astrophys. J.,* **527**, 649

Wandel, A., 1991, *Astr. & Astrophys.,* **241**, 5

Wandel, A., Mushotzky, R. F. 1986, *Astrophys. J.,* **306**, L61

Ward, Martin., et al., 1987, *Astrophys. J.,* **315**, 74

Warwick, R. S., Barstow, M. A., Yaqoob, T. 1989, *Mon. Not. R. astr. Soc.,* **238**, 917

Weaver, K. A., Nousek, J., Yaqoob, T., Hayashida, K., Murakami, S., 1995, *Astrophys. J.,* **451**, 147

Weaver, K. A., 2000, Proceedings of X-ray Astronomy '99 - *Stellar Endpoints, AGN and the Diffuse Background,* G. Malaguti, G. Palumbo and N. White (eds), Gordon and Breach (Singapore)

Wilkes, Belinda J., Masnou, Jean-Louis., Elvis, Martin., McDowell, Jonathan., Arnaud, Keith. 1989, ESA, *The 23rd ESLAB Symposium on Two Topics in X Ray Astronomy*, 2, 1081

Wilkes, B. J. 1986, *Mon. Not. R. astr. Soc.*, **218**, 331

Wilms, J, Nowak, M. A., Dove, J. B., Fender, R. P., di Matteo, T., 1999 *Astrophys. J.*, **522**, 460

Williams, O. R., Turner, M. J. L., Stewart, G. C., Saxton, R. D., Ohashi, T., Makishima, K., Kii, T., Inoue, H., Makino, F., Hayashida, K., Koyama, K., 1992, *Astrophys. J.*, **389**, 157

Wright, A. E., Allen, D. A., Krug, P. A., Morton, D. C., Smith, M. G. 1977, *IAUC*, **3145**, 2

Yaqoob, T., Warwick, R. S., Makino, F., Otani, C., Sokoloski, J. L., Bond, I. A., Yamauchi, M., 1993, *Mon. Not. R. astr. Soc.*, **262**, 435

Yaqoob, T., George, I. M., Nandra, K., Turner, T. J., Serlemitsos, P. J., Mushotzky, R. F., 2001, *Astrophys. J.*, **546**, 759

Yaqoob, T., Padmanabhan, U., Dotani, T., George, I. M., Turner, T. J., Nandra, K., 2001, *In "X-ray Emission from Accretion onto Black Holes"*, E79, proceedings of a workshop held by JHU and LHEA, Eds. Yaqoob, T. & Krolik, J. H.

Zdziarski, A. A., 1995, *Advances in Space Research*, **15**, 27

Zdziarski, A. A., Poutanen, J., Johnson, W. N., 2000, *Astrophys. J.*, **542**, 703

Appendix A

Differential photometry

The magnitude of a star in the observation frame is given by

$$m = m_{inst} + m_{zero} - Ext \tag{1}$$

where, m is the magnitude, m_{inst} is the measured instrumental magnitude and m_{zero} is the zero point which depends upon the instrumental setup. Ext is the is the extinction at a particular wavelength per unit airmass (at the time of observation) which was obtained from the La Palma extinction records. The airmass was calculated using the IRAF package *setairmass*.
Eq. 1 can be written as

$$m_{zero} = m - m_{inst} + Ext \tag{2}$$

For a standard star the magnitude m_{std} is known and the instrumental magnitude can be measured from the observation frame. Thus a standard star observation is used to determine the zero point m_{zero} (Eq. 2). Henceforth the object frame taken on the same night as the standard star observation will be referred to as the calibrated frame. With the zero point determined from the standard star observation we can obtain the magnitudes of stars in the calibrated frame.

Since simultaneous standard star observations were available for only one of the object frames I have used the the magnitude of a comparison star B (determined for

the calibrated frame) to find the magnitude of the object star for the non-calibrated object frames as follows;

$$m_{obj} - m_B = m_{obj(inst)} - m_{B(inst)} \tag{3}$$

$$m_{obj} = m_B + m_{obj(inst)} - m_{B(inst)} \tag{4}$$

Since the magnitude m_B for star B is known and $m_{obj(inst)}$ and $m_{B(inst)}$ can be measured one can determine the magnitude of the object star.

Appendix B

Dead time and coincidence loss correction

The OM count rates were corrected for dead-time and coincidence losses using the following formula.

$$C = \frac{ln(1 - C_{det} \times T)}{T_{ft} - T} \tag{5}$$

where C is the measured count rate, C_{det} is the real count rate, T and T_{ft} are the CCD frame time and the frame transfer time in seconds respectively. The frame time (T) is a function of the OM science window configuration and can be obtained from the "WDX" product files using the SAS task *rudiframetime*. The frame transfer time $T_{ft} = 1.74 \times 10^{-4}$ s.

Conversion of OM count rate to flux

The corrected count rates were converted to fluxes using the appropriate conversion factor for each filter. The conversion factors for OM fllters are listed in table 1.

Filter	Wavelength (Å)	Factor
UVW1	2400-3600	4.833E-16
UVM2	2000-2800	1.819E-15
UVW2	1800-2600	4.190E-15
U	3000-4000	1.900E-16
B	3800-5000	1.599E-16
V	5000-6000	2.152E-16

Table 1: Count rate to flux conversion factors for OM filters. Fluxes are obtained by multiplying the count rate with the appropriate factor for the filter used.

Reddening correction

The fluxes were corrected for Galactic extinction using the equation,

$$f_{obs}(\lambda) = f_{int}(\lambda)10^{-0.4A_\lambda} \tag{6}$$

where, f_{obs} and f_{int} are the observed and intrinsic fluxes, respectively. The extinction at a wavelength λ is related to the colour excess E(B-V) and to the reddening curve k(λ) by

$$A_\lambda = k(\lambda)E(B-V) = \frac{k(\lambda)A_V}{R_V} \tag{7}$$

The values for A_λ were determined using the reddening law of Allen (1976) and R_V = 3.1. The colour excess E(B-V) for individual objects was obtained from literature. These values were substituted into Eq. 6 to obtain the extinction corrected fluxes for each OM filter.